1999

Application of spectral hole burning to the study of in vitro cellular systems

Nebojsa Milanovich
Iowa State University

INFORMATION TO USERS

This manuscript has been reproduced from the microfilm master. UMI films the text directly from the original or copy submitted. Thus, some thesis and dissertation copies are in typewriter face, while others may be from any type of computer printer.

The quality of this reproduction is dependent upon the quality of the copy submitted. Broken or indistinct print, colored or poor quality illustrations and photographs, print bleedthrough, substandard margins, and improper alignment can adversely affect reproduction.

In the unlikely event that the author did not send UMI a complete manuscript and there are missing pages, these will be noted. Also, if unauthorized copyright material had to be removed, a note will indicate the deletion.

Oversize materials (e.g., maps, drawings, charts) are reproduced by sectioning the original, beginning at the upper left-hand corner and continuing from left to right in equal sections with small overlaps. Each original is also photographed in one exposure and is included in reduced form at the back of the book.

Photographs included in the original manuscript have been reproduced xerographically in this copy. Higher quality 6" x 9" black and white photographic prints are available for any photographs or illustrations appearing in this copy for an additional charge. Contact UMI directly to order.

UMI

A Bell & Howell Information Company
300 North Zeeb Road, Ann Arbor MI 48106-1346 USA
313/761-4700 800/521-0600

Application of spectral hole burning to the study of in vitro cellular systems

by

Nebojsa Milanovich

A dissertation submitted to the graduate faculty

in partial fulfillment of the requirements for the degree of

DOCTOR OF PHILOSOPHY

Major: Physical Chemistry

Major Professor: Gerald J. Small

Iowa State University

Ames, Iowa

1999

Graduate College

Iowa State University

This is to certify that the Doctoral dissertation of

Nebojsa Milanovich

has met the dissertation requirements of Iowa State University

Signature was redacted for privacy.

Major Professor

Signature was redacted for privacy.

For the Major Program

Signature was redacted for privacy.

For the Graduate College

to my family

ACKNOWLEDGMENTS

I wish to express my appreciation to my research advisor, Professor Gerald J. Small, for his support, guidance and encouragement, and for giving me the freedom to follow my instincts in the lab. I truly admire his professionalism and I hope to one day establish the same high standards for my own research program. I am also indebted to Dr. John Hayes, with whom I worked closely, for the many discussions we had and for his patience in explaining many basic concepts to me. In addition, I would like to thank Dr. Ryszard Jankowiak for many useful discussions and enduring the numerous fouls I committed on him during our weekly basketball games.

I would like to give very special thanks to Dr. Tonu Reinot for all the assistance he has provided for my research over the years and, more importantly, for the countless laughs and harmless pranks. My sincere thanks goes to Dr. Margus Rätsep for his assistance with my research and for pointing out that no matter how demanding my career gets, or how important I may become, I should always take time and go fishing. To my one-time fellow graduate students, Dr. Hsing-Mei Wu, Dr. Mohamad Toutounji, and (soon to be doctor) Kenny Roberts, I am truly grateful for their friendship and for not being too upset with the occasional pranks to which they have fallen victim. I wish to thank Kathy Fitzgerald for all the help she has been in dealing with paperwork and the many laughs we shared in the meantime. I would also like to express my appreciation to my former general chemistry student, Robin Lehman, for doing a marvelous job with the cell culture.

Most of all, I am eternally grateful for the undying love and support from my family.

Mama, Tata, and Baba Rada have shown me that with hard work, determination, and perseverance I will achieve my goals in life. I hope I will be able to do the same for my children and grandchildren one day. To my wife and best friend, Iman Yazdi, I am truly thankful for her tolerance of my moodiness, my relentless sense of humor, and for always being there for me whenever I needed her. A few sentences cannot begin to describe all that she has meant to me. Finally, I am grateful and excited about the upcoming birth of our first child in the next month, which Iman and I have affectionately nicknamed Bean. Hey, Bean, this doctorate is as much for you as it is for me, buddy.

TABLE OF CONTENTS

CHAPTER 1. GENERAL INTRODUCTION

1.1. The Onset of Cancer

Cancer refers to a disease that results in the uncontrolled growth and spread of abnormal cells. These cells can develop into benign cystic growths or life-threatening malignant tumors. For a malignant tumor to develop, the DNA of a cell must undergo several mutations whereby a dividing cell sustains a mutation and, subsequently, passes on this mutation to the daughter cells. These daughter cells then sustain further mutations that are passed on to the next generation of daughter cells, and so on, until a cell develops the inclination to carry on uncontrolled proliferation (growth). At a certain stage, referred to as hyperplasia, the cells proliferate excessively, but still appear normal. This state persists until another mutation causes a cell to assume irregular shapes and orientations while continuing to proliferate abnormally; this stage is known as dysplasia. Dysplastic cells continue to grow abnormally with increasing irregularity in shape and eventually develop into an *in situ* cancer, i.e., they do not invade neighboring tissues. Once the tumor cells become invasive, they can eventually leave the primary site (site of the original tumor) and metastasize by entering the blood stream or the lymphatic system and, thus, initiate the growth of other tumors at secondary sites. It is at this point that the tumor is said to be malignant and the most deadly (and incurable) [1, 2].

The American Cancer Society (ACS) projects that 1,221,800 new cases of cancer will be diagnosed in the United States in 1999, with 14,300 new cases in Iowa, alone [3]. These projections exclude basal and squamous cell skin cancer and *in situ* cancers except bladder

cancer. Over one million more new cases will be diagnosed for basal and squamous cell skin cancer. Fortunately, many cancers can be prevented with proper diet and exercise, minimized exposure to direct sunlight and carcinogens, and by avoiding tobacco and alcohol [3, 4]. In 1997, Bailar and Gornik [5] reviewed the progress against cancer in the U.S. between 1970 and 1994 based on age-adjusted mortality rates. In their analysis, the age-adjusted mortality from all cancers increased by 6.0 percent over this time period, including a 1.0 percent decrease between 1991 and 1994. The decrease in deaths over this three year period was attributed to a combination of preventive measures and early detection of cancer while, in contrast, new cancer treatments were deemed to be "largely disappointing". The authors concluded by advocating that an increased emphasis should be placed on prevention. In this context, prevention includes the aforementioned guidelines determined by the ACS as well as early detection of cancer when it is at a curable stage.

1.2. Early Detection of Cancer

Factors such as a family history of cancer and occupational exposure to carcinogens, for instance, play a significant role in increasing a person's risk for developing cancer. Furthermore, this disease takes several years to decades to evolve and, as life expectancies increase, so does the risk of developing cancer. As a second line of defense against cancer mortality, routine screening and early stage detection of tumors (i.e., at noninvasive stages), when tumor removal and cancer therapies are most effective [6], would increase the odds of survival if cancer were to occur. The ACS has set up guidelines for self-testing of certain types of cancers such as breast cancer for women and testicular cancer for men. They have

also set forth recommendations for physicans for routine clinical screenings for common cancers, e.g., using pap smears and mammograms for detecting cervical and breast cancer, respectively, in women and screening for prostate-specific antigens (PSA) for possible prostate cancer in men. Routine screening and self-examinations are particularly important for cancers such as breast cancer which does not produce early symptoms, e.g., fever, weight loss, fatigue, etc. [4]. It should be emphasized that screening for cancer is somewhat arbitrary in that it is left to the discretion of the physician. Only when a physician has reason to suspect cancer will tests be conducted. These suspicions can be raised by considering a patient's family history, lifestyle and occupation, or the presence of certain symptoms. Once suspicion is aroused, possible cancer diagnostics include physical examination, testing for the presence of tumor-specific biomarkers for the particular type of cancer suspected, imaging technologies, and microscopic examination of biopsies. If the presence of a tumor is verified, the tumor's location, as well as that of other tumors, is determined. Furthermore, diagnostics are used to grade and stage, i.e., characterize, the tumor. Grading a tumor describes how closely tumor cells resemble normal, healthy cells of the same type based on a tumor cell's degree of differentiation. Staging further classifies a tumor's progress based on size of the primary tumor and whether a tumor has metastasized. Information from staging and grading is then used to determine the appropriate method of treatment and likelihood of recovery.

1.2.1. Screening for Cancer [4]

The potential problem with screening techniques is the possibility of obtaining false-negative or false-positive results which *incorrectly* indicate the absence or presence of

cancer, respectively. The utility of a screen technique is determined by its level of accuracy. The degree of accuracy is, in turn, characterized by the sensitivity and specificity of a particular methodology. Sensitivity describes the ability of a screening test to identify a disease whereby an increase in sensitivity decreases the chance of false-negative results. As an example, a commonly used test for cervical cancer is a pap smear. Unfortunately, the accuracy of this test varies from 60 - 99% and becomes less reliable in older women, especially post-menopausal, thus leading to a possible 40% chance of false-negative results. In contrast, specificity refers to a test's ability to exclude a disease that is not present thereby decreasing the possibility of a false-positive outcome. Prostate cancer, for instance, is curable when detected at an early stage, but because it might not produce symptoms, 25% of diagnoses occur at late stages. Screening for elevated levels of PSA has been suggested for early detection of prostate cancer. However, this test is prone to giving false-positive results because 40% of men having elevated levels of PSA do not have prostate cancer. In general, many methods for screening cancer are available, each having its own degree of accuracy. For other cancers, unfortunately, no early screening test exists. One such case is lung cancer, where the tumor is at an advanced stage by the time x-rays are able to detect its presence.

1.2.2. Current Diagnostic Testing of Cancer [4]

Complaints of various symptoms, e.g., rapid weight loss, fever, and fatigue, can indicate many possible afflictions, including cancer. The diagnostic tests used to detect cancer will depend on the symptoms, possible location and type of cancer, patient and physician preferences, and the willingness of a person's health care provider to pay for

conducting a particular test. Moreover, no single methodology can diagnose, grade, and stage a tumor, but rather techniques are often used in combination with each other. Below is a brief survey of diagnostic techniques currently in clinical use.

Conventional and digital radiography are easy and inexpensive imaging methodologies used for initial evaluation of patients. Both methodologies are based on differences in density between normal and cancer tissues and are used to image deep tumors, e.g., lung cancer. Conventional radiography involves capturing images on x-ray film while images obtained by digital radiography are captured and stored on computer. In general, digital radiography is preferred over conventional x-ray images in that images acquired by computer can be easily manipulated, e.g., regions of interest in a digital image can be enlarged for closer examination. Moreover, conventional x-rays usually require a contrast medium such as iodine or barium to be administered to the patient in order to enhance the contrast between normal and tumor tissues. A contrast medium is often times unnecessary for digital radiography.

Unlike the radiographic techniques described above, which produce sliced (planar) images, computerized tomography (CT) uses x-rays to provide three-dimensional images of a tumor. These three-dimensional images furnish information about tumor size, shape, volume, and location. However, CT scanning is 6-10 times more costly than the aforementioned radiographic techniques while exposure to x-ray radiation is similar, as is the need for contrast media. Limitations of CT include being unable to detect small tumors, or cancers where no mass has developed, implying that CT tests cannot determine whether a

cancer has metastasized.

Magnetic resonance imaging (MRI) uses radiowaves and magnetic fields to produce two-dimensional images. The advantage of MRI over x-rays is that it can be used to image regions of the body that x-rays cannot, such as the brain. Furthermore, MRI can detect smaller tumors than CT and is able to distinguish between tumors and cysts. The disadvantage of MRI is, however, that it is unable to detect calcification, which is a potential sign of breast cancer. In this regard, x-rays (mammograms) remain the standard methodology for detecting breast tumors. The high cost of MRI, which is more expensive than CT, also prohibits it from being widely available.

Ultrasonagraphy, better known as ultrasound, is a readily available and inexpensive imaging technique. Like MRI, ultrasound can distinguish between solid tumor masses and cysts, making it a good technique for visualizing solid tumors in soft tissue. However, ultrasound is unable to penetrate bone and gas-filled cavities and is, thus, ineffective in imaging cancer of the brain, lungs, and the gastrointestinal tract.

The diagnostic imaging techniques mentioned so far are all noninvasive. In contrast, biopsies, dubbed the "end-all" diagnostic technique, are invasive, involving the removal of tissue samples suspected of being cancerous. Methods for obtaining tissue samples include fine needle biopsies and surgical biopsies whereby excised tissue is prepared for examination by a pathologist. In fine needle biopsies, a needle is used to remove easily accessible tumors and, in some cases, deep tumors. Unfortunately, fine needle biopsies often yield false-negative results because the needle has missed the tumor. This is especially problematic for

deep tumors and, as a result, other imaging techniques such as ultrasound are used in conjunction with needle biopsies as a way of guiding the needle to the tumor mass. Surgical biopsies are considered more complicated procedures and the most invasive, sometimes requiring a patient to undergo two surgical procedures. The advantage of surgical biopsies over needle biopsies is that more tissue can be removed for examination. thus reducing the risk of an incorrect diagnosis. Some surgical biopsies involve preparation of frozen slices of tissue that can be immediately examined. In this way, a patient undergoes surgery only once since a prompt examination of the excised tissue allows for immediate excision of the tumor. The problems arising from frozen tissue sections comes from distortion of tissue due to freezing, therefore, making an analysis of the sections difficult for a pathologist. As a note, endoscopic methods are used for obtaining tissue samples for biopsy from inaccessible internal organs. In all cases, biopsies are subject to the expertise of the pathologist examining the tissue samples.

In addition to the diagnostic techniques described above, other spectroscopic methodologies are currently under development for possible use for cancer diagnostics. The list of developmental techniques is too extensive to be covered here and so the reader is referred elsewhere for detailed descriptions of other spectroscopic techniques being applied to cancer diagnostics. [7, 8, 9, and references therein]

1.2.3. Hole Burning and Cancer Diagnostics

In 1994, Furusawa and coworkers [10] applied incoherent accumulated photon echo spectroscopy at cryogenic temperatures (6 - 10 K) to normal and cancerous human

pancreatic, renal (kidney), and uterine tissues stained with rhodamine X isothiocyanate (XRITC). The authors were able to distinguish between the normal and cancerous tissue types based on T_2 dephasing times for the tissues, whereby cancerous tissues consistently had shorter dephasing times than normal tissues, e.g., 47 ps and 29 ps for normal and cancerous pancreatic tissues, respectively. This ability to distinguish between normal and tumor tissues included differentiation between normal hepatic (liver) tissue (73 ps dephasing time) and hepatic tissue with metastatic cells from a primary pancreatic tumor (36 ps dephasing time). Furthermore, the dephasing times for normal uterine tissue and myoma tissue (a benign uterine cancer) were similar, suggesting that dephasing has high sensitivity for distinguishing between normal and malignant tissue. In this dissertation, the application of nonphotochemical hole burning (NPHB) to cellular systems, one normal and one cancerous, is proposed. Whereas MRI is based on T_1 relaxation times, NPHB is based, in part, on T_2^* pure optical dephasing. Therefore, NPHB can be considered the optical analog of MRI and, for the application to cellular and tissue systems, is referred to as hole burning imaging (HBI). HBI has several important attributes making it attractive for cellular and tissue analysis including high sensitivity and spatial resolution (~ 0.1 μm). In practice, easily measured parameters obtained from the rate of hole growth, i.e., dispersive hole growth kinetics (HGK), can be compared to distinguish between normal and cancerous cells and tissues. In addition to HGK, variations in pressure of a few MPa or application of an external electric (Stark) field to holes can also be used to differentiate between normal and neoplastic cells and tissues.

Recently, NPHB was demonstrated for two purified cell lines: MCF-10F cells, a normal human breast epithelial cell line, and MCF-7 cells, a human breast adenocarcinoma cell line [11, 12]. Both cell lines were stained with the dye aluminum phthalocyanine tetrasulfonate (APT). Based on changes in the dipole moment for APT in MCF-10F and MCF-7 cells, Stark hole burning was able to distinguish between normal and cancer cells. This difference in the change in dipole moment suggests that dye molecules near the plasma membrane of normal cells experience ordering not found in cancer cells. This observation, described in Chapter 5, holds promise for NPHB as a diagnostic technique. The precise role for NPHB (HBI) as a diagnostic technique would be to aid in detecting, grading, and staging of tumors excised from biopsies in the form of frozen sections by tightly focusing a laser burning on selected regions of a tissue. (In order to make HBI a noninvasive technique one would have to subject a patient to the cryogenic temperatures necessary to observe the NPHB phenomenon!) While the conditions for diagnostic examination of cells and tissues are refined, Chapters 4 and 5 show that NPHB can be an important new tool for providing basic information about localized intracellular environments and other physical properties of cells.

1.3. Dissertation Organization

Chapter 1 describes the various stages of tumor development and a multitude of diagnostic techniques used to detect cancer. Chapter 2 gives an overview of the aspects of hole burning spectroscopy important for its application to the study of cellular systems. Chapter 3 gives general descriptions of cellular organelles, structures, and physical properties that can serve as possible markers for the differentiation of normal and cancerous cells. Also

described in Chapter 3 are the principles of cryobiology important for low temperature spectroscopy of cells, characterization of MCF-10F (normal) and MCF-7 (cancer) cell lines which will serve as model systems, and cellular characteristics of aluminum phthalocyanine tetrasulfonate (APT), which was used as the "test" probe. Information found in Sections 3.2, 2.3, and 3.5 of Chapter 3 are taken mainly from reviews and textbooks. Therefore, the references used to present the generally accepted concepts described in these sections are given at the beginning of each section, not within the text. Chapters 4 and 5 are previously published papers by the candidate pertaining to the results obtained from the application of hole burning to the study of cellular systems. Chapter 4 presents the first results obtained by spectral hole burning of cellular systems. In this paper, MCF-10F cells were stained with APT and prepared for spectroscopic studies at cryogenic temperatures. Standard hole burning parameters were determined and a high pressure system designed by the candidate for the determination of cellular compressibility is also described. Finally, the results obtained for cells stained with APT are compared to the results from hole burning of APT in water, ethanol, and methanol. Chapter 5 gives results for the differentiation of MCF-10F and MCF-7 cells stained with APT by an external applied electric (Stark) field. A general conclusion is presented in Chapter 6. Appendices A and B provide additional characterization of the cell/probe model systems. Appendix A describes the uptake and subcellular distribution of APT in MCF-10F and MCF-7 cells. Appendix B compares the hole burning characteristics of APT in cells when the cells are in suspension and when they are examined while adhering to a glass coverslip. Appendix C presents preliminary results

for a novel probe molecule, referred to as a molecular thumbtack, designed by the candidate for use in future hole burning applications to cellular systems.

References

1. Weinberg, R. *Sci. Am.* **1996**, *275*, 62.
2. Weinberg, R. *One Renegade Cell: How Cancer Begins*; Basic Books: New York; **1998**.
3. American Cancer Society, *Cancer Facts and Figures*, **1999**.
4. Murphy, G. P.; Morris, L. B.; Lange, D. *Informed Decisions: The Complete Book of Cancer Diagnosis, Treatment, and Recovery*; American Cancer Society, **1997**.
5. Bailar, J. C.; Gornik, H. L. *New Eng. J. Med.* **1997**, *336*, 1569.
6. Nowell, P. C. *Cancer Res.* **1986**, *46*, 2203.
7. Wagnières, G. A., Star, W. M., Wilson, B. C. *Photochem. Photobiol.* **1998**, *68*, 603.
8. Richards-Kortum, R., Sevick-Muraca, E. *Annu. Rev. Phys. Chem.* **1996**, *47*, 555.
9. Alfano, R. R., Ed. *Annals of the New York Academy of Sciences: Advances in Optical Biopsy and Optical Mammography*; New York Academy of Sciences, **1998**, *838*.
10. Furusawa, A.; Suga, T.; Uchikawa, K. *J. Opt. Soc. Am. B.* **1994**, *11*, 1456.
11. Milanovich, N.; Reinot, T.; Hayes, J. M.; Small, G. J. *Biophys. J.* **1998**, *74*, 2680.
12. Milanovich, N.; Rätsep, M.; Reinot, T.; Hayes, J. M.; Small, G. J. *J. Phys. Chem. B*, **1998**, *102*, 4265.

CHAPTER 2. HOLE BURNING SPECTROSCOPY

2.1. Introduction to Nonphotochemical Hole Burning

Persistent spectral hole burning is a site-selective spectroscopic technique developed to probe the inhomogeneously broadened absorption spectra of impurities (guests) in crystalline and amorphous solids (hosts) at low temperatures [1, 2]. To observe spectral holes requires: (1) a mechanism by which electronic excitation of a chromophore (guest) can change the energy of excitation; (2) a way in which to probe the original absorption during the persistence time of the energy change; (3) an inhomogeneous broadening mechanism for the absorption band of impurity. For chromophores in amorphous hosts, eg., organic glasses, polymers, and biological macromolecules, inhomogeneous broadening of an absorption band, Γ_{inh}, can range from ~100 – 300 cm^{-1}. Obscured in this inhomogeneously broadened absorption band is a wealth of information pertaining to the host environment. By selectively exciting a subpopulation of chromophores with a transition frequency, ω, using a narrow band laser of frequency, ω_L, where $\omega_L = \omega$, the effects of Γ_{inh} can be removed. As a result, a "hole" appears in the absorption band where the isochromats originally absorbed.

Shown in Figure 2-1 is an inhomogeneously broadened absorption band (origin, or vibronic band) at low temperature. The three dashed bands are zero-phonon lines (ZPL) of a chromophore having inequivalent matrix microenvironments. A ZPL refers to an electronic transition with no net change in the number of phonons associated with the transition. Accompanying each ZPL is a phonon wing, known as a phonon sideband (PSB), which occurs at energies higher than that of the ZPL.

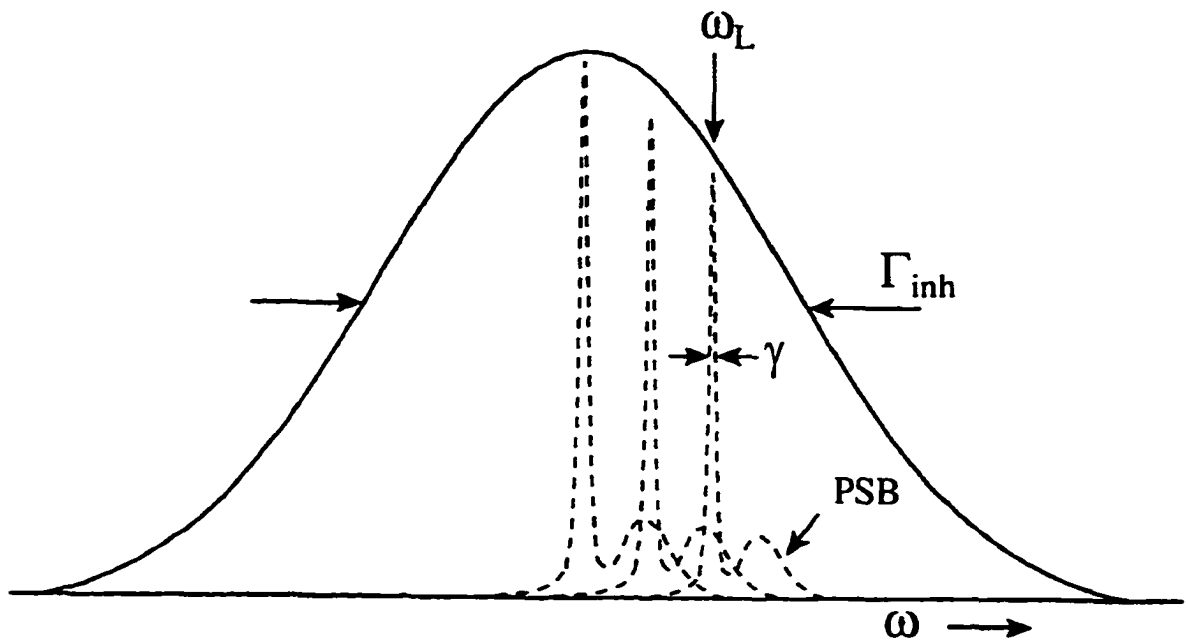

Figure 2-1. Schematic depiction of homogeneously (γ) and inhomogeneously (Γ_{inh}) broadened absorption bands. The ZPL and their associated PSB's are enlarged to clarity. ω_L refers to the laser frequency used to selectively excite a subpopulation of isochromats whose electronic transitions occur at ω, where $\omega = \omega_L$.

An expression for the single site absorption profile has previously been derived [3, 4] for a ZPL frequency, ν, and is given by

$$L(\Omega-\nu)=\prod_{j=1}^{N}\left[\sum_{r_j=0}^{\infty}\frac{e^{-S_j}S_j^{r_j}}{r_j!}\right]\sum_{r=0}^{\infty}\frac{e^{-S}S^{r}}{r!}\,\ell\left(\Omega-\nu-r\omega_m-\sum_{j=1}^{N}r_j\omega_j\right) \qquad (1)$$

where j runs over the discrete pseudolocalized or localized phonons and intramolecular modes. S_j is the Huang-Rhys factor (a measure of the electron-phonon coupling strength) and ω_j in the frequency for the jth mode. The sum over r denotes the contribution from the continuous distribution of low frequency phonons of the amorphous solid and l is the lineshape function. For $r_j = 0$ and $r = 0$, L depicts the ZPL associated with the total zero-point level of the excited electronic state whereby the ZPL is a Lorentzian with a homogeneous width, γ. ω_m is the center frequency (relative to the ZPL) of the one-phonon profile. Sequential nonzero values of $r = 1, 2, 3,...$ correspond to one-, two-, three-,... phonon profiles obtained by the convolution of the one-phonon profile with itself r times. The inhomogeneously broadened absorption spectrum can be obtained by convolving a single-site absorption profile with a Gaussian zero-phonon site excitation distribution function having a center at ν_m and a FWHM of Γ_I, to give

$$A_o(\Omega)=\int d\nu N_o(\nu-\nu_m)L(\Omega-\nu) \qquad (2)$$

where $N_o(\nu-\nu_m)$ is a single site absorption profile, N is a sum of all the single site absorption profile within the inhomogeneous absorption band, and $N_o(\nu-\nu_m)/N$ is the probability of finding a site with a zero-phonon transition frequency equal to ν.

The lineshape of a ZPL is Lorentzian and has a homogeneously broadened linewidth,

γ. The linewidth of a particular ZPL is related to the total optical dephasing time, T_2, by

$$\gamma = (\pi T_2 c)^{-1} \tag{3}$$

where c is the speed of light in a vacuum (2.9979 x 10^{10} cm/s) and the linewidth has units of cm^{-1}. In a hole burning experiment, depletion of a subpopulation of absorbers results in a zero-phonon hole (ZPH) where the ZPH linewidth, Γ_h, is related to the ZPL linewidth, γ, by

$$\Gamma_h = 2\gamma \, . \tag{4}$$

Accompanying the ZPH is a real phonon-sideband hole (real-PSBH), which is analogous to PSB associated with a ZPL. It is located to higher energy of the ZPH and builds on the ZPH. Within the Condon approximation, the relative intensities of the ZPH and real-PSBH are determined by the phonon Franck-Condon factors and are burn time independent. In a hole burned spectrum (i.e., nonphotochemical) the position of the antihole (product absorption) coincides with the real-PSBH and, thus, the real-PSBH is often times obscured by the antihole. Moreover, a pseudo-PSBH also occurs and is the result of off-resonant absorbers whose ZPL frequencies lie to lower energy of ω_B and absorb laser light through their PSB.

T_2 in eq. (3) is given by the expression

$$\frac{1}{T_2} = \frac{1}{2T_1} + \frac{1}{T_2^*} \tag{5}$$

in which T_1 is the excited-state lifetime of the chromophore and T_2* is the pure dephasing time which is attributed to the single site transition frequency modulations resulting from the interaction of the excited state of the chromophore with the intrinsic two level system (TLS_{int}) for a temperature, T, where $T \leq 10$ K and with bath phonons when $T \geq 10$ K. In

general, for a variety of amorphous solids the temperature dependence of T_2* (and the ZPL width) is proportional to $T^{\sim 1.3}$ for $T \leq 10$ K and describes the dephasing from the electron-TLS coupling. (See Section 2.1.1. for more details on two level systems) In contrast, for $T \geq 10$ K, additional contributions to the dephasing are made by exchange coupling with pseudolocalized phonon modes. In addition to pure dephasing, spectral diffusion also contributes to hole width. Spectral diffusion arises from the inherent structural disorder of the glass, resulting in a broad distribution of TLS relaxation times, over times from picoseconds to hours. The reader is referred elsewhere for a discussion on spectral diffusion. [5-10] An important point to note is that γ determines the maximum achievable spectral resolution in hole burning. However, at room temperature, the contribution of T_2* to γ is ~200 cm^{-1}, which is on the order of Γ_{inh} and, thus, the narrowing of γ is lost due to thermal broadening. Therefore, cryogenic temperatures must be used to minimize the number of low frequency phonons occuring at room temperature as well as other contributions to γ.

2.1.1. NPHB Mechanism

Three general mechanisms exist by which a hole is formed: nonphotochemical hole burning (NPHB), photochemical hole burning (PHB), and population bottleneck hole burning. A brief description of the latter two mechanisms is given here. The reader is referred elsewhere for in-depth treatments of PHB and population bottleneck hole burning [11]. The mechanism for NPHB will be given special attention since the purpose of this dissertation is to apply NPHB to the study of cellular systems.

PHB is observed in amorphous as well as crystalline hosts. It describes hole burning

that results from a chemical reaction initiated in an excited state of a chromophore, meaning that the chromophore is photochemically unstable. The photochemical reactions that can occur as a result of PHB include tautomerization, bond-breaking, and isomerization. For example, the first observation of PHB was for free base phthalocyanine in n-octane whereby selective electronic excitation of the absorption band resulted in an intramolecular proton tautomerization. Absorption frequencies for the photoproduct from PHB are usually found outside of the frequency range of the original inhomogeneous absorption band for the chromophore.

Population bottleneck hole burning occurs by depleting a population of absorbers from the ground state and storing them in a long-lived excited state, e.g., a triplet state. Holes formed by population bottleneck hole burning are transient, whereby the lifetime of these holes are ~ 10^{-4} – 10^{-2} s. This technique was first described for Pr^{3+} in a LaF_3 crystal where the nuclear hyperfine levels served as the bottleneck state [12]. Both holes and antiholes were described for this system. For zinc porphyrin in n-octane [13], the long-lived triplet state was used as the population reservoir to observe a hole in the $S_1 \leftarrow S_0$ transition. The lifetime of the hole and the triplet state were found to be the same.

NPHB is a hole burning process involving a photochemically stable chromophore. It occurs primarily in amorphous solids and results in the rearrangement of the matrix molecules solvating the chromophore, initiated by electron-extrinsic two-level system (TLS_{ext}) coupling. The inherent structural disorder of an amorphous system makes NPHB possible by allowing for reconfiguration of the host-guest interactions. The reconfiguration

is preceded by the completion of the ground to excited state back to ground state cycle whereby the final ground state (postburn) configuration is different from and kinetically inaccessible to the initial (pre-excited, or preburn) configuration. In general, NPHB is a reversible process whereby the hole is "filled" upon an increase in temperature and the absorption of the photophysical product, known as the antihole, is usually located to higher energy of the ZPH. The blue-shifted antihole is the result of an increase in free volume of a chromophore whose S_1 state is $\pi\pi^*$. The temperature dependent behavior of antiholes was used to develop a model for NPHB, *vide infra*.

A mechanism for NPHB was first proposed in 1978 by Hayes and Small [14] using a two-level system (TLS) model based on the coupling of an electronic transition of a chromophore with an amorphous host matrix (see Figure 2-2). Originally, in 1972, Anderson et al. [15] and Phillips [16] independently proposed the TLS theory for glassy systems whereby a certain number of atoms or groups of atoms may occupy, with equal probability, two equilibrium positions separated by an energy barrier. At very low (cryogenic) temperatures these atoms or groups of atoms cannot be activated over the energy barrier, but can interconvert via tunneling. For NPHB, the model by Hayes and Small [14] maintains that amorphous systems are comprised of bistable host-guest configurations approximated by a static distribution of TLS_{ext} and that hole burning occurs as a result of phonon-assisted tunneling in the excited state. In 1981, Hayes et al. [17] suggested that two types of TLS's are involved in NPHB. The first type is the TLS_{ext} which is involved in hole formation and a

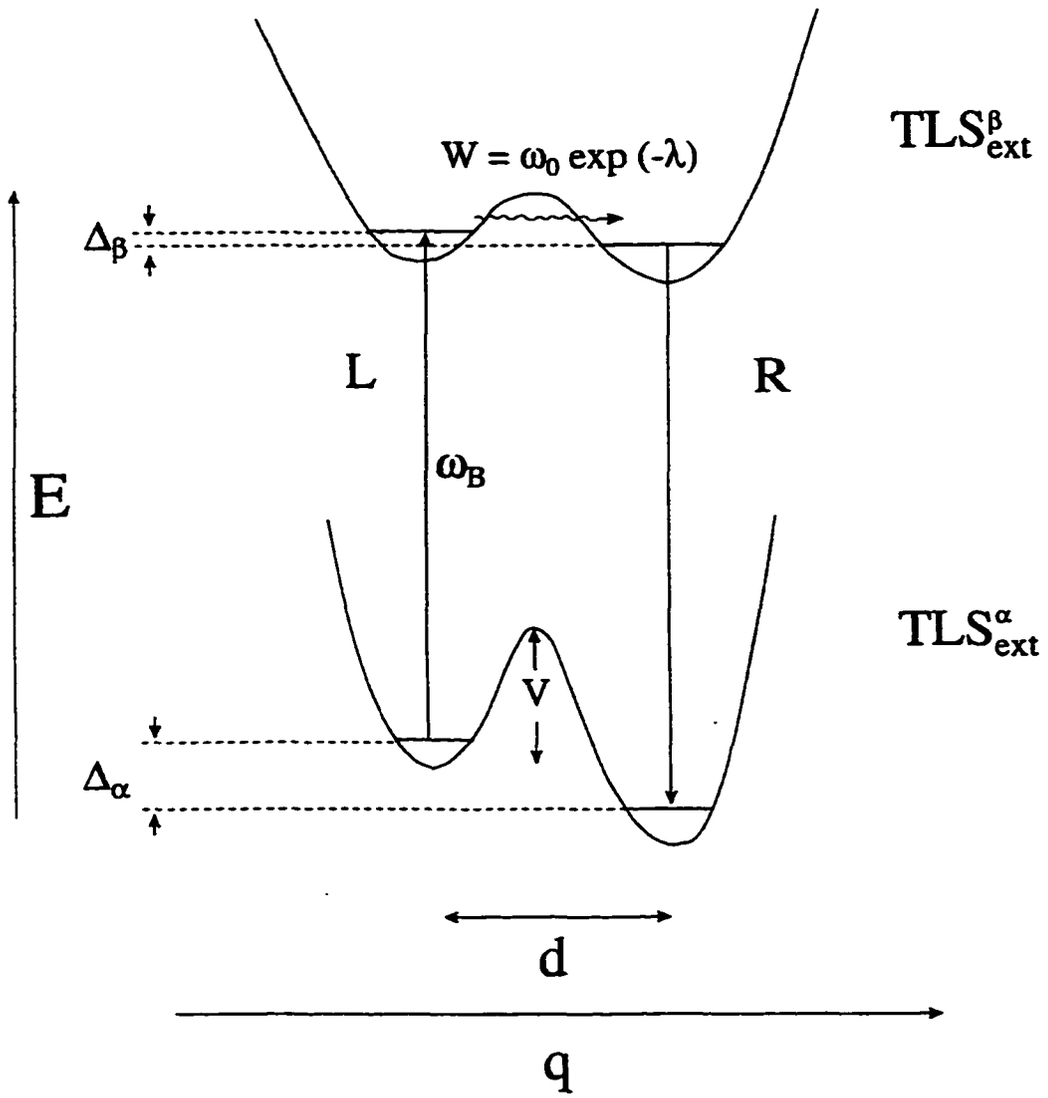

Figure 2-2. Diagram of TLSext coupled to a chromophore in the ground state (α) and the excited state (β). Δ is the asymmetry parameter, V is the barrier height, and q are the intermolecular coordinates. The tunneling frequency, W, is a function of λ, and is defined as $d(2mV)^{1/2}/h$, where m is the tunneling mass. ω_B represents the electronic excitation frequency.

second, fast relaxing type, TLS_{int}, which are responsible for pure dephasing and spectral diffusion. The TLS_{int} are associated with the spatially extended motions of the host matrix and influence the holewidth (as do lifetime and spectral diffusion). The TLS_{ext} correspond to the more localized motions of the guest and the inner shell of solvent molecules about the guest. The phonon-assisted tunneling associated with the TLS_{ext}, together with structural disorder, determine the dispersive hole-growth kinetics (see Section 2.1.2).

Temperature dependent NPHB studies of cresyl violet perchlorate in polyvinyl alcohol [18] later demonstrated that the original mechanism proposed by Hayes and Small was over simplified. While retaining the idea that the rate-determining step of hole formation is the phonon-assisted tunneling in the excited state, the new model proposes the occurrence of an "outside-in" hierarchy of constrained configurational tunneling events. Included in this model is a coupling between TLS_{int} and TLS_{ext} and the notion that reduction of excess free volume in the "outer shell" (due to TLS_{int} tunneling) leads to an increase in "inner shell" free volume about the chromophore. Subsequently, the rate-determining step of hole formation would actually be the excited state tunneling for TLS_{ext}. This process is illustrated in Figure 2-3 for the system of aluminum phthalocyanine tetrasulfonate (APT) in amorphous water. Laser excitation of APT (Figure 2-3a) initiates a hierarchy of dynamical events beginning with the diffusion of water molecules in the outer shell region (Figure 2-3b). This results in a decrease in the matrix free volume in the outer shell region. Subsequently, diffusion of water molecules at the inner shell region (Figure 2-3c) result in excess free volume around APT. In

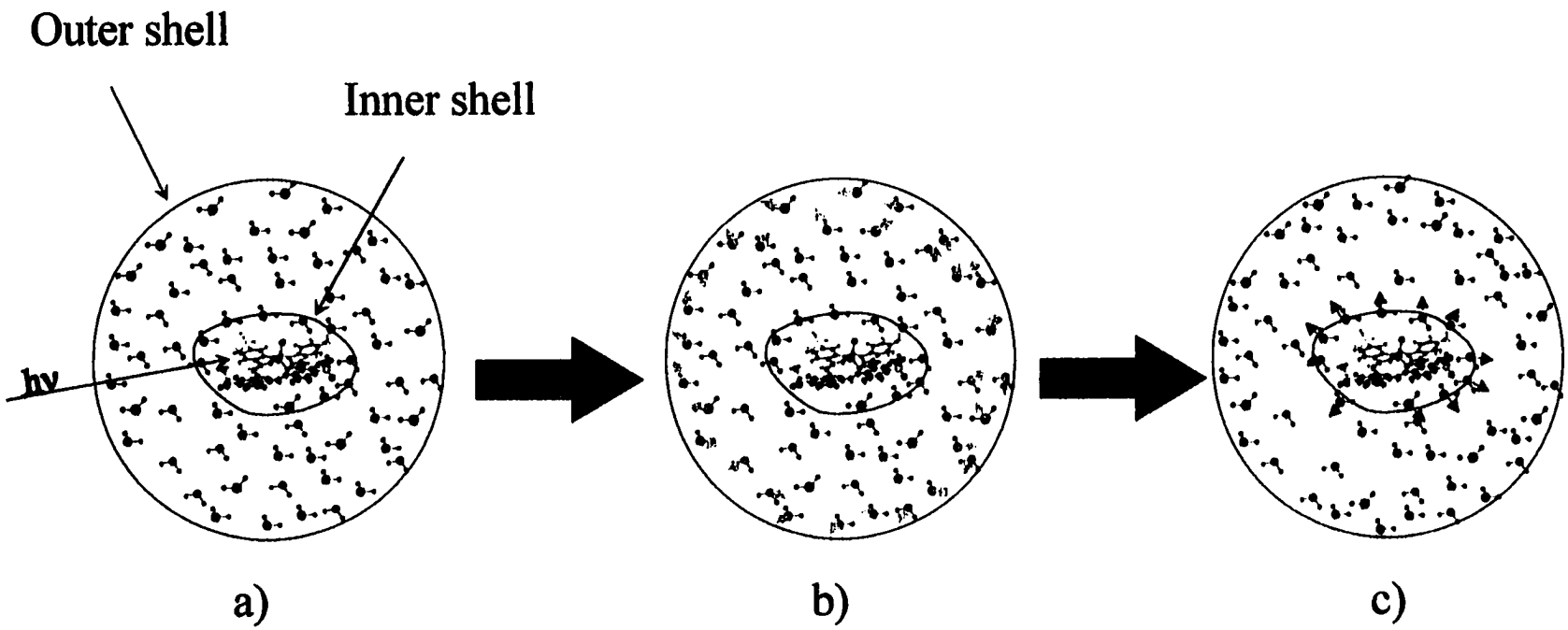

Figure 2-3. Outside-in hierarchy of relaxation events (Onsager model) describing the mechanism for NPHB. Electronic excitation triggers TLS_{int} (a), leading to a decrease in excess free volume of the outer shell (b). The events in (b), in turn, result in increased free volume of the inner shell of solvent molecules about the chromophore (c).

essence, the excess free volume of the outer shell region diffuses towards the inner shell region, in turn, leading to hole formation.

2.1.2. Dispersive Hole-Growth Kinetics

As mentioned in the previous section, Shu and Small [18] proposed that the mechanism for NPHB consists of an "outside-in" hierarchy of relaxation processes whereby an excess in free volume of the outer shell region diffuses to the inner shell region, triggering phonon-assisted tunneling in the excited state of TLS_{ext}, thus, leading to hole formation. Furthermore, the phonon-assisted tunneling process that occurs in the excited electronic state of TLS_{ext} is the rate-determining step of hole formation. The inherent disorder of amorphous solids results in a distribution of values for the phonon-assisted tunneling relaxation rate, R, associated with localized probe inner-shell coordinates. This implies that a single rate constant is inadequate for describing the rate of hole formation and, therefore, the kinetics of this process is considered dispersive.

Based on results for oxazine 720 in glycerol, polyvinyl alcohol (PVOH) thin films, and their deuterated analogues, Kenney et al. [19, 20] developed a theory to describe the dispersive hole growth kinetics of these systems using a Gaussian distribution function for the TLS_{ext} tunneling parameter, λ, where

$$g(\lambda) = N_\lambda \exp\left[-(\lambda - \lambda_o)^2 / 2\sigma_\lambda^2\right] \tag{6}$$

when $\lambda_0^2/2\sigma_\lambda^2 >> 1$, and the normalization constant, $N_\lambda = \left(\sigma_\lambda\sqrt{2\pi}\right)^{-1}$, λ_0 is the center of the Gaussian function, $g(\lambda)$, with a variance σ_λ. According to this theory, the square of the tunneling frequency, W, where

$$W = \omega_o \exp(-\lambda) \tag{7}$$

and ω_0 is the harmonic frequency of TLS_{ext} is proportional to the phonon-assisted tunneling relaxation rate, R. As a result, the relaxation rate can be written as

$$R = \Omega_o \exp(-2\lambda) \tag{8}$$

where Ω_0 ($\approx 8 \times 10^{12}$ s^{-1}) is on the order of ω_0 [19, 20] and is dependent on the TLS_{ext} deformation potential and the asymmetry parameter, Δ. A distribution function for R can then be written based on Gaussian distribution functions for λ proposed by Jankowiak et al. [21-23] where the center of the Gaussian function is at λ_0 with a variance σ_λ. As a result of this approach, the fractional hole depth of the ZPH is 1-$D(t)$, and $D(t)$ is given as

$$D(t) = (2\pi)^{-1/2} \int_{-\infty}^{+\infty} dx \exp(-x^2/2) \exp(-\Sigma_o \xi(x) t) \tag{9}$$

where $\Sigma_0 = P\sigma\Omega_0\tau$, and P is the burn photon flux, σ is the peak absorption cross section, and τ is the excited state lifetime. The variable $x = (\lambda - \lambda_0)/\sigma_\lambda$ and $\xi(x) = \exp[-2(\lambda_0 - \sigma_\lambda x)]$. Included in the derivation of eq. 9 is the assumption that for a majority of the TLS_{ext}

$$\phi(R) = \frac{R}{R+k} \approx \frac{R}{k} << 1 \tag{10}$$

where ϕ(R) is the NPHB quantum yield for a chromophore excited state lifetime of k^{-1}($= \tau$). This assumption originates from earlier work demonstrating that average NPHB quantum yields are low ($< 10^{-4}$ [24, 25]) and are readily tested by the experimental data. This analysis has been successfully applied to the hole growth kinetics and spontaneous hole filling of cresyl violet in PVOH [26] as well as other NPHB systems [27-31].

The parameters obtained from fitting hole growth kinetics data yields values for λ_0

and σ_λ, which, in essence, describe the relative disorder of an amorphous matrix. In addition, the electron-phonon coupling parameter (Huang-Rhys factor), S, is also determined by fitting eq. 9 to the kinetics data. Suffice it to say that S indicates the extent of coupling between the electronic transition of the probe molecule with the phonons of the matrix where $S < 1$ is considered weak coupling, leading to a deep ZPH whereby the fractional hole depth for a saturated hole (a hole burned to maximum depth) is equal to exp(-S). The reader is referred elsewhere for a more complete description of S factors and electron-phonon coupling [32]. Cancer cells and tissues might be viewed as being more structurally disordered than normal cells and tissues. Therefore, the parameters obtained from hole growth kinetics experiments, *viz.*, S, λ_0 and σ_λ, might be used to distinguish between normal and cancerous cells and tissues.

2.2. Effects of Hydrostatic Pressure

High pressure spectroscopy has been useful for investigating intermolecular interactions in solids. Hydrostatic pressure effects on condensed phase systems (i.e., pressure applied by a fluid to all points on the surface of a solid) typically result in red shifts of 0.05 - 0.15 cm^{-1}/MPa for $\pi\pi^*$ state of isolated chromophores imbedded in solids. When the inhomogeneously broadened absorption band of a chromophore in an amorphous solid is monitored, high pressures are required to detect frequency shifts because the bandwidth is large (~ 300 cm^{-1}). On the other hand, the high spectral resolving power of hole burning can provide a more sensitive means in which to probe the solvent interactions between an impurity and the host solid using hydrostatic pressure. The advantage to using hole burning

stems from the fact that homogeneous holewidths are usually $>10^4$ times narrower than an inhomogeneously broadened absorption band at low temperatures. Therefore, pressure-induced changes can be detected using much lower pressures (< 16 MPa, which is achievable with standard helium gas cylinder pressures) than would be necessary to accurately measure the spectral shift of an entire absorption band with a width of hundreds of wavenumbers.

Hydrostatic pressure causes the concomitant broadening of holes along with shifts in the center frequency of holes. The hole broadening that occurs for a given solid is an indicator of the extent of disorder of the matrix. Based on experiments using polymethylmethacrylate (PMMA), polystyrene (PS), and polyethylene (PE) doped with free base phthalocyanine, Sesselmann et al. [33] were able to develop a simple theory that predicts frequency shifts and broadening of holes as a function of applied pressure. Laird and Skinner [34] later improved upon this theory by using a statistical, microscopic model to describe the pressure effects on spectral holes and on the inhomogeneous absorption lineshape of an impurity. This theory assumes that each chromophore is isolated (i.e., noninteracting), the positions of host molecules relative to the chromophore are uncorrelated, the host medium is homogeneous and isotropic, and local compressibility can be replaced by bulk compressibility. Based on these assumptions, the theory predicts that (1) pressure-induced broadening of holes is frequency dependent; (2) long-range interactions are responsible for pressure-induced hole shifts and inhomogeneous broadening; (3) application of pressure results in holes and inhomogeneous lineshapes that are Gaussian; and (4) short-range interactions are responsible for hole broadening. To understand this theory in physical

terms, consider the depletion of a subpopulation of absorbers in an amorphous solid with an absorption frequency, ω. When hydrostatic pressure is applied, the hole that had been burned shifts its center frequency and broadens while the lineshape of the hole becomes Gaussian with applied pressure. Pressure causes the density of the sample to change, thus, changing the long-range interactions and resulting in a shift in the center frequency of the hole. Concomitantly, a change in pressure affects the interaction between the chromophore and its microenvironment, ie., the short-range interactions, such that these interactions change differently for each chromophore of the subpopulation, yielding a broadened hole with a Gaussian lineshape. It should be noted here that if the original hole is recovered when the applied pressure is released, the effects of pressure on the hole (and the system) are referred to as elastic.

Hydrostatic pressure has already been applied to the hole burned spectra of photosynthetic systems [35-38], proteins [39, 40], polymers [41], and eukaryotic cells [42, Chapter 4]. For the work presented in Chapter 4, pressure-induced frequency shifts, $\Delta\omega$ (in cm^{-1}), for cells stained with APT were used to calculate cellular compressibility, κ, according to the relation [34]

$$\Delta\omega(\omega_B, \Delta P) = \frac{n\kappa}{3}\Delta P(\omega_B - \omega_{vac}) \qquad (11)$$

where ΔP (since $\Delta P = P$-1 atm $\approx P$) is the change in pressure, ω_B and ω_{vac} are the burn frequency and vacuum absorption frequency maximum for the probe molecule, respectively, with the difference, (ω_B - ω_{vac}), representing the gas to solvent shift, and n (= 6) is the power of the attractive solute-solvent pairwise potential ($\propto R^{-n}$), which is thought to dominate the

attractive interactions for pressures which are not too high. In the expression for the pairwise potential, R is the solute solvent distance. The impetus for determining the compressibility of cells arises from trying to distinguish between normal and cancer cells based on differences in the structural integrity of the cytoskeleton for these two cell types (see Chapter 3, Section 3.2.3).

2.3. Effects of External Electric (Stark) Fields

Stark hole burning spectroscopy has been applied to the study of probe molecules in various amorphous solids, such as polymers [43, 44], proteins [45, 46], and, most recently, in vitro cellular systems [47, Chapter 5]. In a Stark experiment, an external electric field (Stark field) causes the electronic transition frequency of a molecule to undergo a frequency shift, $\Delta\omega$, due to the interaction of the external field with the dipole moments and polarizabilities of the ground and excited electronic states of the probe. The induced frequency shift (in cm^{-1}) can be expressed as [48]

$$\Delta\omega = -\hbar^{-1}\left[\left(\Delta\bar{\mu}_o + \Delta\bar{\alpha}\cdot\mathbf{E}_{int}\right)\cdot f\mathbf{E}_S + (1/2)\Delta\bar{\alpha}\cdot\left(f\mathbf{E}_S\right)^2\right] \qquad (12)$$

where $\mathbf{E}_S$ and $\mathbf{E}_{int}$ are the Stark field and internal electric field experienced by the probe, respectively, $\Delta\bar{\mu}_o$ is the difference in the molecular dipole moment vectors of the ground and excited states, h is Planck's constant, and f is the Lorentz local field correction factor whereby $f = (\varepsilon + 2)/3$ and ε is the dielectric constant of the matrix. Furthermore, $\Delta\bar{\alpha}$ is the molecular polarizability difference tensor and $\Delta\bar{\alpha}\cdot\mathbf{E}_{int}$ describes a matrix-induced change in dipole, $\Delta\bar{\mu}_{ind}$ contributing to the Stark shift. The first term in eq. 12, $(\Delta\bar{\mu}_o + \Delta\bar{\alpha}\cdot\mathbf{E}_{int})\cdot f\mathbf{E}_S$, describes the linear dependence of $\Delta\omega$ on an electric field while the second term describes the

quadratic dependence. For molecular systems, $\mathbf{E}_{int} >> \mathbf{E}_S$ (eg., $|\mathbf{E}_{int}| \geq 1$ MV/cm [49] and, for the Stark experiments in this dissertation, $|\mathbf{E}_S| \leq 100$ kV/cm is the maximum achievable electric field strength for a ~2 mm separation between electrodes) and, thus, a linear dependence of the frequency shift is observed in amorphous solids. As a result, the quadratic term in eq. 12 can be neglected and the frequency shift is adequately described by

$$\Delta\omega = -\hbar^{-1}\left[\left(\Delta\bar{\mu}_o + \Delta\bar{\alpha}\cdot\mathbf{E}_{int}\right)\cdot f\mathbf{E}_S\right] \tag{13}$$

For hole burning sytems, a linear Stark effect will mean that no shift in the center frequency of a ZPH is observed after applying the Stark field. If, however, the systems are quadratically dependent on the Stark field, then a hole will red-shift relative to the hole position at zero field. A quadratic Stark effect would occur when the external electric field is comparable (or greater) in strength to the internal electric fields in the solid. Since typical hole burning systems undergo a linear Stark effect, including the ones presented in this dissertation, the remainder of this discussion will pertain strictly to the linear behavior of amorphous systems in an external field.

In 1987, Kador et al. developed a relation between hole width, Γ_h, (FWHM, in cm^{-1}) and applied electric field [43], given as

$$\Gamma_h(\mathbf{E}_S) = \omega_o\left[1 + \hbar^{-1}\left(f\Delta\bar{\mu}/\omega_o\right)^2\mathbf{E}_S^2\right]^{1/2} \tag{14}$$

where ω_o is the hole width at zero electric field and $\Delta\bar{\mu}$ is the difference in the ground ($\bar{\mu}_g$) and excited ($\bar{\mu}_e$) electronic state dipole moments. A description of probe-matrix interactions can be developed by considering $\Delta\bar{\mu}$ as having molecular ($\Delta\bar{\mu}_o$) and matrix induced ($\Delta\bar{\mu}_{ind}$)

contributions to the dipole moment change, ie.,

$$\Delta\bar{\mu} = \Delta\bar{\mu}_o + \Delta\bar{\mu}_{ind} \tag{15}$$

For noncentrosymmetric molecules, i.e., molecules without an inversion center, $\Delta\bar{\mu}_o$ represents the change in the intrinsic, permanent dipole moment of the ground and excited electronic states and $\Delta\bar{\mu}_{ind}$ is the matrix-induced dipole moment change [50]. The relative contribution to the overall dipole moment difference, $\Delta\bar{\mu}$, is dependent on the system. In contrast, for centrosymmetric molecules such as aluminum phthalocyanine tetrasulfonate (APT), which have inversion symmetry, $|\Delta\bar{\mu}_o| = 0$ and, thus,

$$\Delta\bar{\mu} = \Delta\bar{\mu}_{ind} \tag{16}$$

Therefore, the splitting and/or broadening of holes that would occur is strictly matrix-induced, where, for example, the D_{4h} symmetry of APT is lowered due to interactions with the matrix. $\Delta\bar{\mu}_{ind}$, in turn, can be viewed as having a random ($\Delta\bar{\mu}_r$) and a nonrandom ($\Delta\bar{\mu}_{nr}$) component [51] such that

$$\Delta\bar{\mu} = \Delta\bar{\mu}_{ind} = \Delta\bar{\mu}_r + \Delta\bar{\mu}_{nr} \tag{17}$$

For the case where $|\Delta\bar{\mu}_{nr}| >> |\Delta\bar{\mu}_r|$, splitting and broadening are both observable [48], meaning that the inversion center of a centrosymmetric molecule such as APT is removed by a chromophore-matrix interaction occuring at a fixed angle, θ, between $\Delta\bar{\mu}$ and the transition dipole, $\boldsymbol{D}$. This situation is illustrated in Fig. 2-4a and b for APT, where the plane of the phthalocyanine ring of APT is perpendicular to the plane of the page. In Fig. 2-4a, when $\Delta\bar{\mu} \,||\, \boldsymbol{D}$, splitting of the hole is observed when the probe laser polarization, $\mathbf{E}_L$, is

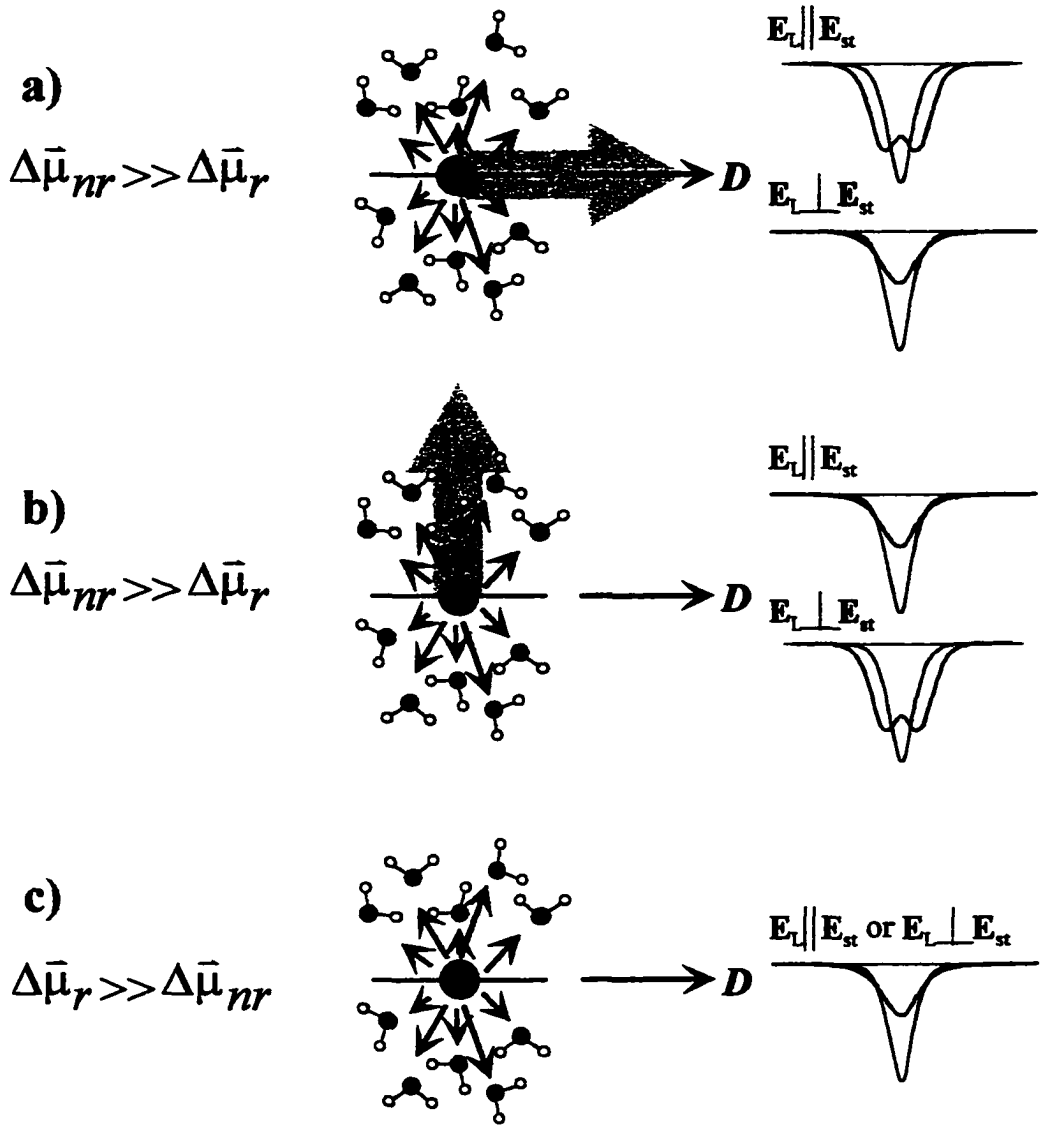

Figure 2-4. Schematic representation of the possible matrix-induced changes in dipole moment on APT observed by application of a Stark field on holes burned at zero field. For $\Delta\vec{\mu}_{nr} >> \Delta\vec{\mu}_r$, $\Delta\vec{\mu}_{ind}$ (green arrow) is a) parallel and b) perpendicular to the transition dipole, ***D***. When $E_L || E_S$ or $E_L \perp E_S$, splitting and broadening are observed in a), respectively, while the opposite is true for b). When $\Delta\vec{\mu}_r >> \Delta\vec{\mu}_{nr}$, $\Delta\vec{\mu}_{ind}$ is randomly induced (black arrows), resulting in hole broadening, irrespective of laser and Stark field orientations.

oriented parallel to $\mathbf{E}_S$, while hole broadening is observed when $\mathbf{E}_L \perp \mathbf{E}_S$. Similarly, Fig. 2-4b represents the situation where $\Delta\bar{\mu} \perp \boldsymbol{D}$, where splitting and broadening are observed when $\mathbf{E}_L \perp \mathbf{E}_S$ and $\mathbf{E}_L \| \mathbf{E}_S$, respectively. In contrast, when a matrix-induced dipole moment change is caused by predominantly random electrostatic interactions with the matrix, i.e., $| \Delta\bar{\mu}_r | >> | \Delta\bar{\mu}_{nr} |$, only broadening is observed, irrespective of the angle between $\mathbf{E}_L$ and $\mathbf{E}_S$. (Fig. 2-4c) Described in Chapter 5 [47] is the case for APT in MCF-10F and MCF-7 cells where broadening is observed when $\mathbf{E}_L \| \mathbf{E}_S$ and $\mathbf{E}_L \perp \mathbf{E}_S$. For APT in MCF-7 cells, $| \Delta\bar{\mu} |$ is the same for parallel and perpendicular laser/electric field orientations, whereby $| \Delta\bar{\mu}_{nr} | \approx 0$. However, $| \Delta\bar{\mu} |$ is different for the two orientations for APT in MCF-10F cells. This difference can be explained by considering that even though $| \Delta\bar{\mu}_r | >> | \Delta\bar{\mu}_{nr} |$, the nonrandom component does not equal zero. The posssible reasons for this difference are discussed in Chapter 4.

References

1. Hayes, J. M.; Jankowiak, R.; Small, G. J. In *Topics in Current Physics, Persistent Spectral Hole Burning: Science and Applications*; Moerner, W. E., Ed. Springer-Verlag: New York, **1987**; p 153.

2. Jankowiak, R.; Hayes, J. M.; Small, G. J. *Chem. Rev.* **1993**, *93*, 1471.

3. Lyle, P., *Ph.D. Dissertation*, Iowa State University, **1993**.

4. Hayes, J. M.; Lyle, P. A.; Small, G. J. *J. Phys. Chem.* **1994**, *98*, 7337.

5. Narasimhan, L. R.; Littau, K. A.; Pack, D. W.; Bai, Y. S.; Elschner, A.; Fayer, M. D. *Chem. Rev.* **1990**, *90*, 439.

6. Littau, K. A.; Fayer, M. D. *Chem. Phys. Lett.* **1991**, *176*, 551.

7. van der Zaag, P. J.; Galaup, J. P.; Völker, S. *Chem. Phys. Lett.* **1990**, *166*, 263.

8. Silbey, R. J.; Koedijk, J. M. A.; Völker, S. *J. Chem. Phys.* **1996**, *105*, 901.

9. Koedijk, J. M. A.; Wannemacher, R.; Silbey, R. J.; Völker, S. *J. Phys. Chem.* **1996**, *100*, 19945.

10. Zilker, S. J.; Haarer, D. *Chem. Phys.* **1997**, *220*, 167.

11. Moerner, W. E., Ed. *Topics in Current Physics, Persistent Spectral Hole Burning: Science and Applications*; Springer-Verlag: New York, **1987**, *44*.

12. Erickson, L. E. *Phys. Rev. B.* **1975**, *11*, 4512.

13. Shelby, R. M.; MacFarlane, R.M. *Chem. Phys. Lett.* **1979**, *64*, 545.

14. Hayes, J. M.; Small, G. J. *Chem Phys.* **1978**, *27*, 151.

15. Anderson, P. W.; Halperin, B. I.; Varma, C. M. *Phil. Mag.* **1972**, *25*, 1.

16. Phillips, W. A. *J. Low Temp. Phys.* **1972**, *7*, 531.

17. Hayes, J. M.; Stout, R. P.; Small, G. J. *J. Phys. Chem.* **1981**, *74*, 4266.

18. Shu, L.; Small, G. J. *Chem. Phys.* **1990**, *141*, 447.

19. Kenney, M.; Jankowiak, R.; Small, G. J. *Chem. Phys.* **1990**, *146*, 47.

20. Kenney, M. J., *Ph.D. Dissertation*, Iowa State University, **1990**.

21. Jankowiak, R.; Rechert, R.; Bässler, H. *J. Phys. Chem.* **1985**, *89*, 4569.

22. Jankowiak, R.; Small, G. J.; *Phys. Rev. B.* **1988**, *37*, 8407.

23. Jankowiak, R.; Hayes, J. M.; Small, G. J. *Phys. Rev. B.* **1988**, *38*, 2084.

24. Jankowiak, R.; Shu, L.; Kenney, M. J.; Small, G. J. *J. Luminescence* **1987**, *36*, 293.

25. Jankowiak, R.; Small, G. J. *Science* **1987**, *237*, 618.

26. Shu, L.; Small, G. J. *J. Opt. Soc. Am. B.* **1992**, *9*, 733.

27. Kim, W.-H.; Reinot, T.; Hayes, J. M.; Small, G. J. *J. Phys. Chem.* **1995**, *99*, 7300.

28. Kim, W.-H.; Reinot, T.; Hayes, J. M.; Small, G. J. *J. Chem. Phys.* **1996**, *104*, 6415.

29. Reinot, T.; Hayes, J. M.; Small, G. J., *J. Chem. Phys.* **1997**, *106*, 457.

30. Reinot, T.; Kim, W.-H.; Hayes, J. M.; Small, G. J. *J. Chem. Phys.* **1996**, *104*, 793.

31. Reinot, T.; Kim, W.-H.; Hayes, J. M.; Small, G. J. *J. Opt. Soc. Am. B.* **1997b**, *14*, 602.

32. Rebane, K. K. *Impurity Spectra of Solids; Elementary Theory of Vibrational Structure*; Plenum Press: New York, **1970**.

33. Sesselman, Th.; Richter, W.; Haarer, D.; Morawitz, H. *Phys. Rev. B.* **1987**, *36*, 7601.

34. Laird, B. B.; Skinner, J. L. *J. Chem. Phys.* **1989**, *90*, 3274.

35. Chang, H.-C.; Jankowiak, R.; Reddy, N. R. S.; Small, G. J. *Chem. Phys.* **1995**, *197*, 307.

36. Reddy, N. R. S.; Jankowiak, R.; Small, G. J. *J. Phys. Chem.* **1995**, *99*, 16168.

37. Wu. H.-M.; Savikhin, S.; Reddy, N. R. S.; Jankowiak, R.; Cogdell, R. J.; Struve, W. S.; Small, G. J. *J. Phys. Chem.* **1996**, *100*, 12022.

38. Wu, H.-M., *Ph.D. Dissertation*. Iowa State University, **1998**.

39. Gafert, J.; Friedrich, J.; Parak, F. *J. Chem. Phys.* **1993**, *99*, 2478.

40. Gradl, G.; Zollfrank, J.; Breinl. W.; Friedrich, J. *J. Chem. Phys.* **1991**, *94*, 7619.

41. Schellenberg, P.; Friedrich, J.; Kikas, J. *J. Chem. Phys.* **1994**, *100*, 5501.

42. Milanovich, N.; Reinot, T.; Hayes, J. M.; Small, G. J. *Biophys. J.* **1998**, *74*, 2680.

43. Kador, L.; Haarer, D.; Personov, R. *J. Chem. Phys.* **1987**, *86*, 5300.

44. Kador, L.; Personov, R.; Richter, W.; Sesselman, Th.; Haarer, D. *Polymer Journal* **1987**, *19*, 61.

45. Gafert, J.; Friedrich, J.; Parak, F. *Proc. Natl. Acad. Sci. USA* **1995**, *92*, 2116.

46. Köhler, M.; Gafert, J.; Friedrich, J.; Falk, H.; Meyer, J. *J. Phys. Chem.* **1996**, *100*, 8567.

47. Milanovich, N.; Rätsep, M.; Reinot, T.; Hayes, J. M.; Small, G. J. *J. Phys. Chem. B*, **1998**, *102*, 4265.

48. Meixner, A. J.; Renn, A.; Bucher, S. E.; Wild, U. P. *J. Phys. Chem.* **1986**, *90*, 6777.

49. Kador, L.; Jahn, S.; Haarer, D.; Silbey, R. *Phys. Rev. B* **1990**, *41*, 12215.

50. Altman, R. B.; Haarer, D.; Renge, I. *Chem. Phys. Lett.* **1993**, *216*, 281.

51. Vauthey, E.; Holliday, K.; Changjiang, W.; Renn, A.; Wild, U. P. *Chem. Phys.* **1993**, *171*, 253.

CHAPTER 3. BIOLOGICAL CONSIDERATIONS

3.1. Introduction

The high resolution spectroscopic technique of hole burning and the underlying principles behind hole burning were introduced in Chapter 2. Application of this approach to the study of cellular systems also requires an understanding of the biological systems under study. Since the ultimate goal will be the application of spectral hole burning to the study of cellular aberrations, and, eventually, the early detection of diseases, *viz.*, cancer, then an understanding of the biology of a cell and cancer-related cellular abnormalities is necessary. Presented in this chapter is a description of cell biology as it pertains to changes in the physical properties (exploitable by hole burning) of cancer cells from that of normal cells. In addition, the characteristics of two well defined breast epithelial cell lines, one normal (MCF-10F) and the other cancerous (MCF-7), used as model systems, will be described. That nonphotochemical hole burning requires liquid helium temperatures to obtain high resolution hole spectra, means that cryogenic temperatures might have a significant effect on cellular structure and morphology. Therefore, these effects must be understood so that a suitable sample preparation methodology can be devised for studying cells at these temperatures. Absorption and fluorescence from endogenous biomolecules and components of the culture medium that might interfere with the hole burning of probe molecule is also discussed, as well as the biological behavior of the probe molecule, aluminum phthalocyanine tetrasulfonate (APT), chosen for the initial hole burning experiments on cellular systems which are reported in Chapters 4 and 5.

3.2 Cell and Cancer Biology

3.2.1. Biological Membranes —Structure and Function

Biological membranes of eukaryotic cells define the boundary of the cells and organelles. For a cell to survive, critical physiological processes must be carried out. To achieve this, the cell (plasma) membrane and organelle membranes prevent the disruption of these cellular physiological processes by serving as a barrier between the interior of a cell and the extracellular environment, or, in the case of organelles, between the organelle interior and the cytoplasm. Concomitantly, membranes of the cell are also semipermeable in that they are able to regulate transport across the membrane via the various lipids and proteins composing the membranes. By doing so, membranes of cells are able to maintain homeostasis.

In general, biological membranes are composed of amphiphatic lipid molecules (whose biochemical structures will be described in 3.2.1.1) having a hydrophilic head and a hydrophobic tail (Figure 3-1a) and, when in aqueous solution, spontaneously form a sheet-like bilayer between ~ 50 and 100 Å thick (Figure 3-1b). These molecules are arranged such that the hydrophilic heads of the lipid molecules form an interface with the water molecules of the solution while the hydrophobic tails are oriented away from the aqueous medium. Interactions between lipid molecules are strong enough to result in membranes having low permeability for ions and most polar molecules. As a result, proteins, e.g. ion channels, pumps and receptors, are present to regulate activity across a membrane. A general description of membrane-associated proteins will be given in Section 3.2.1.2.

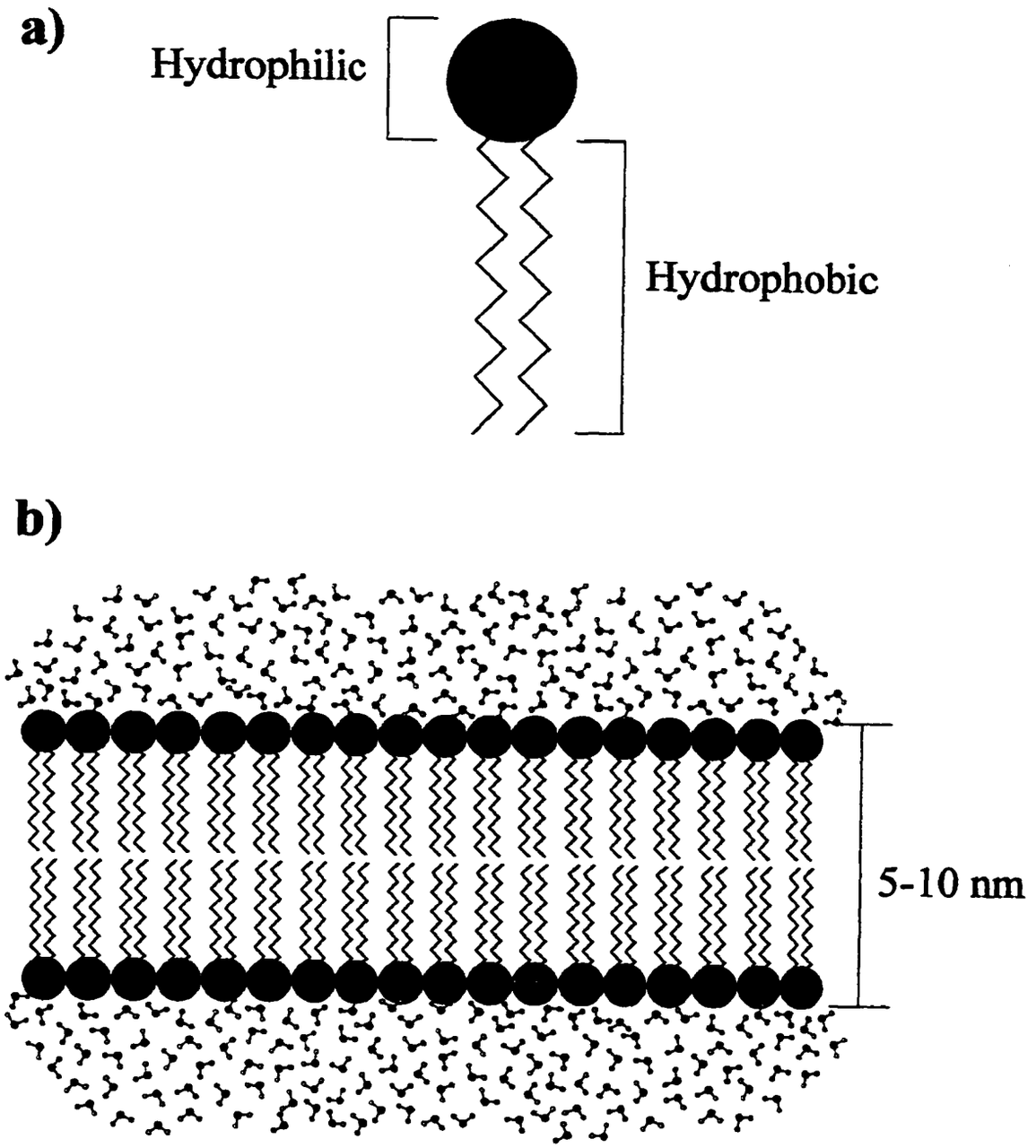

Figure 3-1. Schematic representation of a) the hydrophilic and hydrophobic portions of a typical amphiphatic plasma membrane lipid molecule and b) arrangement of a lipid bilayer in an aqueous solution.

3.2.1.1. Membrane Lipids [1, 2]

Lipid molecules found in eukaryotic cells can be categorized as one of three types: phospholipids, glycolipids, and sterols, *viz.*, cholesterol. The unbranched fatty acyl chains found in phospholipids and glycolipids make up the hydrophobic tail of the lipid and are typically between 14 and 24 carbons in length. The C-C bonds of the fatty acyl chain can be all single bonds (saturated fatty acid chain) or contain one or more double bonds (unsaturated fatty acid chain). Unsaturated chains adopt either a *cis* or *trans* conformation with the *cis* conformation being more common. The presence or absence of unsaturated fatty acyl chains within a membrane contribute to the fluidity of the membrane, which will be discussed in Section 3.2.1.3.

The first type of membrane lipids, phospholipids, are the major type of lipid and can be found in all biological membranes. These molecules are derivatives of either glycerol (**1**) or sphingosine (**2**) serving as the lipid backbone (Figure 3-2a). Phospholipids derived from glycerol are known as phosphoglycerides. They are formed by esterification of adjacent hydroxyl groups of glycerol with the carboxyl ends of two fatty acid chains and phosphorylation of the third hydroxyl group, resulting in phosphotidate. Addition of the alcohol moieties, serine, choline, ethanolamine, glycerol, and inositol to the phosphate group (see Figure 3-2a) results in the main group of phosphoglycerides.

In contrast to the many possible phospholipids derived from glycerol, sphingomyelin is the only phospholipid having a sphingosine backbone. Sphingomyelin consists of an unsaturated fatty acid chain forming an amide bond with the sphingosine and a phosphoryl

a)

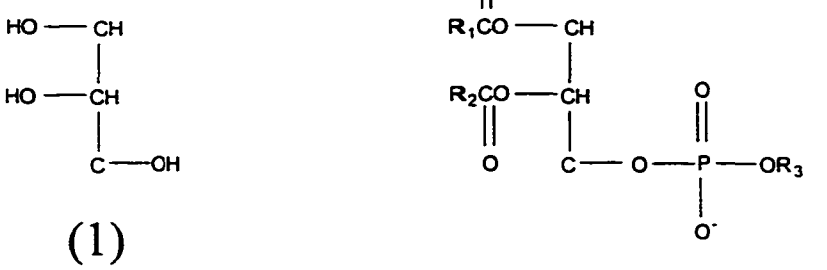

(1)

b)

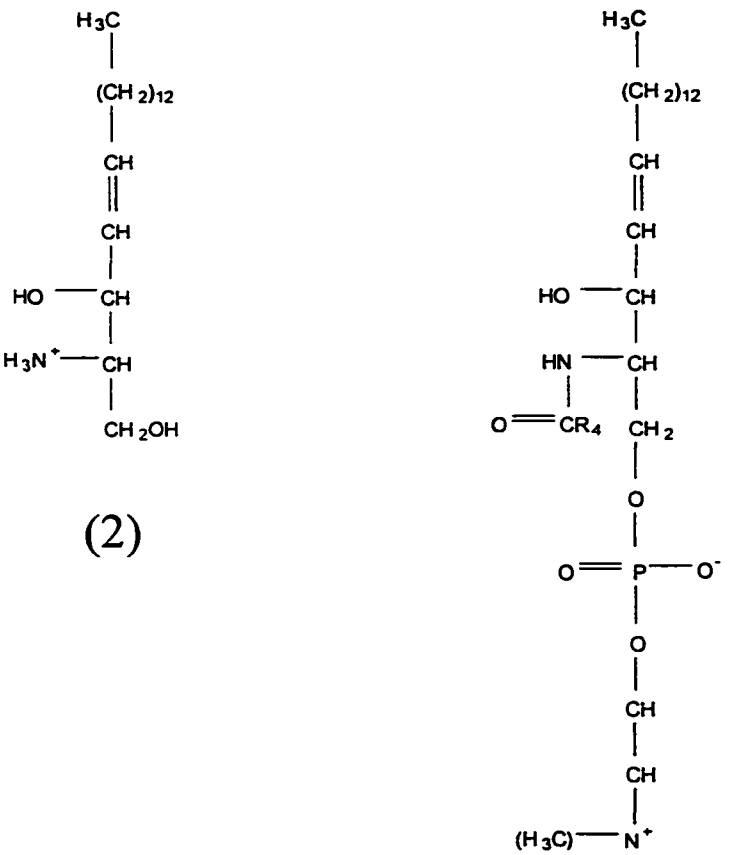

(2)

Figure 3-2. General structure of the two types of phospholipids: a) phosphoglycerides and b)sphingomyelin. R_1 and R_2 in a) represent saturated or unsaturated fatty acyl chains. R_3 is an alcohol, usually serine, choline, inositol, and ethanolamine. R_4 is an unsaturated fatty acyl chain.

choline group esterifiying the primary hydroxyl group of sphingosine (Figure 3-2b).

Glycolipids are the second type of membrane lipids and, like sphingomyelin, are derivatives of sphingosine with an associated fatty acid chain (sphingomyelin and the glycolipids are sometimes collectively referred to as sphingolipids). However, unlike sphingomyelin, the primary hydroxyl group of the sphingosine backbone contains one or more sugar groups (Figure 3-3a), which can be branched, e.g., as in gangliosides.

The third type of membrane lipid molecule is the sterol, cholesterol (Figure 3-3b). This lipid molecule is found in membranes and is an important factor regarding the fluidity of the cell membrane.

In general, the lipid composition of membranes will vary with cell type as will the distribution of lipid molecules within a particular membrane region. A heterogeneous distribution of lipid molecules throughout the plasma membrane will contribute to the asymmetric character of the cell membrane (see Section 3.2.1.3) and, thus, will give rise to physical properties of cell membranes that can be probed by hole burning (See Sections 3.2.2 and 3.2.3).

3.2.1.2. Membrane Proteins [3-6]

As mentioned in Section 3.2.1.1, membrane-associated proteins regulate activity occuring across cell membranes. The specific proteins expressed on a cell membrane and their amounts vary with the cell type and are dependent on a particular cell's function.

Membrane-associated proteins are classified as being either integral, or peripheral, depending on the ability to dissociate the protein from the membrane, with integral proteins

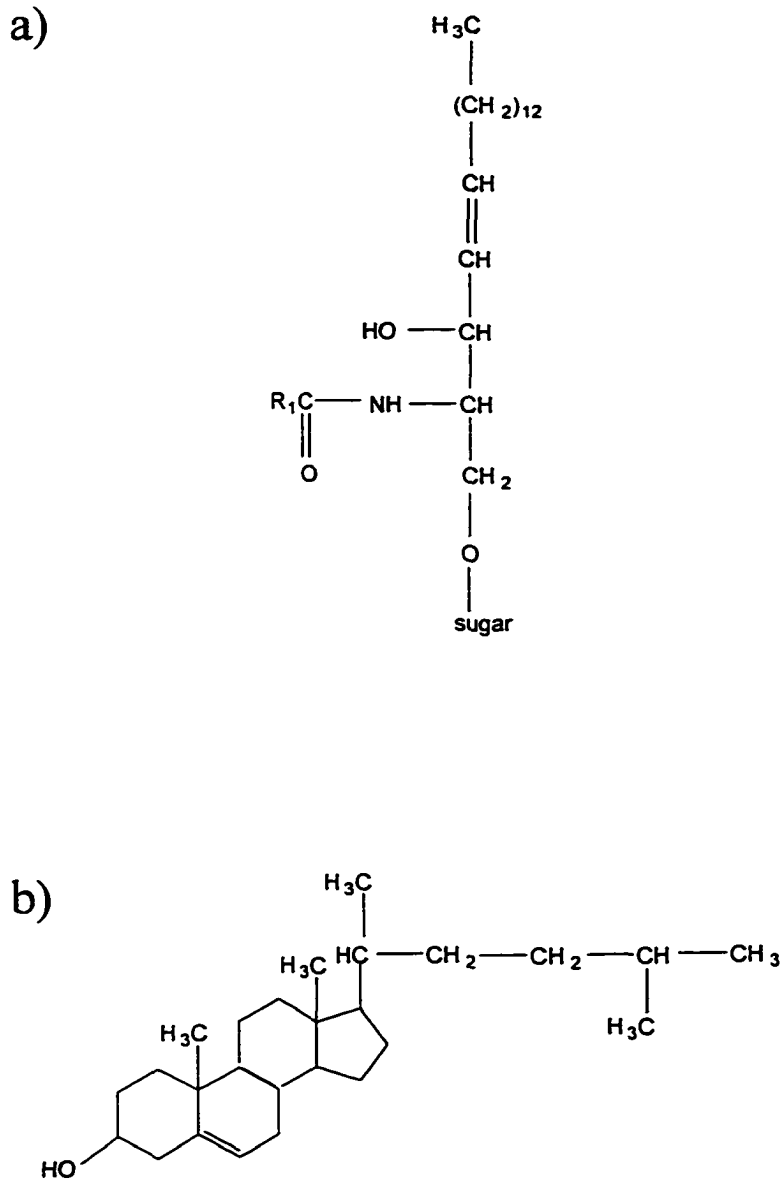

Figure 3-3. General structure of a) glycolipids and b) cholesterol. R_1 represents a fatty acyl chain.

being more difficult to dissociate than peripheral proteins (Figure 3-4). Examples of integral and peripheral proteins include ion channels and cytoskeletal proteins, respectively. Integral proteins sometimes span the length of a membrane one, or more, times (proteins of this type are referred to as transmembrane proteins) and are chemically amphiphatic, whereby the transmembrane domain of the integral membrane protein consists of nonpolar amino acid residues that form an α-helix. That the transmembrane domain contains nonpolar amino acid residues means that it is hydrophobic and, thus, forms strong interactions with the tails of membrane lipids. In turn, it stands to reason that the intracellular and extracellular domains of the integral membrane proteins are hydrophilic.

Unlike integral proteins, peripheral proteins are located along the intracellular surface of the lipid bilayer. Peripheral proteins are bound to the cell membrane by hydrogen bonds or electrostatic interactions with the hydrophilic portions of membrane lipids or integral proteins. An example of peripheral proteins is ankyrin, which links cytoskeletal proteins to the cell membrane (See Section 3.2.3).

3.2.1.3. Membrane Fluidity and Asymmetry

In the early 1970's, Singer and Nicholson [7] proposed the fluid mosaic model for cell membranes whereby lipid molecules of the cell membrane are able to diffuse along the membrane, known as lateral diffusion (diffusion coefficient ~10^{-8} cm^2/sec) [8] (Figure 3-5a). In addition to lateral diffusion, phospholipids, in particular, were later found to undergo transverse diffusion, more commonly referred to as flip-flop, whereby a phospholipid molecule "flip-flops" from one monolayer of the cell membrane to the other (Figure3-5b).

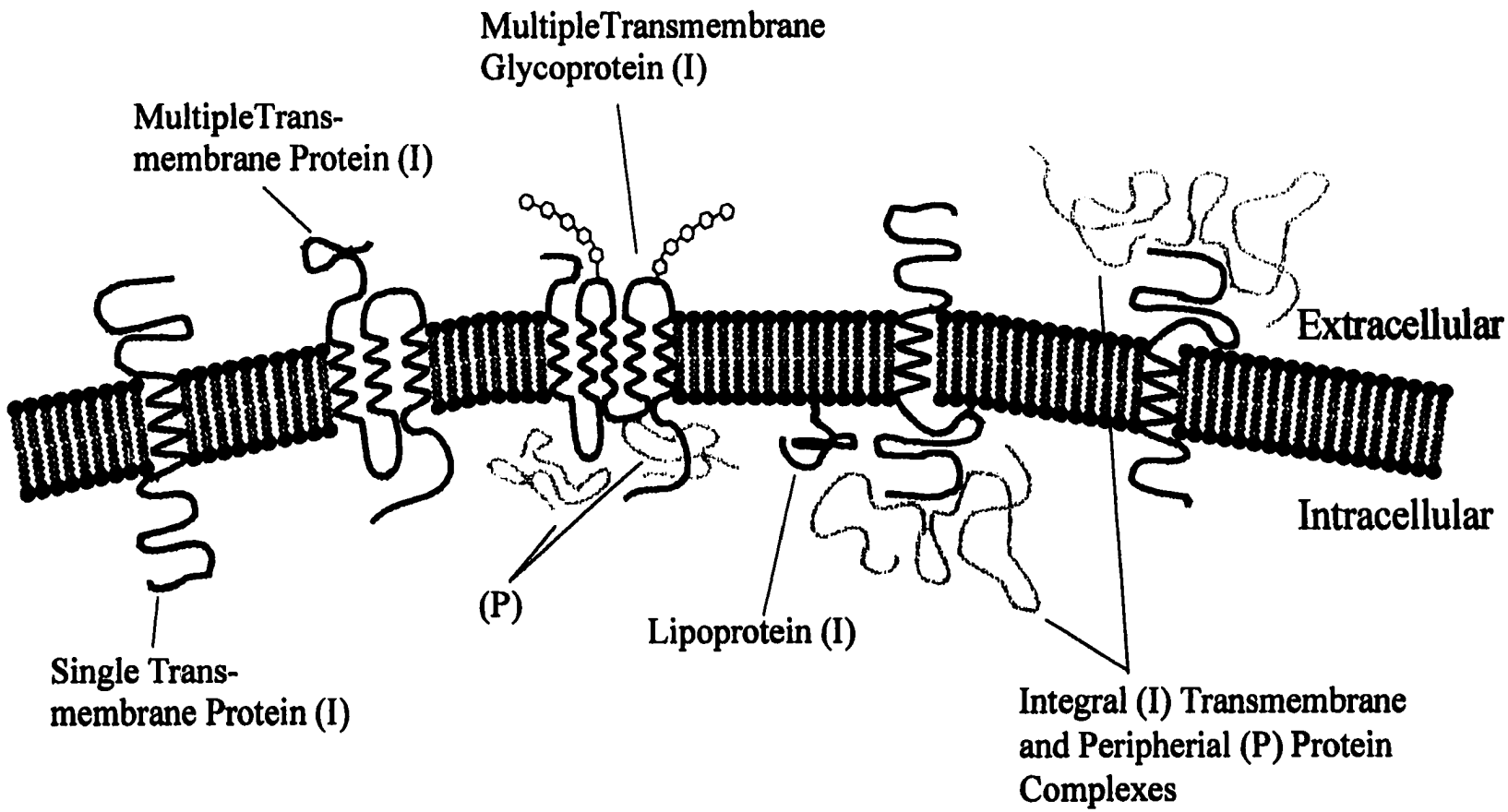

Figure 3-4. Association between integral (I) and peripheral (P) membrane proteins and the cell membrane.

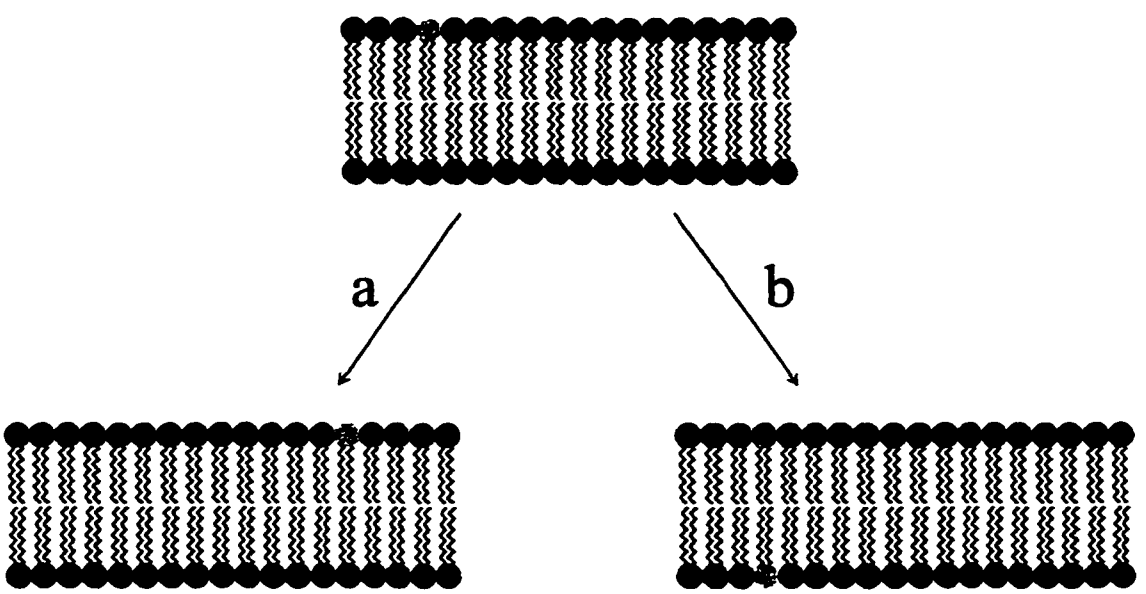

Figure 3-5. Membrane lipids can undergo (a) lateral diffusion and (b) flip-flop.

Relative to lateral diffusion, flip-flops occur less frequently (on the order of hours for one lipid molecule) and, in the case of glycolipids and membrane proteins, are not known to occur at all.

Fluidity of a cell membrane is affected by the molecular composition of the membrane and temperature. As mentioned in Section 3.2.1.1, lipid molecules with *cis* unsaturated fatty acyl chains disrupt the tight packing of adjacent lipid molecules, thus, increasing the fluidity of the cell membrane; an increase in temperature increases the fluidity of the membrane as well. In contrast, lipids with *trans* unsaturated fatty acyl chain as a well as saturated fatty acyl chains and cholesterol make the membrane more rigid and, in turn, decrease the fluidity.

In view of the fluid nature of a cell membrane, one would suspect that perhaps molecules of the cell membrane are homogeneously distributed throughout the membrane. However, the cell membrane is said to be asymmetric in that the inner and outer membrane surfaces have different molecular components and physiologic activities associated with them. (It should also be mentioned that the asymmetry of a cell membrane can also be described as polar. However, this meaning of polarity should not be confused with that pertaining to separation of charge). For instance, glycolipids and glycoproteins (proteins containing sugar moieties, e.g., ion channels) are only found on the extracellular half of the plasma membrane. Together these glycosylated molecules form a sugar coating around a cell known as the glycocalyx. The presence of sugars on the extracellular membrane region is thought to provide intercellular recognition between the different cells in a tissue and as

identifying markers by cells of the immune system. This contrasts phosopholipids, which can be found on both the extracellular and intracellular halves of the cell membrane. Nonetheless, certain phospholipids are found predominantly on either the intra-, or extracellular halves of the membrane bilayer, e.g., phosphatidylserine being found mainly on the intracellular region of the plasma membrane of red blood cells. Membane-associated proteins, as well, must be oriented in a specific way and delivered to a particular membrane region to ensure proper function of the protein and, subsequently, the cell. As will be discussed in Section 3.3, the plasma membrane of an epithelial cell is divided into domains with distinct lipid and protein compositions. It is this distinction of membrane domains, i.e., membrane asymmetry, that ensures the proper function of an epithelial cell, the breakdown of which has been implicated in diseases such as cancer [9, 10].

3.2.2. Biological Membranes —Electrical Properties [11-13]

All cell-associated membranes have electrical properties defined by the membrane structure, molecular composition, and function, and give rise to an overall electrical potential of the cell membranes. This overall electrical potential can be thought of as having two contributions: (1) a transmembrane potential, usually referred to simply as the membrane potential, and (2) surface potentials (charges). In general, the electrical properties of the cell membrane play a major role in the physiological processes of the cell [13]. Variations in a cells membrane potential and surface charge density have also been affected by diseased cells, such as cystic fibrosis cells [14] and cancer cells [13, 15, 16]. In the following discussion, a brief description of the aforementioned contributions to the electrical potential

of membranes is given and will be restricted to the plasma membrane. Nonetheless, these principles can, to an extent, be extrapolated to the electrical properties of organelle membranes, e.g., the mitochondrial membrane.

The transmembrane potential (henceforth referred to as the membrane potential) arises as a result of the differences in electrical charge between the intracellular and extracellular membrane regions. This difference in electrical charge can be created through either the electrogenic pumping or passive diffusion of inorganic ions in or out of the cell. The latter case is thought to be the dominant process occuring in animal cells and typically involves the ions K^+, Na^+, Ca^+, and Cl^- diffusing through ion-selective channels across the cell membrane. The driving force behind the flow of ions through a membrane channel is the electrochemical gradient present across the membrane. This electrochemical gradient is comprised of a concentration gradient and a voltage gradient of the ion across the cell membrane whereby one force drives the ions through the channel while the other force opposes the passage of ions. When these two forces balance each other, the result is no net flow of ions through the channel and the electrochemical gradient for the ion is zero. Therefore, the voltage gradient (i.e., the membrane potential) under this equilibrium condition is an equilibrium potential, more commonly referred to as a resting potential. The resting potential can be calculated by the Nernst equation given as

$$V = (RT / zF) In\left(\frac{C_o}{C_i}\right) \qquad (1)$$

where V is the resting potential in volts, R is the gas constant (2 cal $mol^{-1}K^{-1}$), T is temperature in Kelvin, z is the valence of the ion being considered, F is Faraday's constant

(2.3×10^4 cal $V^{-1}mol^{-1}$), and C_o and C_i are the ion concentrations on the outside and inside of the cell membrane, respectively. Oddly enough, despite the fact that several inorganic ions have concentration gradients across the cell membrane, the membrane potential in animal cells is thought to be caused predominantly by the K^+ leak channels present in a membrane (through which K^+ ions diffuse freely in and out of the cell) and the K^+ gradient. Alternate explanations to the view of passive diffusion of K^+ being the main cause of the resting potential have been proposed, but have not been widely accepted [17, 18]. Nevertheless, values for the resting potential range anywhere from -20 mV to -200 mV, with typical values of ca. -70 mV. The negative sign for the resting potential reflects the relative concentration of ions on either side of the membrane. It should also be noted here that changes in membrane permeability due to membrane excitation results in an action potential. This idea is best illustrated by the change in membrane permeability of neurons upon excitation.

Also associated with a cell membrane are surface charges that are the result of an asymmetric distribution of molecules (i.e., membrane proteins and lipids) comprising the membrane. These molecules give rise to surface charges as a consequence of charged groups on the molecules. Under physiological conditions, cells tend to be negatively charged due to the charged molecules found in the plane of the membrane and from the glycocalyx. Both positive and negative charges found in the membrane plane come about from hydrophilic regions of membrane proteins and phospholipids. Surface charges from phospholipids are mainly the result of the negatively charged hydrophilic head of phosphatidylserine, which has a $^-1$ charge. This membrane lipid is maintained on the inner layer of the membrane bilayer

by the ATP-driven pump aminophospholipid translocase. The glycocalyx, as mentioned in Section 3.2.1.3, is a coating of the outer membrane of the cell formed by the sugar moieties of glycoproteins and glycolipids. Portions of the sugar moieties distal to the protein or lipid contain neuraminic (sialic) acids which, under physiological pH, are dissociated, i.e., they are negatively charged. In general, the glycocalyx contributes a preponderance of the negative charge found on the extracellular side of the plasma membrane.

3.2.3. Cytoskeletal Structure and Function [19]

Found in eukaryotic cells, the cytoskeleton is comprised of a network of filamentous protein molecules that provide a cell with shape, contribute to cellular movement along a surface, movement of intracellular components (eg. organelles) through the cytoplasm, segregation of chromosomes during cell division, and mechanical strength. Protein filaments of the cytoskeleton are classified as being one of three types based on diameter: actin filaments, sometimes referred to as microfilaments (5-9 nm), intermediate filaments (10 nm), and microtubules (25 nm). These filaments are formed by the polymerization of specific protein subunits. Actin filaments and microtubules are composed of actin and tubulin subunits, respectively, whereas intermediate filaments can be formed from a variety of fibrous proteins, eg., keratin and vimentin. In conjunction with cytoskeletal proteins are various accessory proteins whose functions are to regulate filament polymerization and to link the cytoskeletal filaments to other cellular structures, eg., ankyrin, a peripheral protein, which links actin filaments to the interior periphery of the plasma membrane. In general, each filament type has a different arrangement within a cell which is determined by its

function (Figure 3-6).

Actin filaments (Figure 3-6a) are composed of thin, flexible actin protein subunits that combine to form a helix. These subunits are classified as one of three types: α-actin, found in muscle cells, and β-, and γ-actin, found in all other cell types, and all three subunits having a fast growing positive terminal and a slow growing negative pole. A mesh of actin filaments formed along the periphery of the cell membrane, known as the cell cortex, provides a cell with shape and mechanical strength through the attachment of actin-binding proteins as well as involvement in surface movements, phagocytosis, cytokinesis, and locomotion. A comparison of actin filaments in nonneoplastic and neoplastic cells by Tucker et al. [20] showed distinctive growth properties and morphological differences between the normal and transformed cells whereby the actin filaments in the latter were thin and sparse compared to the former. Furthermore, the Rho family of guanosine triphosphatases (GTPases), —part of the Ras (oncogene) superfamily of proteins— is thought to regulate transcription of the genes that encode the proteins of the actin filaments in the cell cortex via a receptor-activated Rac protein [21]. This regulation, in turn, influences morphogenesis, chemotaxis, axonal guidance, and the progression of the cell cycle.

Intermediate filaments (Figure 3-6b) are comprised of three general classes of nonpolar subunits, keratins, neurofilaments, and vimentin and vimentin-related filaments, which surround the cell nucleus and extend to the plasma membrane. They are important for cells that experience a lot of mechanical stress, eg. epithelial cells, which have tight junctions (see Section 3.3). Keratins, in particular, are abundant and characteristic of epithelial cells

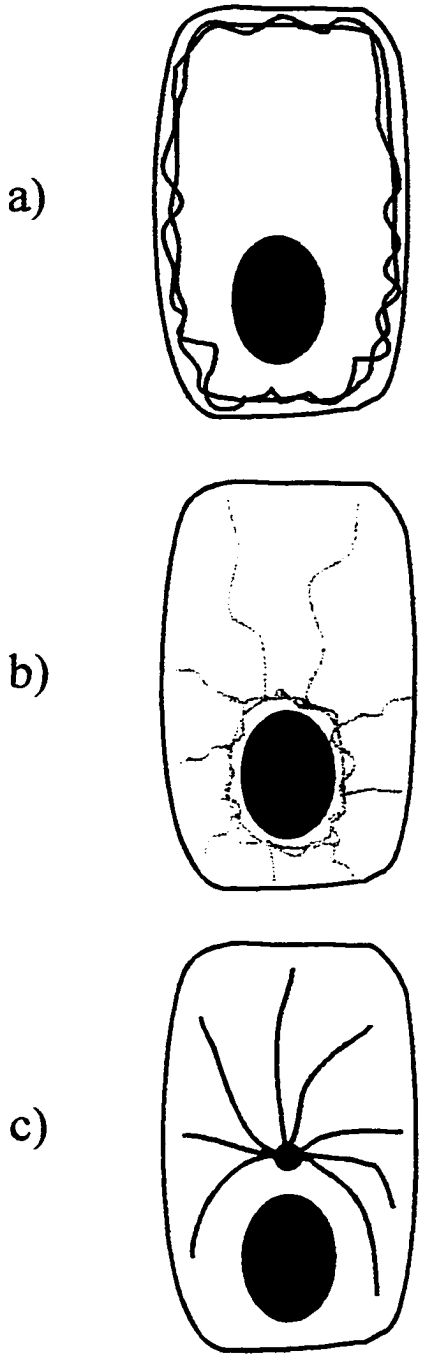

Figure 3-6. Arrangement of cytoskeletal filaments a) actin, b) intermediate filaments, and c) microtubules in a typical eukaryotic cell.

that actively proliferate, whereby one epithelial cell can have >20 types of keratin. In fact, the heterogeneity of keratins found in epithelial cells can prove useful in determining the origin of a carcinoma based on the specific keratins found in the tumor cells. Hynes and Destree [22] observed that a difference existed in the organization of intermediate filaments and their interactions with nuclei of NIL8 cells (a hamster cell line) and NIL8 cells transformed by hamster sarcoma virus. In addition, mutations of the protein subunits of intermediate filaments have been implicated in colorectal cancer and several other diseases [23].

Like actin filaments, microtubules (Figure 3-6c) consist of polarized protein subunits. These subunits are actually heterodimers of α- and β-tubulin whereby the negative terminal is embedded in centrosomes while the positive terminal grows and extends into the cytoplasm. Microtubules are primarily involved in the segregation of chromosomes during mitosis through the formation of mitotic spindles, which have made them targets of anticancer treatments. For instance, the anticancer agents, vinblastine and vincristine, are able to kill cancer cells (which undergo irregular cell division) by binding to free tubulin and, thus, preventing chromosomal segregation by inhibiting the formation of mitotic spindles. Another anticancer drug, taxol, unlike the two aforementioned drugs, stabilizes the polymerized microtubule filaments, but does not allow for the depolymerization of the mitotic spindles after chromosomal segregation.

3.3. **Epithelial Cells** [24, 25]

Tissues can be classified as one of four types: epithelial, connective, muscle, and nerve. Described in this section are epithelia which consist of epithelial cells arranged in a sheetlike fashion. These cellular sheets line the inner and outer surfaces of the body, eg. glandular ducts, inner walls of organs such as the intestines, and mucous membranes. Epithelial cells have a number of possible functions including endocrine and exocrine secretory functions in glands, absorptive functions in organs, and protective functions.

Epithelial cells can be classified based on three general morphological characteristics, as illustrated in Figure 3-7. The first classification is based on the number of cell layers. Cells having this morphological characteristic are either simple, stratified, or pseudostratified. Second, epithelial cells characterized by their surface cell shape are referred to as squamous, cuboidal, or columnar. Finally, epithelial cell morphology can be characterized by cell surface specialization whereby the cell surface is ciliated, or expresses many keratins. Note that epithelial cell tissues can exhibit a combination of these morphological traits.

An important characteristic of epithelial cells is that they are polarized and are, therefore, considered to be vectorial in that substances endocytosed at one membrane region of an epithelial cell are translocated and, subsequently, secreted at another membrane region. Polarization of epithelial cells is achieved by having three distinct membrane regions. (Figure 3-8): the apical membrane which faces the lumen of ducts and organs, the lateral membrane which is connected to adjacent epithelial cells, and the basal membrane which

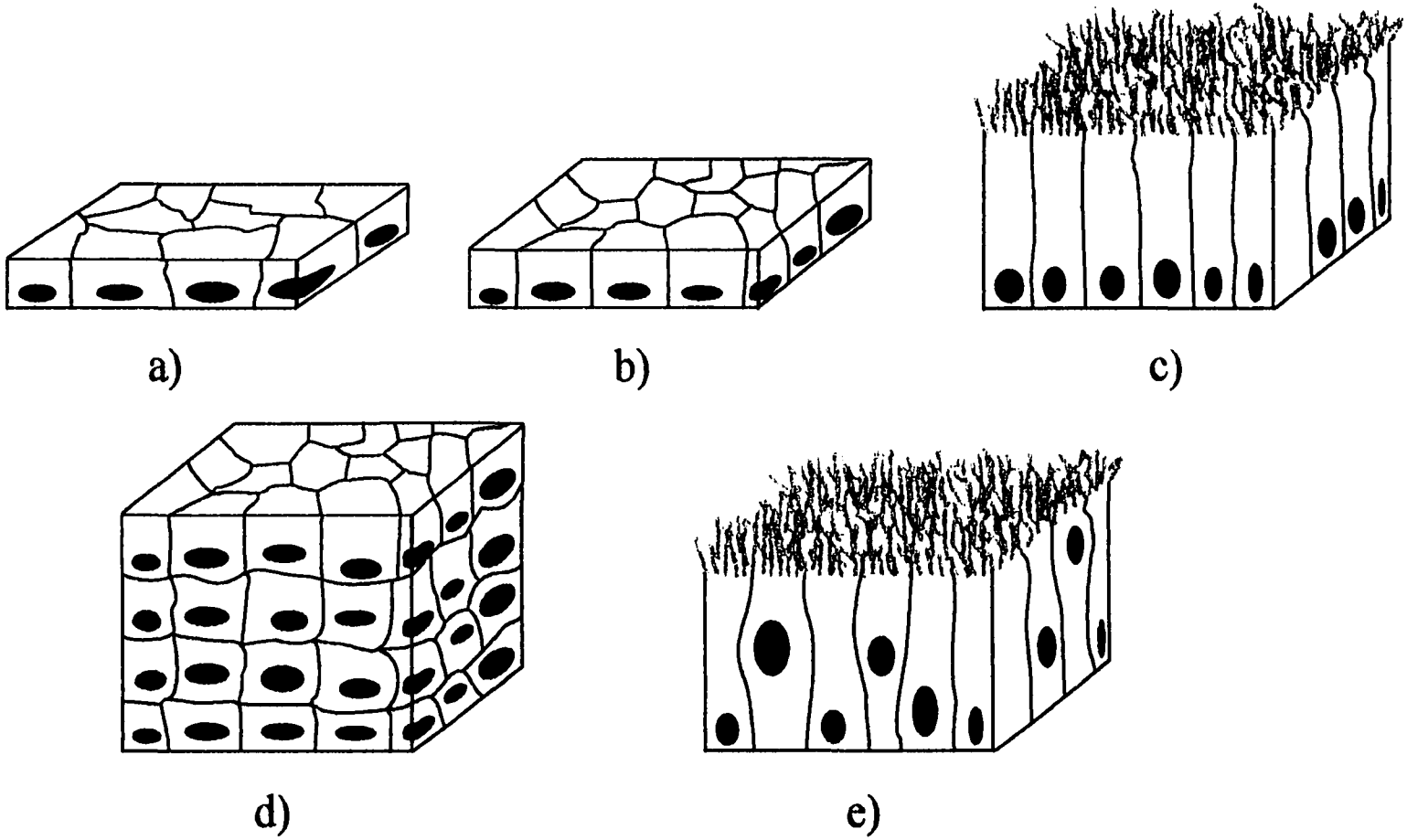

Figure 3-7. Epithelial cell types: a) - c) are examples of simple squamous, cuboidal, and columnar epithelia, respectively. Depicted in d) and e) are stratified (multilayered) and pseudostratified epithelia, respectively. The epithelia in c) and e) are ciliated (yellow).

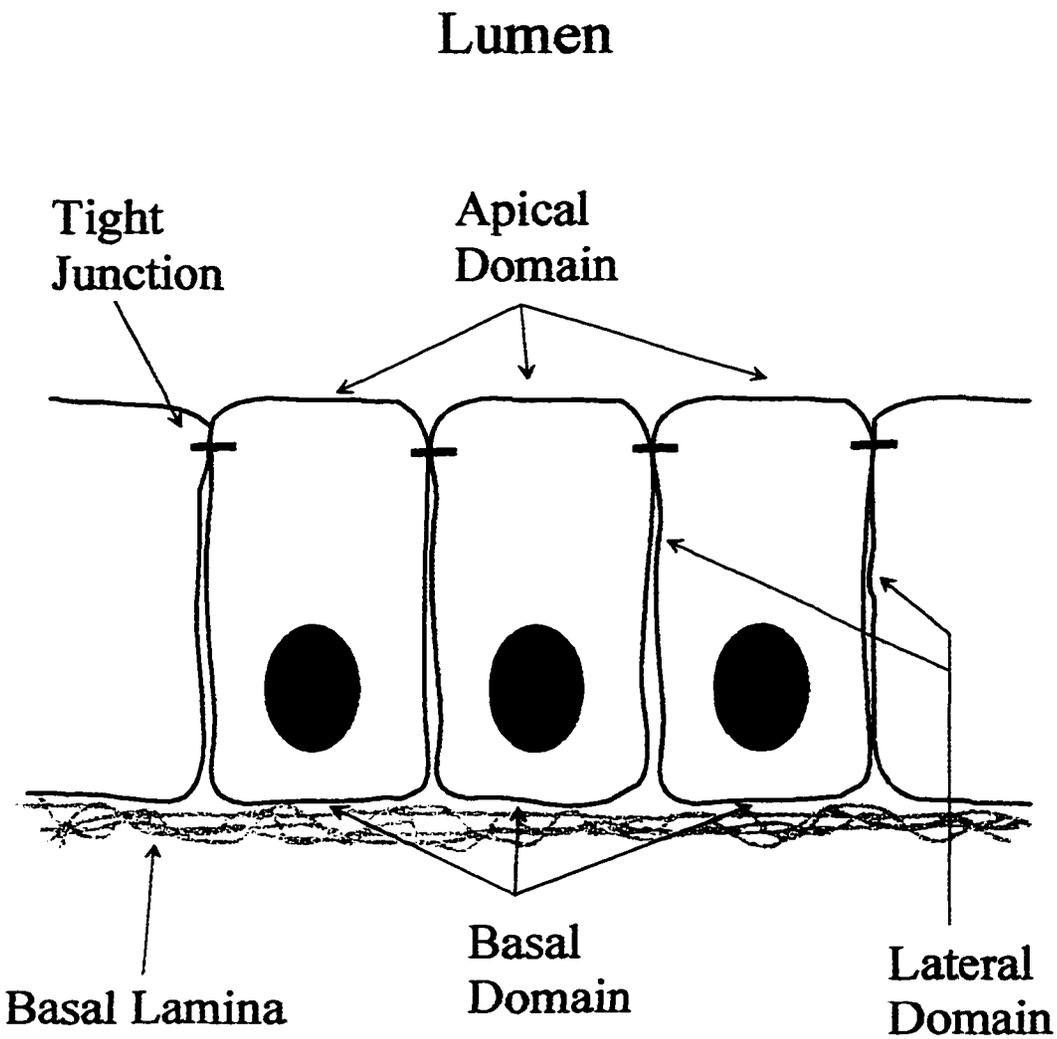

Figure 3-8. Typical epithelial cell arrangement and the distinct domains for a cell. The basal and lateral domains are collectively known as basolateral domain. Tight junctions form between adjacent epithelial cells to separate the apical and basolateral domains and to prevent diffusion of substances along the extracellular side of the lateral domain.

binds to basement membranes. (Note: the basal and lateral membrane regions are collectively known and will be referred to as the basolateral membrane region) The apical membrane is separated from the basolateral region by intercellular junctions known as tight junctions. These tight junctions prevent the free flow of substances along the lateral extracellular membrane domain of adjacent epithelial cells and keep the apical membrane biochemically distinct from the basolateral domain. This biochemical distinction is maintained from within the cell by a variety of mechanisms [10, 26, 27] and the polarized nature of the cells is varied by the identity and concentration of lipids and proteins present in a specific membrane domain. Therefore, a breakdown in the separation of the apical and basolateral membrane domains would incur a random redistribution of membrane proteins and lipids and, in turn, result in the loss of the polarized character of the cells. Loss of epithelial cell polarity is thought to be a characteristic of diseases such as cancer [9, 10].

3.4. Cell Lines

3.4.1. MCF-10F Cells

A mortal cell line, MCF-10M, was isolated from human fibrocystic mammary tissue [28]. This cell line was found to be a normal (diploid) human breast epithelial cell which, under typical Ca^{2+} concentrations found in culture media ($\geq$ 1.05 mM), senesced [28]. Despite senescence by the MCF-10M cell line, an immortal cell type, MCF-10, evolved spontaneously from the MCF-10M culture. In turn, two immortal cell sublines, one floating (MCF-10F) and the other adherent (MCF-10A) were derived from MCF-10 cells with the MCF-10F cells appearing at a low (~0.04 mM) Ca^{2+} concentration while the MCF-10A cells

evolved at a high (~1.05 mM) Ca^{2+} concentration [28]. Electron microscopic images determined MCF-10F and MCF-10A cells to be luminal ductal cells, which was verified by the presence of sialomucins and keratins [29]. Both cell types showed minimal chromosomal rearrangement and near diploidy [28]. Interestingly, the concentration of Ca^{2+} has a profound effect on cell morphology [29]. Grown in media with a normal Ca^{2+} concentration, MCF-10A cells are low cuboidal with many desmosomes and short microvilli. On the other hand, MCF-10F cells, grown in media with low Ca^{2+} concentration, are spherical and exhibit overall fewer desmosomes and a larger number of long microvilli. In general, the immortality and the natural evolution of MCF-10F and MCF-10A cells into culturable normal human breast cells have made these cells useful for in vitro studies of human proliferative breast disease (associated with high risk invasive breast cancer) and breast cancer [30, 31].

3.4.2. MCF-7 Cells

MCF-7 cells serve as a well-characterized in vitro model of a differentiated human breast epithelial tumor cell line having long-term differentiation and growth in culture (on the order of years). These cells were isolated and identified by Soule and coworkers in 1973 from the pleural effusion of a 69-year-old woman with malignant breast cancer [32]. They demonstrated that MCF-7 cells are, in fact, a human, subtetraploid cell line showing signs of differentiated mammary epithelial cell function based on dome formation in monolayer cultures. Further evidence that MCF-7 cells are differentiated mammary epithelial cells was verified by the presence of estrogen receptors [33, 34] and synthesis of α-lactalbumin (a

protein synthesized specifically by differentiated mammary epithelial cells) [35]. Three-dimensional growth of cultured MCF-7 cells on a collagen-coated cellulose sponge matrix demonstrated that the cells show retention of histologic characteristics similar to the primary tumor and pleural metastasis, *viz.*, formation of clusters and duct-like structures [36]. From such behavior in sponge culture, MCF-7 cells were concluded to be that of an adenocarcinoma (cancer of glandular epithelial cells). Further characterization of MCF-7 cells by Percoll gradient centrifugation show that these cells, grown in culture, consist of six subpopulations of varying density and are, thus, heterogeneous [37]. The six subpopulations included a small fraction (~5 %) of stem cells, which are hypothesized to give rise to the other five subpopulations. This would, in turn, imply that the six subpopulations separated by centrifugation are of the same origin, *viz.*, the stem cells, and simply represent MCF-7 cells at various stages of differentiation.

3.5. Cryobiology [38, 39, 40, 41]

Cryobiology pertains to the subjection of biological systems to temperatures typically ranging anywhere from subambient to liquid nitrogen at -196 °C (77 K). There are two main reasons for having biological systems be at cryogenic temperatures: preservation/storage and obtaining ultrastructural information. Preservation and storage include the preservation of food and retardation of food spoilage as well as preservation and storage of donor organs for use in transplantation. Moreover, cultured cell types used in basic research usually have a limited lifetime in vitro. For this reason, long-term cryogenic storage helps in maintaining a continuous supply of fully functional, differentiated cell lines. Low temperatures also

provide ultrastructural information about tissues and cells unobtainable at room temperature. In this way, the dynamics of structures in a cellular system are frozen-out, or cell and tissue components obstructing visualization of a desired structure are removed. Such ultrastructural information is obtained by the freeze-fracture, or freeze-etching of samples prior to microscopic analysis. From these two very different reasons for cryogenically freezing biological samples, it stands to reason that preparative measures will also differ, depending on the purpose for freezing. Since nonphotochemical hole burning requires cryogenic temperatures to obtain high-resolution spectra, low temperature effects on cellular systems must be considered and, subsequently, appropriate sample preparations devised for spectroscopic studies under such conditions. Therefore, this section will outline the cryopreparative procedures routinely used for low-temperature storage and ultrastructural analysis as well as their advantages and drawbacks. It should be kept in mind that preparative measures for cryogenic storage and ultrastructural studies are distinct and that neither procedure is, by itself, perfectly suitable for hole burning.

The fundamental problem confronting cryobiology comes from the high intrinsic water content in cells (~70% of total cell mass). Upon freezing, the normal phase transition of water is from a liquid at ambient temperature to ice at subambient temperatures. The problem of ice crystal formation at cryogenic temperatures is further complicated in a cell because cytoplasmic and extracellular regions vary in solute composition and concentration as well as the presence of semipermeable membranes providing membrane-water interfaces. When a cell is frozen, the progression of events is such that extracellular ice is formed first,

followed by intracellular ice. This ice formation disrupts the osmotic equilibrium across the plasma membrane, thus, resulting in dehydration and shrinkage of the cell along with denaturation, or aggregation of cellular proteins. As a result, preparative procedures have been developed to help attenuate the effects of ice in cells.

To minimize ice formation, variations in cooling rate, sample size, and addition of cryofixatives and cryopreservatives aid in making appropriate samples for cryogenic temperatures. Ideally, a sample can be cooled such that the water present vitrifies, ie., forms a glass, instead of crystallizing. Vitrification is important because it increases the likelihood of recovering proper cell function after thawing. However, vitrification of water would require a cooling rate of ~10^6 K/sec and, thus, the best possible scenario would be to cool as rapidly as possible to decrease the size of ice crystals formed within a cell. Furthermore, regions of the cell deeper into the interior will tend to cool slower than regions nearer to the plasma membrane, or extracellular regions. This results in a temperature gradient from the extracellular region to the interior of the cell and, in turn, gives a heterogeneous distribution of ice crystals within a cell. This effect can be minimized when studying subcellular structures by working with small sample sizes. However, such sample sizes are not practical when larger sample sizes are required, *viz.*, for long-term storage. The third way of controlling ice formation is by addition of a cryopreservative, eg., dimethyl sulfoxide (DMSO), or glycerol, to a sample prior to freezing. Nonetheless, low molecular weight cryopreservatives such as DMSO and glycerol are able to penetrate the cell membrane and can cause swelling, or cytotoxicity. In addition, the tendency for cryopreservatives to be

toxic is dependent on concentration of cryopreservative, temperature and time of exposure.

In light of the measures taken to preserve natural cell structure and function at cryogenic temperatures, *vide supra*, caution must be taken when manipulating any of the aforementioned variables to rid a sample of ice. Ultimately, sample preparation is determined by the purpose for using cryogenic conditions. A study of various freezing procedures performed on Chinese hamster fibroblasts by Farrant et al. [39] showed that for low-temperature microscopic studies rapid cooling (473 K/min) of small cell samples to 77 K (with 5% DMSO by volume) resulted in acceptable levels of ice formation, satisfactory ultrastructure, and no shrinkage. The disadvantage to this procedure is that, upon thawing, the cells are no longer viable. Therefore, even though this approach is adequate for ultrastructural studies, it is not suitable as a protocol for cryogenic storage. For storage purposes the authors proposed a two-step cooling procedure involving the addition of a cryopreservative. The first step in cooling would be slow, with a cooling rate of ~1 K/min down to ca. -70 °C, afterwhich the cells can be rapidly cooled to liquid nitrogen temperatures. Electron micrographs of Chinese hamster fibroblasts cooled in this manner were shrunken, but showed no ice formation. Rapid thawing of such samples would then assure that a majority of cells would be viable and recover proper cellular function. Note that for both the rapidly cooled sample and the sample cooled using a two-step cooling procedure, 5% DMSO was used as a cryopreservative. However, despite the presence of a cryopreservative, ice formed in the cells of the rapidly cooled sample because the cooling rate was too fast for the DMSO to behave as a cryopreservative and prevent ice formation. This inability of DMSO

to behave as a cryopreservative (i.e., prevent ice nucleation) was overcome by the slow-cooling step of the two-step cooling regime.

As can be seen, neither of these preparations, despite being routine, are necessarily suitable, or unsuitable, for hole burning studies of cellular systems. The rapid cooling regime would provide better preservation of cellular structures. However, ice, which is not present under the two-step cooling scheme, would not constitute an appropriate nonphotochemical hole burning system with a probe in a disordered matrix. As a matter of fact, the probe molecule, APT, which results in hole widths of hundreds of megahertz in amorphous water, will not hole burn in ice [42]. Nonetheless, the shrunken state of a cell having undergone two-step cooling may hinder efforts to differentiate between cell types based on compressibility. In Chapters 4 and 5, cell suspensions were prepared in the presence of a cryopreservative followed by two step cooling. In Appendix B, these results are compared to cells grown adherent to glass coverslips and rapidly cooled (i.e., room temperature samples are immersed into a liquid helium cryostat pre-cooled to ~4.5 K) in the absence of solution in an effort to simplify the sample preparation procedure and determine the effects of the suspension media used for the work presented in Chapters 4 and 5.

3.6. Biological Probes

3.6.1. Autofluorescence

Autofluorescence refers to fluorescence from endogenous biomolecules of unstained cells. Albeit a misnomer for the work in this dissertation, these biomolecules will be referred to as autofluorescent even though hole burning spectroscopy is actually concerned with

absorption, not emission. In mammalian cells autofluorescence comes from flavin coenzymes (flavin mononucleotide (FMN), flavin adenine dinucleotide and riboflavin) [43], reduced pyridine nucleotides (nicotinamide adenine dinucleotide (NADH) and nicotinamide adenine dinucleotide phosphate (NADPH)) [44], aromatic amino acids (phenylalanine, tryptophan, and tyrosine) and nucleic acids (adenine, thymine, guanine, cytosine, and uracil). [45] These biomolecules along with any absorbing/fluorescing components from the culture media and their respective absorption and emission maxima are summarized in Table 1.

Table 1. Absorption and emission maxima for endogenous biomolecules

Molecules/Biomolecules	λ_{abs} (nm)	λ_{em} (nm)
flavins	450	515
pyridine nucleotides	340	460
amino acids	~ 240-300	
nucleic acids	260	
phenol red*	560≠	578.4≠

*Abs/Em. for pH 7.4
≠Abs taken at ambient temperature and em. taken at 77 K.

Flavins and pyridine nucleotides are necessary for cellular metabolism [46] and amino acids and nucleic acids are essential components of proteins and DNA/RNA, respectively. In contrast, phenol red, which is commonly used as a pH indicator in culture media, is unimportant for cell viability. Therefore, removal of these essential biomolecules

from cells would be toxic whereas culture media without phenol red would be nontoxic, but, for the chosen systems, may have some uncharacterized physiological effect (the absence of phenol red may cause some physiological changes in MCF-10F cells by preventing estrogen receptors from "going away" [47]).

Autofluorescence becomes problematic when the level of fluorescent dye present in a sample is low enough such that the autofluorescent signal competes with that of the probe. Elaborate methods, mainly for flow cytometric applications, have been devised to overcome autofluorescent signals [48-51]. More recently, much simpler approaches have been taken to overcome autofluorescence. Many new dyes are now commercially available that absorb and emit in the same spectral region as the autofluorescent molecules, but are designed to "out-fluoresce" these endogenous chromophores when bound to the intended cellular target sites, even at low concentrations [52]. This approach is sufficient for microscopic and flow cytometric applications, but is not particularly useful for hole burning applications. For instance, phenol red, which is present in the suspension media of samples presented in this dissertation, will hole burn. This poses a problem in that a probe molecule whose absorption spectrum overlaps with phenol red absorption will result in competing hole burning processes and, in turn, difficult to interpret results. Fortunately, the absorption spectra of autofluorescent molecules and phenol red typically occur at wavelengths less than 600 nm. Therefore, dye molecules absorbing above 600 nm have the advantage of absorption bands that do not overlap those of autofluorescent species and, if hole burning is applied to tissues, longer wavelengths would penetrate tissues better than wavelengths where autofluorescing

species absorb. A class of dye molecules known as phthalocyanines are useful in this regard because their absorption maxima occur in ~670-680 nm range — well removed from that of autofluorescing species. The introduction of Chapter 4 gives an outline of the criteria used in selecting a probe molecule as well as brief background information on the hole burning characteristics and biological behavior of the dye molecule, aluminum phthalocyanine tetrasulfonate (APT). The next section gives a more extensive description of the biological behavior of APT.

3.6.2. Cellular Characterization of APT

Research using a variety of porphyrins and phthalocyanines as possible photosensitizers [53] in the area of photodynamic therapy (PDT) has offered much insight into the biological characteristics of these antitumor agents. Phthalocyanines such as APT are especially well suited for use as photosensitizers because their absorption maxima are removed from that of autofluorescent species and, in vivo, laser excitation at such wavelengths more easily penetrates tissue [54, 55]. Many permutations of side chains and chelated metal ions with phthalocyanines have been synthesized in an effort to develop a more effective PDT agent [53] (Figure 3-9). These permutations, in turn, have profound effects on the photosensitizer's biodistribution and pharmacokinetics in vivo and in vitro [53]. The current discussion will focus on the relevant findings of PDT research with APT as the photosensitizing agent.

Uptake studies of seven different sulfonated metallophthalocyanines [56] in chinese hamster fibroblasts, line V79-B310H, indicated that APT and uranyl phthalocyanine

a)

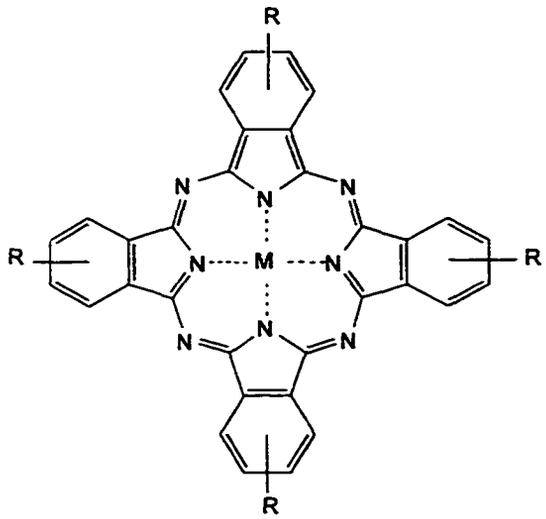

b)

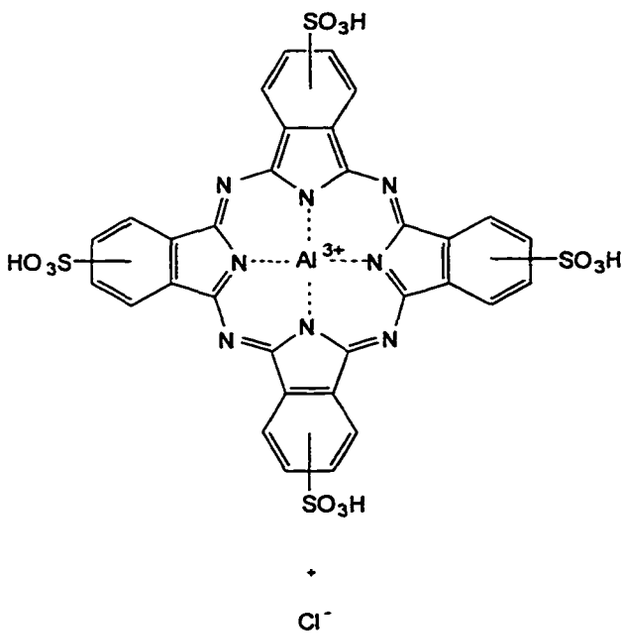

Figure 3-9. General molecular structure of a) phthalocyanines and the molecular structure for b) APT. M and R represent a variety of metals and side chains, respectively.

tetrasulfonate had the highest rates of uptake in culture medium containing 10 % fetal calf serum (FCS). In a serum-free medium APT had the highest uptake rate of the seven photosensitizers, nearly doubling that of the uranyl analog and increasing almost ten-fold compared to APT in medium with FCS. Moreover, only APT and silicon phthalocyanine tetrasulfonate exhibited no aggregation. This study further indicated that dye uptake was a two step process involving first receptor-mediated binding of the dye followed by internalization of the dye-receptor complex.

The degree of sulfonation was also shown to influence the uptake, retention [57-59], intracellular distribution [60], and cytotoxicity [59, 61] of the sulfonated aluminum phthalocyanines. In vitro studies using mono-, di-, tri-, and tetrasulfonated aluminum phthalocyanine in Colo 26 cells from murine colorectal carcinomas syngeneic to BALB/c mice indicated that uptake and retention of dye is inversely related to the degree of sulfonation [58]. In contrast, the authors found that uptake and retention in BALB/c mice increased with the degree of sulfonation in vivo. The results in BALB/c mice [58, 59] and in normal rat colon [61] are explained by the variability in hydrophobicity/hydrophilicity and, in turn, lipid solubility brought on by sulfonation, with the less sulfonated (more hydrophobic) species better able to bind lipoproteins, e.g. low density lipoproteins (LDL). [62] Once internalized, Peng and coworkers [60], using laser scanning confocal microscopy, found that mono- and disulfonated aluminum phthalocyanine exhibited diffuse fluorescence throughout the cytoplasm of human melanoma LOX cells while the tri-, and tetrasulfonated species showed granular fluorescence. Counterstaining with acridine orange verified that the

granular fluorescence was from dye localization within lysosomes. No fluorescence was detected in the nucleus from any of the dyes prior to sensitization. However, following light exposure, APT is released from the lysosomes and redistributed throughout the cytoplasm and nucleus of the LOX cells. This redistribution was also observed for V79 Chinese hamster fibroblasts treated with di- and tetrasulfonated aluminum phthalocyanine [63]. Confocal images of APT in MCF-10F and MCF-7 cells were similar to the LOX cells in that granular fluorescence from dye localized in lysosomes and diffuse fluorescence throughout the cytoplasm were observed for both cell lines. Proposed regions of PDT action for aluminum phthalocyanine having various degrees of sulfonation have included DNA [64, 65], cell membranes [66, 67] and mitochondria [67, 68], but APT was never detected in either the nucleus or mitochondria of MCF-10F and MCF-7 cells.

References

1. Stryer, L. *Biochemistry*; 3rd ed., W H. Freeman and Co.: New York, **1988**; p. 283.
2. Petty, H. R. *Molecular Biology of Membranes: Structure and Function*; Plenum Press: New York, **1993**; p. 7.
3. Petty, H. R., *Molecular Biology of Membranes: Structure and Function*; Plenum Press: New York, **1993**; p. 26.
4. Alberts, B.; Bray, D.; Lewis, J.; Raff, M.; Roberts, K.; Watson, J. D. *Molecular Biology of the Cell*, 3rd ed.; Garland Publishing: New York, **1994**; p. 477.
5. Wickner, W. T.; Lodish; H. F. *Science* **1985**, *230*, 400.
6. Sabatini, D. D.; Kreibich, G.; Morimoto, T.; Adesnik, M. *J. Cell Biol.* **1982**, *92*, 1.
7. Singer, S. J.; Nicholson, G. L. *Science* **1972**, *175*, 720.
8. Alberts, B.; Bray, D.; Lewis, J.; Raff, M.; Roberts, K.; Watson, J. D. *Molecular Biology of the Cell*; 3rd ed.; Garland Publishing: New York, **1994**; p. 480.

9. Fish, E. M.; Molitoris, B. A.; *New Eng. J. Med.* **1994**, *330*, 1580.

10. Rodriguez-Boulan, E.; Nelson, W. J. *Science* **1989**, *245*, 718.

11. Alberts, B.; Bray, D.; Lewis, J.; Raff, M.; Roberts, K.; Watson, J. D. *Molecular Biology of the Cell*, 3rd ed.; Garland Publishing: New York, **1994**; p. 523.

12. Glaser, R., In *Electromanipulation of Cells*; Zimmermann, U., Neil, G.A., Eds. CRC Press: New York, **1996**: p. 329.

13. Glaser, R., In *Biophysics of the Cell Surface*; Glaser, R., Gingell, D., Eds. Springer-Verlag: New York, **1990**; p. 173.

14. Ackerman, M. A.; Clapman, D. E. *New Eng. J. Med.* **1997**, *336*, 1575.

15. Petty, H. R., *Molecular Biology of Membranes: Structure and Function*; Plenum Press: New York, **1993**; p. 353.

16. Monen, S.H.; Schmidt, P.H.; Wondergem, R. *J. Membrane Biol.* **1998**, *161*, 247.

17. Bashford, C.L.; Pasternak, C.A. *J. Membrane Biol.* **1984**, *79*, 275.

18. Bashford, C.L.; Pasternak, C.A.*TIBS* **1986**, *11*, 113.

19. Alberts, B.; Bray, D.; Lewis, J.; Raff, M.; Roberts, K.; Watson, J. D. *Molecular Biology of the Cell*, 3rd ed.; Garland Publishing: New York, **1994**; p. 787.

20. Tucker, R. W.; Sanford, K. K.; Frankel, F. R. *Cell* **1978**, *13*, 629.

21. Hall, A. *Science* **1998**, *279*, 509.

22. Hynes, R. O.; Destree, A. T. *Cell* **1978**, *13*, 151.

23. Fuchs, E.; Cleveland, D.W. *Science* **1998**, *279*, 514.

24. Shaw, A. J., In *Epithelial Cell Culture: A Practical Approach*; Shaw, A.J., Ed. IPL Press at Oxford University Press: New York, **1996**; p. 1.

25. Junqueira, L. C.; Carneiro, J.; Kelley, R. O. *Basic Histology*, 7th ed.; Appleton and Lange: Norwalk, Connecticut, **1990**; p. 66.

26. Simons, K.; Fuller, S. D. *Ann. Rev. Cell Biol.* **1985**, *1*, 243.

27. Fuller, S.; von Bonsdorff, C.-H.; Simons, K. *Cell* **1984**, *38*, 65.

28. Soule, H. D.: Maloney, T. M.; Wolman, S. R.; Peterson, Jr., W. D.; Brenz, R.; McGrath, C. M.; Russo, J.; Pauley, R. J.; Jones, R. F.; Brooks, S. C. *Cancer Res.* **1990**, *50*, 6075.

29. Tait, L.; Soule, H. D.; Russo, J. *Cancer Res.* **1990**, *50*, 6087.

30. Bartow, S. A. *J. Natl. Cancer Inst.* **1993**, *85*, 1710.

31. Miller, F. R.; Soule, H. D.; Tait, L; Pauley, R. J.; Wolman, S. R.; Dawson, P. J.; Heppner, G. H. *J. Natl. Cancer Inst.* **1993**, *85*, 1725.

32. Soule, H. D.; Vazquez, J.; Long, A.; Brennan, M. *J. Natl. Cancer Inst.* **1973**, *51*, 1409.

33. Brooks, S.C.; Locke, E.R.; Soule, H.D. *J. Biol. Chem.* **1973**, *248*, 6281.

34. Lippman, M. E.; Bolan, G. *Nature* **1975**, *256*, 592.

35. Rose, H. N.; McGrath, C. M. *Science* **1975** *190*, 673.

36. Russo, J.; Soule, H. D.; McGrath, C.; Rich, M. A. *J. Natl. Cancer Inst.* **1976**, *56*, 279.

37. Resnicoff, M.; Medrano, E. E.; Podhajcer, O. L.; Bravo, A. I.; Bover, L.; Mordoh, J. *Proc. Natl. Acad. Sci. USA.* **1987**, *84*, 7295.

38. Franks, F. *J. Microscopy* **1977**, *111*, 3.

39. Farrant, J.; Walter, C. A.; Lee, H.; Morris, G. J.; Clarke, K. J. *J. Microscopy*, **1977**, *111*, 17.

40. Wisniewski, R. *BioPharm*, **1998**, *11*, 35.

41. Wolfinbarger, Jr., L. *BioPharm*, **1998**, *11*, 42.

42. Kim, W.-H.; Reinot, T.; Hayes, J. M;, Small, G. J. *J. Phys. Chem.* **1995**, *99*, 7300.

43. Benson, R. C.; Meyer, R. A.; Zaruba, M. E.; McKhann, G. M. *J. Histochem. Cytochem.* **1979**, *27*, 44.

44. Aubin, J. E. *J. Histochem. Cytochem.* **1979**, *27*, 36.

45. Cantor, C. R.; Schimmel, P. R. *Biophysical Chemistry, Part II: Techniques for the Study*

of Biological Structure and Function; W. H. Freeman and Co.: New York, **1980**; p. 377.

46. Alberts, B.; Bray, D.; Lewis, J.; Raff, M.; Roberts, K.; Watson, J. D. *Molecular Biology of the Cell*, 3rd ed.; Garland Publishing: New York, **1994**; p 610.

47. Djuric, Z. *Private Communication.*

48. Corsetti, J. P.; Sotirchos, S. V.; Cox, C.; Cowles, J. W.; Leary, J. F.; Blumberg, N. *Cytometry* **1988**, *9*, 539.

49. Hirschfeld, T. *J. Histochem. Cytochem.* **1979**, *27*, 96.

50. Roederer, M.; Murphy, R. F. *Cytometry* **1986**, *7*, 558.

51. Steinkamp, J. A.; Stewart, C. C. *Cytometry* **1986**, *7*, 566.

52. Haugland, R. P., *Handbook of Fluorescent Probes and Research Chemicals*, 6th Ed., Molecular Probes, Inc.: Eugene, Oregon. **1996**.

53. Boyle, R. W.; Dolphin, D. *Photochem. Photobiol.* **1996**, *64*, 469.

54. Spikes, J. D. *Photochem. Photobiol.* **1986**, *43*, 691.

55. Rosenthal, I. *Photochem. Photobiol.* **1991**, *53*, 859.

56. Ben-Hur, E.; Siwecki, J. A.; Newman, H. C.; Crane, S. W.; Rosenthal, I. *Cancer Lett.* **1987**, *38*, 215.

57. Tralau, C. J.; Barr, H.; Sandeman, D. R.; Barton, T.; Lewin M.R.; Bown, S.G. *Photochem. Photobiol.* **1987**, *46*, 7.

58. Chan, W. C.; Marshall, J. F.; Svensen, R.; Bedwell, J.; Hart, I. R. *Cancer Research*, **1990**, *50*, 4533.

59. Chan, W. S.; West, C. M. L.; Moore, J. V.; Hart, I. R. *Br. J. Cancer* **1991**, *64*, 827.

60. Peng, Q.; Farrants, G. W.; Madslien, K.; Bommer, J. C.; Moan, J.; Danielsen, H. E.; Nesland, J. M. *Int. J. Cancer*. **1991**, *49*, 290.

61. Chatlani, P. T.; Bedwell, J.; MacRobert, A. J.; Barr, H.; Boulos, P. B.; Krasner, N.; Phillips, D.; Bown, S. G. *Photochem. Photobiol.* **1991**, *53*, 745.

62. Wagnières, G. A., Star, W. M., Wilson, B. C. *Photochem. Photobiol.* **1998**, *68*, 603.

63. Moan, J.; Berg, K.; Anholt, H.; Madslien, K. *Int. J. Cancer*. **1994**, *58*, 865.

64. Ramakrishnan, N.; Clay, M. E.; Xue, L. -Y.; Evans, H. H.; Rodriguez-Antunez, A.; Oleinick, N. *Photochem. Photobiol.* **1988**, *48*, 303.

65. Zaidi, S. I. A.; Oleinick, N. L.; Zaim, M. T.; Muktar, H. *Photochem. Photobiol.* **1993**, *58*, 771.

66. Wilson, A. C.; Malham, G. M.; Thomsen, R. J.; Harvey, J. D.; Baguley, B. C. *J. Clin. Neuroscience* **1996**, *3*, 252.

67. Müller, M.; Reich, E.; Steiner, U.; Heicappell, R.; Miller, K. *Eur. Urol.* **1997**, *32*, 339.

68. Ben-Hur, E.; Green, M.; Prager, A.; Kol, R.; Rosenthal, I. *Photochem. Photobiol.* **1987**, *46*, 651.

CHAPTER 4. ALUMINUM PHTHALOCYANINE TETRASULFONATE IN MCF-10F, HUMAN BREAST EPITHELIAL CELLS: A HOLE BURNING STUDY

A paper published in the *Biophysical Journal* **1998,** *74,* 2680

N. Milanovich, T. Reinot, J. M. Hayes and G. J. Small

4.1. Abstract

Laser-induced holes are burned in the absorption spectrum of aluminum phthalocyanine tetrasulfonate (APT) in MCF-10F, human breast epithelial cells. The hole burning mechanism is shown to be non-photochemical. The fluorescence excitation spectra and hole spectra are compared with those of APT in hyperquenched glassy films of water, ethanol, and methanol. The results show that the APT is in an acidic, aqueous environment with a hydrogen bonded network similar to that of glassy water, but showing the influence of other cellular components. Pressure shifts of holes allow the local compressibility about the APT to be determined.

4.2. Introduction

Biological samples when subjected to cryogenic temperatures display an inherent disorder which gives these samples glass-like properties. Thus, high resolution optical techniques such as fluorescence line narrowing (FLN) [1] and hole burning [2] which have been developed to probe the inhomogeneously broadened absorption spectra of impurity molecules in glasses are increasingly being used to investigate biological samples. FLN, for example, has been used to study DNA-carcinogen complexes at physiological damage levels

[3, 4] and protein-chromophore interactions [5]. Hole burning has been used extensively to study electron and energy transfer processes in photosynthetic systems [2, 6, 7]. Because the band widths obtained by these techniques are so narrow compared with room temperature absorption widths, Stark shifts and broadening [8, 9] and pressure effects [10-17] on the spectra can be accurately measured.

In this paper, we report the results of hole burning and pressure shifts for a dye molecule within cultured mammalian cells. The results reported here represent the first measurements of hole burning and compressibility for dye molecules within intact cells. The hole burning mechanism will be shown to be non-photochemical hole burning, NPHB, which occurs due to rearrangement of the matrix solvating the dye rather than due to photochemistry of the dye itself. The mechanisms and properties of NPHB have been extensively studied both by us [18-20] and by others [21] and NPHB properties have been shown to be extremely sensitive to the molecular environment of the dye molecule [22, 23]. The demonstration in this paper of NPHB of a dye molecule within cells opens up the possibility of utilizing hole burning using organelle specific dye molecules to "image" anomalies in sub-cellular structures. As differences in hole burning parameters such as hole width and hole growth kinetics are related to differences in T_2 optical relaxation, while hole shifts with pressure and temperature are determined by short range solvent forces, hole burning imaging is directly analogous to magnetic resonance imaging which measures proton T_1 relaxation times to detect differences in tissue structures.

Application of hole burning to a cellular system requires careful selection of an

appropriate dye molecule that can be detected within the cell. In choosing a dye certain important biological and spectroscopic criteria must be satisfied. First, the probe molecule used must be membrane permeable. Second, autofluorescence caused by other biomolecules present inside the cell may have spectra that interfere with the probe molecule's spectrum. In mammalian cells, such as those used in this study, autofluorescence is primarily caused by flavin coenzymes (FAD and FMN, abs./em. ~450/515 nm) [24] and reduced pyridine nucleotides (NADH, abs./em. ~340/460 nm) [25]. In addition, the presence of the pH indicator phenol red (abs./em. 560/578.4 nm, pH ~7.4, at room temperature and 77 K, respectively), used in culture media, may also interfere with the probe molecule's spectra. Interference from autofluorescence and phenol red fluorescence suggest that a dye absorbing and fluorescing at wavelengths greater than 600 nm would be best suited. In general, longer wavelengths will penetrate tissues better than shorter wavelengths. Third, the dye should be dispersed throughout the cell while not undergoing a chemical reaction. Finally, the dye molecule must hole burn, i.e., it must be in a disordered environment and have sufficient coupling to the environment that electronic excitation will trigger solvent rearrangement, and it must be photochemically stable and not aggregate.

In choosing an appropriate dye molecule we were guided by considering photosensitizers used in photodynamic therapy (PDT). PDT is a cancer treatment method based on photooxidation of intracellular biomolecules of the targeted cells initiated by a photosensitized dye molecule [26]. What makes these photosensitizers ideal is that cells are able to uptake these molecules. Many photosensitizers have been under consideration for use

as photodynamic dyes. These dye molecules retain the basic "core" structure of either a porphyrin or a phthalocyanine ring while differences in uptake and biodistribution are determined by the sidechains and/or metals associated with the molecule's core [27]. Phthalocyanines, in particular, have absorption maxima in the 670-680 nm range. In the current study we have chosen aluminum phthalocyanine tetrasulfonate (APT) to stain cells in vitro. Although APT is not organelle specific, it has been used as a probe molecule for studying disorder in amorphous water [22, 28-31] and, therefore, its hole burning behavior is well characterized. Much work has also been done using APT as a photodynamic dye [32-34]. Ben-Hur *et. al.* investigated the uptake of several tetrasulfonated metallophthalocyanines in Chinese hamster cells [35]. They found that of the seven metallophthalocyanines considered, uranyl phthalocyanine tetrasulfonate and APT were taken up at the highest rate and that APT was one of only two metallophthalocyanines to not aggregate under physiological conditions. The authors further add that the dye molecules make their way into the cell first by binding to a cell-surface receptor followed by the internalization of the receptor-ligand complex. Confocal laser scanning microscopy of APT in human melanoma cells indicates that the internalized dye molecules can be found in lysosomes [36].

We report here the hole burning of APT inside MCF-10F human mammary epithelial cells [37, 38]. The cells were stained with APT, at which time the cells were prepared for study at liquid helium temperatures (~4.5 K). Spectra obtained for APT in MCF-10F cells were compared to those for APT in hyperquenched glassy water, ethanol, and methanol. We

also present here the results of pressure effects on the center frequency of holes burned in APT's fluorescence excitation spectrum and, subsequently, determine the compressibility of the dye in MCF-10F cells. In general, we are interested in detecting cellular anomalies so that we might eventually apply NPHB to the early detection of disease.

4.3 Experimental

Cell Culture MCF-10F human mammary epithelial cells were obtained from the American Type Culture Collection (ATCC). MCF-10F cells were cultured in a 1:1 mixture of Ham's F12 medium and Dulbecco's modified Eagle's medium containing 5% horse serum, 100 ng/ml cholera enterotoxin, 10 μg/ml insulin, 0.5 μg/ml hydrocortisol, and 20 ng/ml EGF. All cell culture items were purchased from Sigma-Aldrich Chemical Co. (St. Louis, MO) The cells were grown in 25 cm^2 culture flasks and incubated at 37 °C under an air atmosphere containing 5% CO_2; cells were passed weekly.

Sample Preparation For sample preparation, cells were grown in 75 cm^2 culture flasks. Cells were allowed to grow to near confluence at which time sterile-filtered APT (Porphyrin Products, Login, UT) in phosphate buffered saline (PBS) was added to the culture flasks. Final APT concentration in the culture flasks was adjusted to 10^{-4} M. Samples were then incubated overnight (18-19 h) at 37 °C under a 5% CO_2 atmosphere. After incubation the culture media containing excess APT were removed from the flasks and the cells were washed three times with PBS to remove excess dye and media. Washed cells were detached from the flasks by treating the cells with trypsin. Following trypsin treatment the appropriate culture medium was added to each flask 1:1 with trypsin and cell population was determined

using a Coulter Multisizer II cell counter. Typical cell populations ranged from 1 x 10^6 to 3 x 10^6 cells/ml. Samples were then centrifuged for 5 min. at 100g and the resulting supernatant was discarded. The cells were resuspended in freezing medium, which consisted of the appropriate culture medium with 5% DMSO. Aliquots of these samples were mixed 1:1 with glycerol and transferred to 5 mm o.d. gelatin capsules. Final samples typically contained between ~10^5 and 3 x 10^5 cells. Because a cryopreservative was used (DMSO), the samples were slow-cooled to -70 °C in a styrofoam box inside a freezer overnight to avoid ice formation in the cells at cryogenic temperatures [39, 40].

Cell Viability Stained MCF-10F cells were tested for viability using a Coulter EPICS XL-MCL flow cytometer. A frozen sample, as prepared above, was rapidly thawed and stained with propidium iodide (PI) (Molecular Probes, Inc., Eugene, OR). Cell viability was determined by PI uptaken. Non-viable cells are able to take up the dye while viable are not. Typically, viability was > 90% and nearly no debris resulting from ruptured cells was present.

High Pressure System Pressures used in this study were attained with standard gas cylinder pressures and helium gas was used as the pressure transmitting medium. Gas pressure applied to the sample was manually regulated by a Model E11-8-N115H two-stage pressure regulator (Air Products, Des Moines, IA). In-line with the pressure regulator was a PX945-3KGI pressure transducer (0-20.7 MPa detection range with 0.1% accuracy) and model DP941-E pressure readout (both from Omega Engineering, Stamford, CT). 316 stainless steel tubing (I.D. 1/8") was used to connect the cylinder regulator and pressure transducer. A

reducing union reduced the tubing diameter to 1/16". The 1/16" gas delivery line was connected at the head of the sample holder with a bulkhead union. Inside the cryostat head, 1/16" tubing connected to the other end of the bulkhead union was wrapped along the length of the sampleholder's shaft for thermal grounding. A male connector joined the gas delivery line to the high pressure cell. All connectors were SWAGELOK.

The high pressure cell is made of copper with horizontal cross-section of 1 1/8" x 1 1/8" and a height of 2". The schematic in Fig. 4-1 is a vertical cross-section of the cell. Windows made of antireflection coated BK7 glass (1/8" thickness, 1/2" diameter) (Melles Griot, Irvine, CA) on three of the cell's four vertical sides provided optical access to the sample. Windows were glued to window mounts with low temperature epoxy (Janis Research Co., Wilmington, MA) and the window mounts were then secured to the cell body. An O-ring made of Indium metal provided the seal between the window mount and the cell body.

In an experiment, a single sample contained in the above described gelatin capsule was placed inside the pre-cooled (-70 °C) high pressure cell. After placing the sample inside the cell, the male connector mentioned above was screwed into place. One-inch copper spacers were placed between the mounting plate of the sampleholder and cell to allow for easy connection of the delivery line with the cell. At low temperatures (< 40 K), gases inside the pressure delivery line, i.e. oxygen and nitrogen from air, will solidify and prevent the delivery of gas pressure to the sample. Therefore, the delivery line was continuously flushed with helium as the cell and delivery line were being connected. Consequently, a small

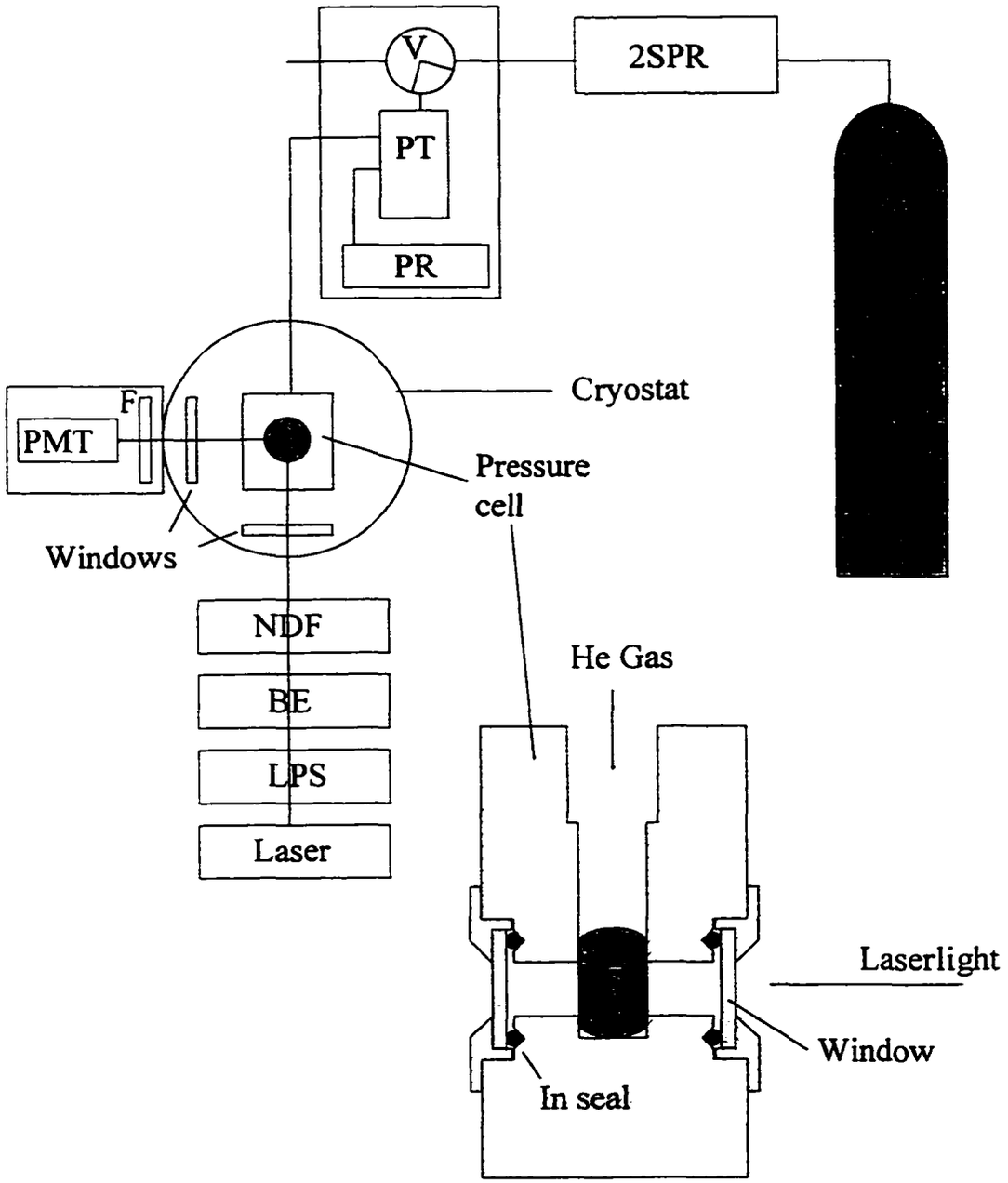

Figure 4-1. Schematic representation of experimental apparatus showing details of the high pressure system. S, sample; NDF, neutral density filter; BE, beam expander; LPS, laser power stabilizer; PMT, phtomultiplier tube; F, filter; PR, pressure readout; PT, pressure transducer; V, valve; 2SPR, two-stage pressure regulator; He, helium gas cylinder.

pressure remained inside the cell (~ 100 kPa) until the cell was inserted into a pre-cooled (~4.5 K) cryostat (Supertran Continuous Flow Cryostat, Janis Research Co., Wilmington, MA) at which time the pressure decreased to ambient pressure (defined as 0 kPa). That the delivery line was unobstructed was checked by allowing the cell to cool to ~4.5 K and applying between 30 and 70 kPa of pressure to the cell. Temperature rose rapidly by 1-3 K if the delivery line was not obstructed, at which time pressure was dropped to ambient and the temperature returned to ~4.5 K. Temperature of the sample was monitored using a silicon diode (Lakeshore Cryogenics Model DT-470, Westerville, OH) in direct contact with the high pressure cell.

Laser system The fluorescence excitation system used has previously been described [30, 31]. Briefly, a Coherent Innova 90-6 Argon ion laser (Coherent, Inc., Santa Clara, CA) was used to pump a CR-699-29 ring dye laser using DCM special laser dye (Exciton, Dayton, OH). This dye gives 100-600 mW power over a wavelength region of 610-700 nm. Laser intensity was stabilized with an LS100 laser power stabilizer (Cambridge Research and Instrumentation, Cambridge, MA) and, subsequently, the laser beam was expanded with a telescope. The laser was operated in two modes: broad range continuous scanning without intracavity etalons and short range scanning with intracavity etalons. The scanning ranges and line widths for the broad scanning mode and short range mode were 1000 cm^{-1} and 0.4 cm^{-1} , and 10 cm^{-1} and < 30 MHz (.001 cm^{-1}), respectively.

Hole burning and scanning intensities were varied using a series of neutral density (absorption) filters. Laser beam intensities used for detection were chosen so as not to further

alter the spectra. The estimated change in fractional hole depths at each wavelength was less than 0.0005 for channel time t=0.2 s and intensity I=60 nW/cm^2 (see Fig. 4, where the burn intensity is 1.7 μW/cm^2). For kinetics curve detection, burn intensities less than 2 μW/cm^2 were used while concurrently recording a decrease in fluorescence signal. Because the fluorescence signal decreases very rapidly during the first few seconds of burning, and much slower later, the typical channel time in the beginning was 0.1 s. After approximately half of the burn was completed channel time was changed to 1 s.

Fluorescence excitation signal was collected with a GaAs photomultiplier tube (PMT) and photon counter (Stanford Research, SR-400, Sunnyvale, CA). Excitation signal was filtered from the PMT with cut-off filters at 750 nm. The laser was scanned and data was collected with a PC.

4.4. Results and Discussion

The fluorescence excitation spectrum of APT-treated MCF-10F cells at 4.5 K is shown in Fig. 4-2. The figure also shows the fluorescence excitation spectra of APT in freezing media, in hyperquenched glassy water, and in glassy ethanol. Comparing the spectra of APT in freezing media with that in cells, it is apparent that there is a large shift in the fluorescence excitation maxima of the spectra in the former and the spectrum is also considerably broader than that in cells. These differences between the freezing media spectrum and the spectrum in cells are conclusive evidence that the APT in the cellular samples is associated with the cells rather than simply dissolved in the suspension medium. The width of the freezing media spectrum indicates that there is a wide variety of

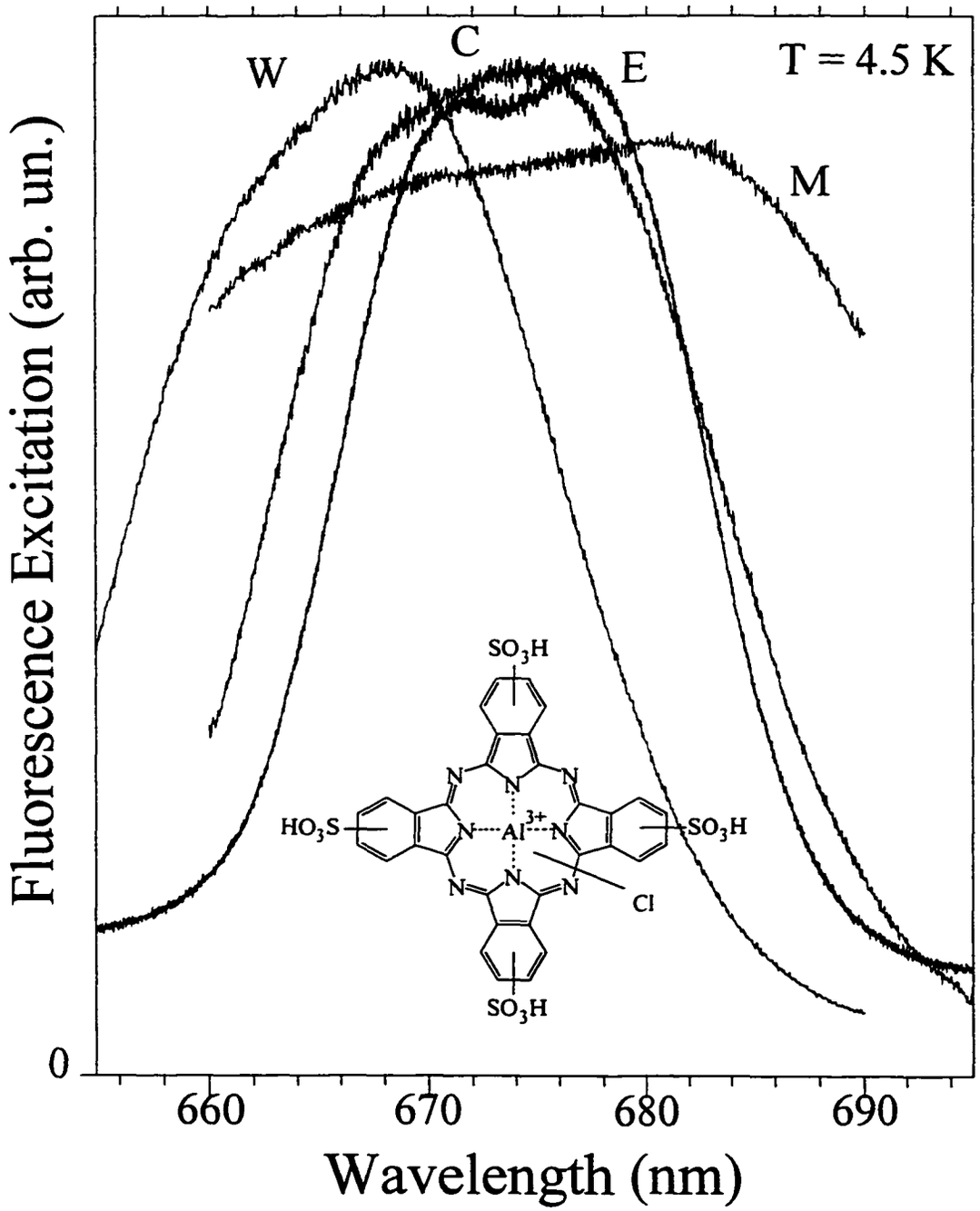

Figure 4-2. Fluorescence excitation spectra of APT in various glassy matrices. The curves are W, water (λ_{max}= 668.2 nm); C, MCF-10F cells in 1:1 freezing medium and glycerol λ_{max}= 675.4 nm); E, ethanol (λ_{max}= 676.9 nm); M, 1:1 freezing medium and glycerol (λ_{max}= 681.3 nm). Structure of APT is shown in lower portion of figure.

environments in which the APT can be found while in cells or in single component glasses the APT environment is less inhomogeneous. In previous work on NPHB of APT in glassy samples [22, 28-31], it was shown that the fluorescence maximum is solvent and pH dependent. In hyperquenched glassy water, the APT fluorescence shifts red with increasing pH. At pH = 3.4, e.g., the maximum is at 672 nm, at 668 nm for neutral pH (as shown in Fig. 2), and at 663 nm for pH 11.6. Relative to neutral hyperquenched glassy water, the fluorescence excitation maximum also shifts red in glassy ethanol (679 nm) or methanol (677 nm) [22]. A water content of ~1% has shifted the fluorescence excitation maximum given in Fig. 4-2 for ethanol to 677 nm. Along with the changes in peak position, there are also changes in the fluorescence band shape which occur in the different glassy solvents. As can be seen in Fig. 4-2, for the cellular samples and for hyperquenched glassy water, the fluorescence excitation band is very broad with a nearly flat-topped peak. In previous work [22, 30], it has been shown that there are two bands contributing to the absorption. Similar structure is also observed in ethanol and methanol where the bands are somewhat better resolved [22]. In Fig. 4-2 the spectra for ethanol and freezing media clearly show two peaks while the two bands are poorly resolved in water and the cell spectra. The nature of the second band has not been conclusively determined, although it does not seem to be a vibronic absorption band. From hole burning action spectra in glassy water, ethanol and methanol [22], it appears to be an APT configuration that rapidly converts to the lower energy absorbing band from which the fluorescence originates. This is evidenced by the broadening and lower saturated fractional hole depth of holes burned on the blue side of the absorption

relative to holes burned on the red side. In hyperquenched glassy water, the hole widths for the bluer holes indicate a ~1 ps relaxation process is involved. The red side holes, on the other hand, have widths which depend upon the annealing of the sample. In samples annealed at temperatures near the glass transition temperature, the hole widths are as narrow as 110 MHz at 5.0 K, i.e. they approach the fluorescence lifetime; in unannealed samples they are ~500 MHz [30]. In comparing the fluorescence excitation spectra of APT in cells with that in the glassy media, the peak position and band shape for APT-treated cells indicate a low pH, aqueous environment. Studies of APT as a photodynamic agent have shown that APT is present in lysosomes [36]. Lysosomes are sub-cellular structures whose function is macromolecular digestion [41]. The digestive enzymes present in lysosomes are acid hydrolases which function best in a low pH environment. That APT is localized in lysosomes is consistent with the spectral observations of Fig. 4-2. That the environment is similar to hyperquenched glassy water will be further demonstrated in what follows.

Fig. 4-3 shows typical hole spectra for APT-treated cells at 4.5 K after burning at a burn frequency, ω_B= 14,771 cm^{-1}. For the lowest burn fluence, a zero-phonon hole with a width of ~1500 MHz is observed. As shown in the figure, continued burning leads to saturation and broadening of the zero-phonon hole, growth of a phonon side band hole with a peak at $\omega_B - 31 \pm 2$ cm^{-1} and development of weak vibronic hole structure. Two conclusions regarding hole burning of APT in cells can be drawn from the data shown in Fig. 4-3. First, that hole burning of APT in cells is observed is strong evidence that the APT is in a glassy environment, as hole burning is either absent or much reduced in crystalline environments

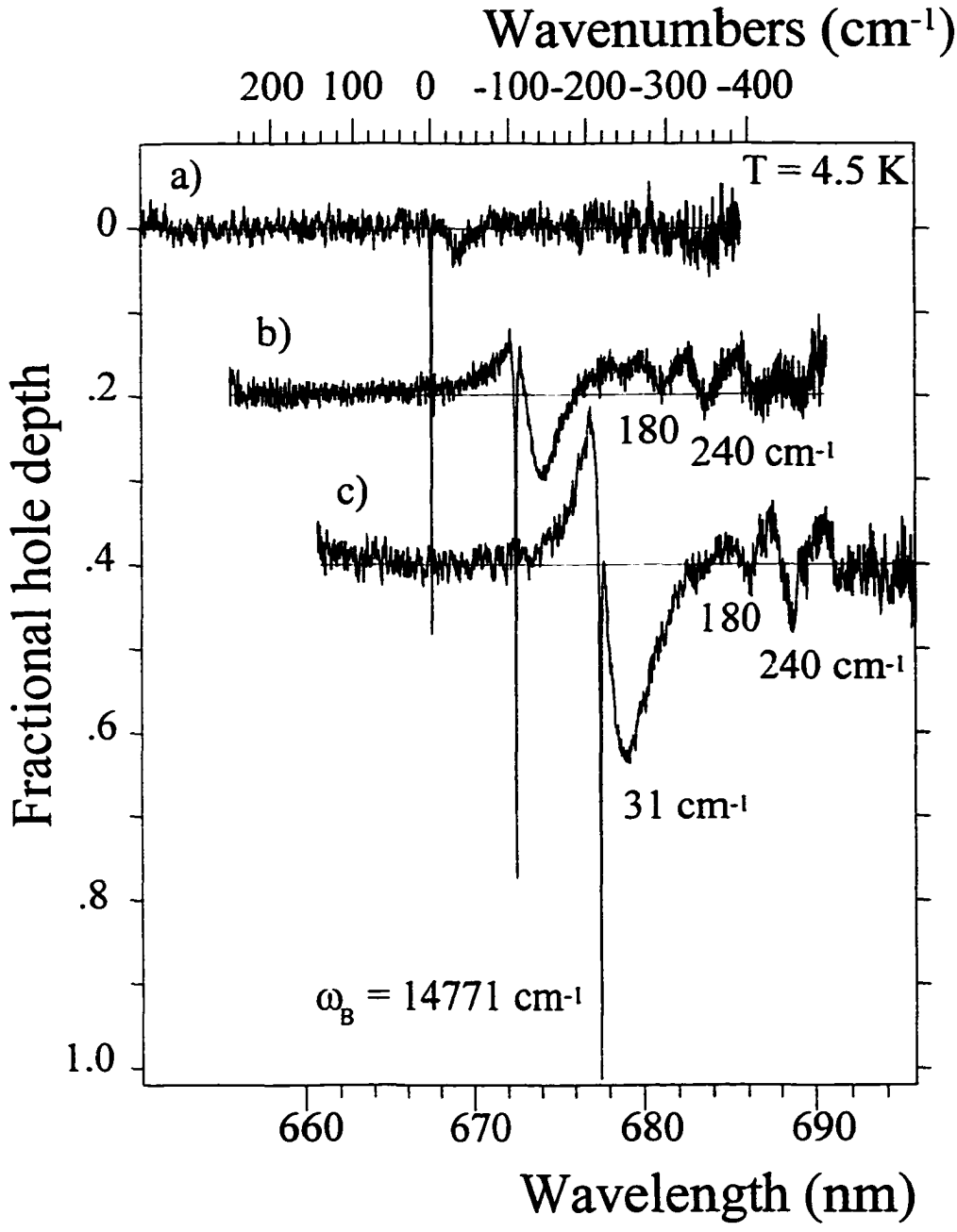

Figure 4-3. Hole profiles for holes burned at $\omega_B = 14771$ cm^{-1} with increasing fluence. Burn fluences were a) 0.086 J/cm^2, b) 0.81 J/cm^2, and c) 7.3 J/cm^2. All three spectra show a phonon side band hole having a mean phonon frequency of 31 cm^{-1}. Spectra b and c also show pseudo-vibronic holes at 180 cm^{-1} and 240 cm^{-1}. For clarity, b and c were shifted relative to a. Shifts were 5 nm, 0.2, and 10 nm, 0.4 for b and c, respectively.

[22, 30]. Second, from the spectral hole profile shown in Fig. 4-3, the hole burning most likely occurs through a non-photochemical hole burning process. NPHB is widely observed in glasses and is due to a configurational rearrangement of solvent molecules around an electronically excited probe molecule. The presence of a broad distribution of nearly isoenergetic structural configurations is a universal property of glasses which arises from their disordered nature. A characteristic of NPHB is that the "product" absorption (anti-hole) lies within the original inhomogeneously broadened absorption band and, for π-π^* transitions is blue-shifted relative to ω_B, as is shown for APT in cells in Fig. 4-3. The blue-shifted anti-hole has been explained in terms of an increase in glass free volume in the vicinity of the probe molecule [42, 43].

It is interesting to compare the hole burning results for APT in cells with the results for APT in hyperquenched glassy water, ethanol and methanol [22, 29, 30]. APT in hyperquenched glassy water is a highly efficient hole burning system with hole widths as narrow as 110 MHz when burned at 4.5 K following annealing at temperatures near the glass transition temperature. Even in unannealed films, the hole widths are typically only ~500 MHz. In ethanol and methanol hole burning at 4.5 K of films annealed at higher temperatures gave widths of 1,500 MHz and 2,000 MHz, respectively. The phonon sideband holes observed for APT in hyperquenched glassy water are peaked at 38 cm^{-1} compared with 26 cm^{-1} for ethanol and 17 cm^{-1} for methanol. The phonon frequencies for hyperquenched glassy water are considerably higher than the 20-25 cm^{-1} phonon sideband holes observed for a wide variety of other hole burning systems. Given the slow cooling to -70 °C used for the

cellular samples, it is appropriate to compare the characteristics of holes for APT in cells with the characteristics for the annealed films. For the cell samples, the zero-phonon hole widths are more similar to ethanol than to hyperquenched glassy water while the mean phonon frequency (~31 cm^{-1}) is between that for ethanol (26 cm^{-1}) and hyperquenched glassy water (38 cm^{-1}). The point is not that APT is in an alcoholic environment but rather that the disordered hydrogen bond structure, which gives hyperquenched glassy water its unique properties as a hole burning host [29], is preserved in cells although it is somewhat modified by the other cellular components. One can also compare the Huang-Rhys factors, S, for APT in the various glasses. The Huang-Rhys factor is a measure of the electron-phonon coupling strength and, at low temperatures, determines the saturated zero-phonon hole depth since at any frequency within the inhomogeneously broadened origin band, the zero-phonon contribution to absorption will be exp[-S]. From Fig. 4-3, the fractional hole depth is 0.57 which corresponds to an S of 0.56. However this value must be considered as an upper limit for S as the zero-phonon hole is not completely saturated and as there is some interference between the zero-phonon hole and the anti-hole evident in the figure. S can also be determined by extrapolating the ratio of integrated zero-phonon hole area to the total integrated hole area (zero-phonon hole + phonon side band hole) to zero fluence. This ratio is given by exp[-2S] [2; 44]. Using this method, S= 0.34 was determined for APT in cells. S was also determined from the kinetic fits discussed later, where S= 0.36 was determined. Given that zero-phonon hole depth is measured directly from the kinetics curves, 0.36 can be considered the most accurate value for S. Although there is some disparity between the

various determinations of S, the values are all less than 1.0 indicating that the electron-phonon coupling may be characterized as weak. For APT in annealed hyperquenched glassy water, ethanol and methanol, S values of 0.55, 0.43 and 0.36 were determined [22, 28]. Thus, the value in cells is similar to that observed in the other three systems.

The efficiency of hole burning for APT in hyperquenched glassy water can be judged by the fluence required to burn a 10% hole at 5K, 0.13 $\mu J\ cm^{-2}$. For APT in MCF-10F cells a fluence of 6.0 $\mu J\ cm^{-2}$ is needed to burn a 10% hole at ω_B = 680.9 nm. Thus, although APT-treated cells show fluorescence excitation spectra similar to those observed for APT in hyperquenched glassy water, there are significant differences between the hole burning properties of the two systems. APT in hyperquenched glassy water is more efficient, with narrower zero-phonon holes and a higher frequency phonon side band hole. These results would indicate that there must be a difference between the environment of APT in hyperquenched glassy water and in lysosomes.

The kinetics of hole burning for APT in cells and in hyperquenched glassy water is also quite different as shown in Fig. 4-4. This figure shows, on a logarithmic time scale, the time development of holes in the two systems. For both, the non-exponential hole burning is evidence that the kinetics cannot be described by a single rate. Treating the kinetics as being described by a Gaussian distribution of rates has been successful for a variety of glassy samples [45, 46]. In this treatment, the time dependent fractional hole depth , D(t), is given as

$$D(t) = (2\pi)^{-1/2} \int_{-\infty}^{+\infty} dx \exp(-x^2/2) \exp(-\Sigma_o \xi(x) t) \qquad (1)$$

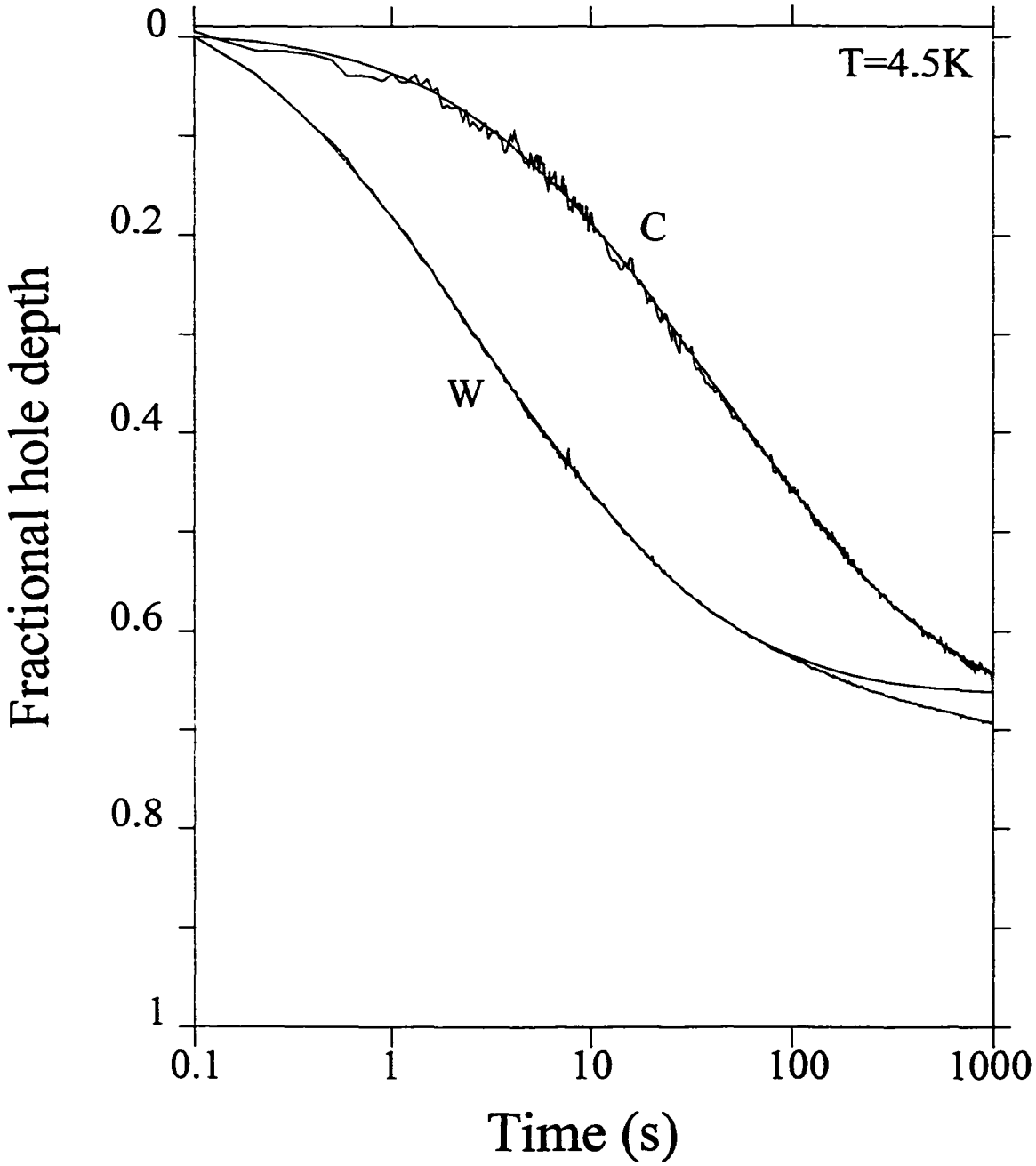

Figure 4-4. Hole growth curves and theoretical fits to eq. 1 correspond to APT in hyperquenched glassy water (W) and in MCF-10F cells (C). Fit parameters were W: λ_0= 8.2, σ_λ= 0.99, S=0.40; C: λ_0= 9.1, σ_λ= 0.96, S=0.36. Both curves were for burns using an intensity of 1.7 $\mu W/cm^2$.

where $\Sigma_0 = P\sigma\Omega_0\tau$ with P the burn photon flux; σ the peak absorption cross section; and τ the excited state lifetime; Ω_0 describes the average harmonic frequency of the extrinsic two level systems, TLS_{ext}, the glass configurations described by an intermolecular double well potential which are formed by interaction of the probe molecule with the glass. The integration variable $x = (\lambda - \lambda_0)/\sigma_\lambda$ and $\xi(x) = \exp[-2(\lambda_0-\sigma_\lambda x)]$. λ is the tunneling parameter for TLS_{ext}. Eq. 1 is derived by assuming that λ has a Gaussian distribution centered at λ_0 with a standard deviation σ_λ and that tunneling is the rate determining step in the hole burning process. Eq. 1 describes the time dependence only of the zero-phonon hole, but it does not take into account the change in hole shape (broadening). As the zero-phonon hole saturates, i.e., as the subpopulation of molecules in exact resonance with the burn frequency is depleted, non-resonant absorption through the wings of Lorentzian zero-phonon lines become important. Because of non-resonant absorption and the burning of molecules absorbing through phonon processes, the hole continues to grow. This is the cause of the deviation of the APT in hyperquenched glassy water data at long times in Fig. 4-4. The data in Fig. 4-4 was fit to Eq. 1 using a four parameter least squares fit. The four fit parameters, λ_0, σ_λ, the Huang-Rhys factor, S, and the amplitude at t=0 (a technical parameter), were used to obtain the fits in Fig. 4-4; values for λ_0, σ_λ, and S are given in the figure caption. The values for the two systems are quite similar, although λ_0 is slightly higher for cells than for hyperquenched glassy water. The more rapid hole burning of APT in hyperquenched glassy water is caused entirely by the homogeneous width being a factor of three narrower than for APT in cells.

A further difference between APT in cells and in hyperquenched glassy water is indicated in Fig. 4-5. This shows the effect of burning consecutive holes at 1 nm spectral intervals throughout the APT absorption. As is evident in the figure, when these holes are burned beginning at high energies, and each subsequent hole displaced by 1 nm to lower energy, (i.e., blue to red), a hole action spectrum results. Note that this acton spectrum shows that holes are only burned into the low energy half of the band. As discussed above, attempts to burn holes in the higher energy band are unsuccessful due to rapid relaxation to the lower energy band. On the other hand, if the burning is initiated at low energies and subsequent holes are burned to higher energy, (i.e., red to blue), hardly any holes result. For APT in hyperquenched glassy water, there is also a dependence on whether the burn proceeds from high to low energy or *vice versa*, although the result is not as dramatic: there is a diminution of hole depths when burning is from high to low energy as opposed to the nearly complete absence of holes seen for APT treated cells. Thus, laser induced hole filling is more efficient for APT in cellular samples than for APT in hyperquenched glassy water. Laser induced hole filling has previously been discussed [47, 48]. The filling was found to be substantially higher when the secondary burn frequency, ω_{B2}, was to higher energy of the initial burn frequency, ω_{B}., Based on detailed observations of the total spectral changes involved in burning and laser induced filling, the increased filling efficiency for blue secondary burns was related to the blue-shifted anti-holes observed in NPHB [48]. Thus, hole filling is due to light-induced anti-hole reversion. The present observations on laser-induced hole filling of APT in cells are entirely consistent with this filling mechanism. However, a second

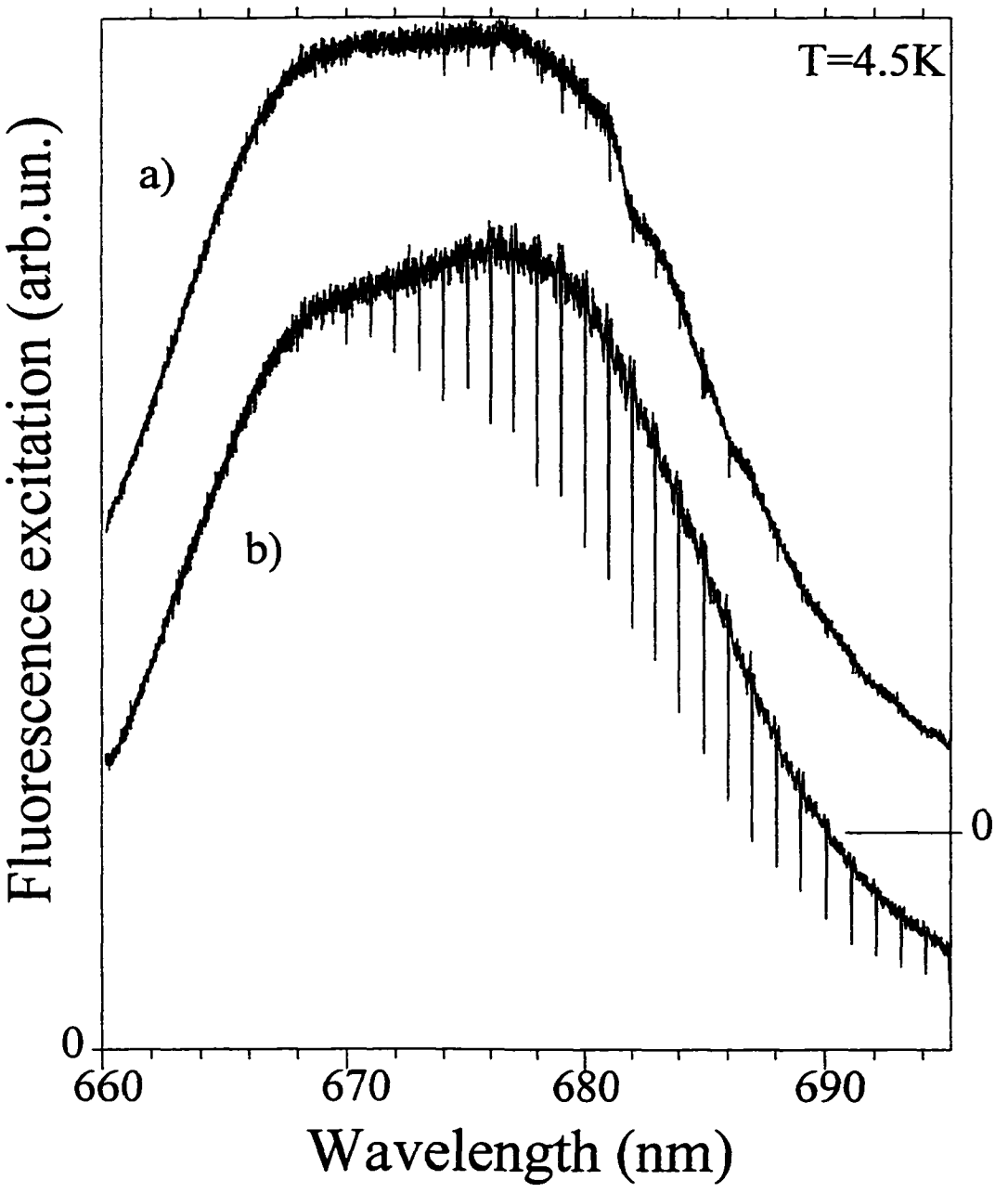

Figure 4-5. Action spectra of holes burned across the fluorescence excitation profile of APT in MCF-10F cells showing the dependence of hole profile on the burn direction. a) and b) result from burning holes in the red to blue and blue to red directions, respectively. Each hole was burned using a burn fluence of 133 mJ/cm^2.

mechanism involving ~1 ps relaxation from blue absorbing APT conformers into red absorbing conformers cannot be ruled out.

A change in the hydrostatic pressure applied to the sample after hole burning effects both the frequency and width of the hole. The frequency shift is linear if the sample is elastic, and is understood to be due to a change in the average equilibrium separation between the solute and the solvent, r_0. Therefore, the direction of the frequency shift depends upon both the magnitude and the sign of the pressure change. The frequency shift has been shown to be related to the effect of solvating the probe molecule, i.e., the gas to solvent shift, ($\bar{\nu}_B$ - $\bar{\nu}_{vac}$) and the matrix compressibility, κ [49]:

$$\Delta\bar{\nu}(\bar{\nu}_B, \Delta P) = 2\kappa\Delta P(\bar{\nu}_B - \bar{\nu}_{vac}) \qquad (2)$$

Several inferences can be drawn from this expression. First, if $\bar{\nu}_{vac}$ lies within the inhomogeneously broadened absorption band, burning at $\bar{\nu}_{vac}$ will be independent of pressure. Second, the pressure shift is wavelength dependent, increasing as the burn frequency is further removed from $\bar{\nu}_{vac}$. Finally, from the variation of $\Delta\bar{\nu}(\bar{\nu}_B, \Delta P)$ with $\bar{\nu}_B$, one can determine both $\bar{\nu}_{vac}$ and κ, the compressibility of the sample. The variation of the pressure induced frequency shift with pressure is shown in Fig. 4-6. As is evident from the figure, the pressure shift is linear at all burn wavelengths. Therefore, the pressure effects are elastic although some hole filling does occur so that the hole shape is not entirely recovered when the pressure is removed. A plot of the slopes of the pressure shifts *vs.* burn frequency can be extrapolated to yield the vacuum absorption frequency of APT. A value of 15627 cm^{-1} (639.9 nm) was determined. Although this value is consistent with the values determined

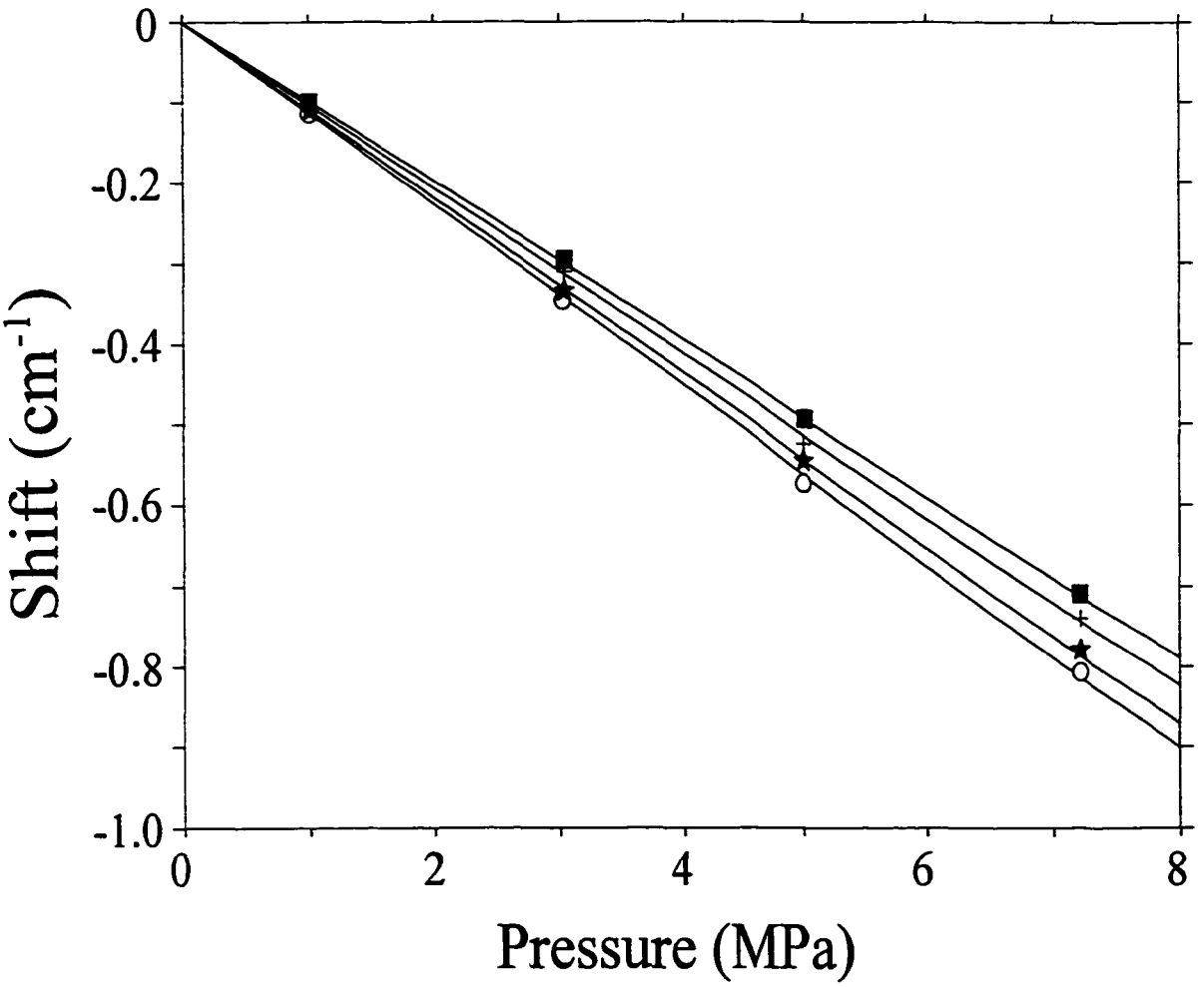

Figure 4-6. Shift of the center frequency for holes burned at 677.5 nm (square), 680.0 nm (cross), 682.0 nm (star), and 685.0 nm (circle) as a function of hydrostatic pressure.

for similar molecules in a supersonic jet expansion, given the range over which the extrapolation is made, the result is probably accurate to only ~20%. The compressibility determined from Eq. 1 is 0.06 GPa^{-1}, which is comparable with the values obtained in a similar manner for organic glasses, polymers and protein samples [10-17]. The question arises as to what the measured compressibility corresponds. For similar measurements on probe molecules within proteins [14], the authors argued that the compressibility is of the protein due to the short range nature (R^{-6}) of the interactions causing the pressure shift. If the compressibility being measured is the local compressibility, then the value determined is probably that of the lysosomes in which the dye is located. Experiments in which the lysosomes are disrupted by photoactivation before freezing are planned. It will be of interest whether there is any significant difference in compressibility for such samples. Hole burning experiments on a second cell line are also in progress. The cells in these experiments use MCF-7 human breast adenocarcinoma cells. Although the results are still preliminary, there appears to be less reproducibility in these cells, perhaps reflecting the heterogeneity of this cancer cell line [50].

The Ames Laboratory is operated for the US-DOE by Iowa State University under Contract W-7405-Eng-82, and this work was supported by the Office of Health and Environmental Research, Office of Energy Research. T. Reinot was supported by the Solid State Chemistry and Polymers Program of the Division of Materials Science Division of NSF. The authors would like to thank Kristi Harkins, Paul Kapke, and Donghui Cheng at the ISU Cell and Hybridoma Facility for assistance with cell culture and flow cytometry.

References

1. Jankowiak, R.; Small, G. J. *Chem. Res., Toxicol.* **1991,** *4*, 256.

2. Jankowiak, R.; Small, G. J. In *The Photosynthetic Reaction Center*; J. Diesenhofer and J. Norris, Editors. Academic, New York, **1993**; p 133.

3. Jankowiak, R.; Cooper, R. S.; Zamzow, D.; Small, G. J.; Doskocil, G.; Jefferey, A. M. *Chem. Res. Toxicol.* **1988**, *1*, 60.

4. Ariese, F.; Small, G. J.; Jankowiak, R. *Carcinogenesis*. **1996**, *17*, 829.

5. Kaposi, A. D.; Fidy, J.; Stavrov, S. S.; Vanderkooi, J. M. *J. Phys. Chem.* **1993**, *97*, 6319.

6. Reddy, N. R. S.; Lyle, P. A.; Small, G. J. *Photosyn. Res.* **1992**, *31*, 167.

7. Small, G. J. *Chem. Phys.* **1995**, *197*, 239.

8. Kador, L.; Haarer, D.; Personov, R. *J. Chem. Phys.* **1987**, *86*, 5300.

9. Meixner, A. J.; Renn, A.; Bucher, S. E.; Wild, U. P. *J. Phys. Chem.* **1986**, *90*, 6777.

10. Chang, H.-C.; Jankowiak, R.; Reddy, N. R. S.; Small, G. J. *Chem. Phys.* **1995**, *197*, 307.

11. Gafert, J.; Friedrich, J.; Parak, F. *J. Chem. Phys.* **1993**, *99*, 2478.

12. Gradl, G.; Zollfrank, J.; Breinl, W.; Friedrich, J. *J. Chem. Phys.* **1991**, *94*, 7619.

13. Reddy, N. R. S.; Jankowiak, R.; Small, G. J. *J. Phys. Chem.* **1995**, *99*, 16168.

14. Schellenberg, P.; Friedrich, J.; Kikas, J. *J. Chem. Phys.* **1994**, *100*, 5501.

15. Sesselman, Th.; Richter, W.; Haarer, D.; Morawitz, H. *Phys. Rev. B.* **1987**, *36*, 7601.

16. Wu. H.-M.; Savikhin, S.; Reddy, N. R. S.; Jankowiak, R.; Cogdell, R. J.; Struve, W. S.; Small, G. J. *J. Phys. Chem.* **1996**, *100*, 12022.

17. Zollfrank, J.; Friedrich, J.; Fidy, J.; Vanderkooi, J. M.. *J. Chem. Phys.* **1991**, *94*, 8600.

18. Jankowiak, R.; Hayes, J. M.; Small, G. J. *Chem. Rev.* **1993**, *93*, 1471.

19. Hayes, J. M.; Jankowiak, R.; Small, G. J. In *Topics in Current Physics, Persistent Spectral Hole Burning: Science and Applications*; Moerner, W. E., Ed. Springer-Verlag: New York, **1987**; p 153.

20. Jankowiak, R.; Small, G. J. *Science* **1987**, *237*, 618.

21. Moerner, W. E., Ed. *Topics in Current Physics, Persistent Spectral Hole Burning: Science and Applications*; Springer-Verlag: New York, **1987**.

22. Reinot, T.; Kim, W.-H.; Hayes, J. M.; Small, G. J. *J. Chem. Phys.* **1996**, *104*, 793.

23. Milanovich, N.; Suh, M.; Jankowiak, R.; Small, G. J.; Hayes, J. M. *J. Phys. Chem.* **1996**, *100*, 9181.

24. Benson, R. C.; Meyer, R. A.; Zaruba, M. E.; McKhann, G. M. *J. Histochem. Cytochem.* **1979**, *27*, 44.

25. Aubin, J. E. *J. Histochem. Cytochem.* **1979**, *27*, 36.

26. Henderson, B. W.; Dougherty, T. J. *Photochem. Photobiol.* **1992**, *55*, 145.

27. Boyle, R. W.; Dolphin, D. *Photochem. Photobiol.* **1996**, *64*, 469.

28. Reinot, T.; Hayes, J. M.; Small, G. J. *J. Chem. Phys.* **1997a**, *106*, 457.

29. Reinot, T.; Kim, W.-H.; Hayes, J. M.; Small, G. J. *J. Opt. Soc. Am. B.* **1997b**, *14*, 602.

30. Kim, W.-H.; Reinot, T.; Hayes, J. M.; Small, G. J. *J. Phys. Chem.* **1995**, *99*, 7300.

31. Kim, W.-H.; Reinot, T.; Hayes, J. M.; Small, G. J. *J. Chem. Phys.* **1996**, *104*, 6415.

32. Rosenthal, I. *Photochem. Photobiol.* **1991**, *53*, 859.

33. Spikes, J. D. *Photochem. Photobiol.* **1986**, *43*, 691.

34. Moan, J.; Berg, K.; Anholt, H.; Madslien, K. *Int. J. Cancer*. **1994**, *58*, 865.

35. Ben-Hur, E.; Siwecki, J. A.; Newman, H. C.; Crane, S. W.; Rosenthal, I. *Cancer Lett.* **1987**, *38*, 215.

36. Peng, Q.; Farrants, G. W.; Madslien, K.; Bommer, J. C.; Moan, J.; Danielsen, H. E.; Nesland, J. M. *Int. J. Cancer*. **1991**, *49*, 290.

37. Soule, H. D.; Maloney, T. M.; Wolman, S. R.; Peterson, Jr., W. D.; Brenz, R.; McGrath, C. M.; Russo, J.; Pauley, R. J.; Jones, R. F.; Brooks, S. C. *Cancer Res.* **1990**, *50*, 6075.

38. Tait, L.; Soule, H. D.; Russo, J. *Cancer Res.* **1990**, *50*, 6087.

39. Farrant, J.; Walter, C. A.; Lee, H.; Morris, G. J.; Clarke, K. J. *J. Microsc.* **1977**, *111*, 17.

40. Franks, F. *J. Microsc.* **1977**, *111*, 3.

41. Alberts, B.; Bray, D.; Lewis, J.; Raff, M.; Roberts, K.; Watson, J. D. *Molecular Biology of the Cell*, 3rd ed.; Garland Publishing: New York, **1994**; p 610.

42. Shu, L.; Small, G. J. *Chem. Phys.* **1990**, *141*, 447.

43. Shu, L.; Small, G. J. *J. Opt. Soc. Am. B.* **1992a**, *9*, 724.

44. Hayes, J. M.; Gillie, J. K.; Tang, D.; Small, G. J. *Biochim. Biophys. Acta.* **1988**, *932*, 287.

45. Kenney, M.; Jankowiak, R.; Small, G. J. *Chem. Phys.* **1990**, *146*, 47.

46. Shu, L.; Small, G. J. *J. Opt. Soc. Am. B.* **1992b**, *9*, 733.

47. Fearey, B. L.; Carter, T. P.; Small, G. J. *Chem. Phys.* **1986**, *101*, 279.

48. Shu, L.; Small, G. J. *J. Opt. Soc. Am. B.* **1992c**, *9*, 738.

49. Laird, B. B.; Skinner, J. L. *J. Chem. Phys.* **1989**, *90*, 3274.

50. Resnicoff, M.; Medrano, E. E.; Podhajcer, O. L.; Bravo, A. I.; Bover, L.; Mordoh, J. *Proc. Natl. Acad. Sci. USA.* **1987**, *84*, 7295.

CHAPTER 5. STARK HOLE-BURNING OF ALUMINUM PHTHALOCYANINE TETRASULFONATE IN NORMAL AND CANCER CELLS

A paper published in *J. Phys. Chem. B*, **1998**, *102*, 4265

N. Milanovich, M. Rätsep, T. Reinot, J. M. Hayes, G. J. Small

5.1. Abstract

The results of Stark hole-burning of aluminum phthalocyanine tetrasulfonate (APT) in MCF-10F (normal) and MCF-7 (cancer) cells are reported. Hole broadening was observed for zero-phonon holes (ZPH) for both cell lines when laser polarization was parallel and perpendicular to an applied electric (Stark) field. Changes in dipole moment suggest that dye molecules are located near the cell membrane and, in normal cells, experience some degree of ordering not found in the cancer cells.

5.2. Introduction

In a recent paper [1] (referred to hereafter as I) we demonstrated that nonphotochemical hole burning (NPHB) spectroscopy can be applied to dye molecules within cells. Our ultimate objective is to determine whether NPHB can be used to "image" anomalies in sub-cellular structures as a normal cell transforms into a cancer (diseased) cell. By analogy with magnetic resonance imaging (MRI), one can refer to our concept as hole burning imaging (HBI). With NPHB, however, several properties can be measured including the homogeneous width of the zero-phonon hole (ZPH), the electron-phonon coupling and the response of the ZPH to pressure and external electric (Stark) fields. Earlier work on

NPHB of dye molecules in polymers and glasses had shown that NPHB is sensitive to the microenvironment around the dye [2].

In I, the dye molecule aluminum phthalocyanine tetrasulfonate (APT) in (normal) MCF-10F, human breast epithelial cells was studied *in vitro*. APT was chosen as the test molecule because it is membrane permeable (having been used in photodynamic cancer therapy) and because its NPHB properties in hyperquenched and annealed glassy films of water [3-5], ethanol and methanol [6] have been thoroughly studied. In I, results on the homogeneous width, electron-phonon coupling, dispersive hole growth kinetics and pressure-induced linear shifting of APT's ZPH in normal cells were reported. It was concluded that APT in the cell is in an aqueous environment, one that is glassy rather than crystalline at low temperatures. However, it appears that the hydrogen-bonding of water molecules with APT in pure glassy water is somewhat disrupted in the cell due to APT's interactions with other cellular components. Although APT's hole burning efficiency in the cell is lower (7x) than in glassy water, it is still high (a burn fluence of 6.0 mJ/cm^2 produces a fractional hole depth of 0.1). Subsequently, we performed the same experiments for APT in MCF-7 human breast adenocarcinoma cells (unpublished results). Briefly, no significant reproducible differences were observed. While the results for MCF-10F cells from different samples were highly reproduceable, those for MCF-7 cells were less so, perhaps reflecting the heterogeneity of this cell line [7].

The inability of APT to distinguish between normal and cancer cells based on the above types of experiments is probably mainly due to the fact that APT is not organelle-

specific, *vide infra*. Ideally, one would like to use a probe molecule that is specific to a cellular component known to undergo significant structural changes as a normal cell evolves into a cancerous cell. Nevertheless, we present hole burning data which show that, with the Stark effect (external electric field), APT can distinguish between the two cell lines.

5.3. Experimental Section

MCF-10F and MCF-7 cells were obtained from the American Type Culture Collection (ATCC). MCF-10F cells were cultured in a 1:1 mixture of Ham's F12 medium and Dulbecco's modified Eagle's medium containing 5% horse serum, 100 ng/ml cholera enterotoxin, 10 mg/ml insulin, 0.5 mg/ml hydrocortisol, and 20 ng/ml EGF. MCF-7 cells were cultured in minimum essential medium (Eagle) with non-essential amino acids, Earle's BSS, 1 mM sodium pyruvate, 10 mg/ml bovine insulin, with 10% fetal bovine serum. All culture media components were purchased from Sigma-Aldrich Chemicals. Both cell lines were incubated at 37 °C under an air atmosphere containing 5% CO_2; cells were passed weekly. Staining of MCF-10F and MCF-7 cells were carried out as described previously for MCF-10F cells. MCF-7 cells were suspended in a freezing medium different from MCF-10F. The MCF-7 freezing media consisted of MCF-7 culture media with 5% DMSO. The reader is referred to I for a detailed discussion of overall protocol. Sample aliquots, in their respective freezing media, were diluted 1:1 (by volume) with glycerol and transferred to 5 mm o.d. gelatin capsules for facile formation of a glass at 4.5 K. The hole burning apparatus which utilizes the fluorescence excitation mode for recording of absorption and hole burned spectra is described in I. Linewidth of the laser used for burning and recording of hole

burned spectra was < 20 MHz.

The Stark cell used for this experiment consisted of two teflon walls separated by a distance of 11 mm and two copper electrodes positioned perpendicular to the walls. A separation of 4.95 mm was maintained between the electrodes by placing them into grooves made on the inside of the teflon walls. The experiments were done using a fluorescence excitation scheme described previously [1, 3] and, therefore, the electrodes had to be placed above and below the sample to avoid repositioning of the sample during the experiment. The laser beam was able to access the samples through a slit on one of the teflon walls. Samples were placed lying on their sides at ~45 degrees relative to the teflon walls and immediately plunged into a cryostat pre-cooled to 4.2 K; subsequent cooling to 1.8 K was done by applying a vacuum to the cryostat's sample chamber. A polarizer placed in front of the Stark cell was used to orient the laser beam polarization either parallel or perpendicular to the applied Stark field. Electric field strengths up to 10.1 kV/cm were utilized.

5.4. Results and Discussion

Fluorescence excitation spectra for APT-stained MCF-10F and MCF-7 cells at 1.8 K are given in Figure 5-1. Both spectra have nearly flat-topped peaks and are composed of two separate bands which are slightly resolved for the MCF-10F sample; the identities of these two bands have been discussed elsewhere [1, 3-6]. Fluorescence excitation maxima of 675.4 nm and 676.2 nm correspond to the lower energy bands of MCF-10F and MCF-7, respectively, and were determined by fitting two gaussian lineshapes to each spectrum. In I, APT was shown to have considerable broadening of the fluorescence excitation band and a

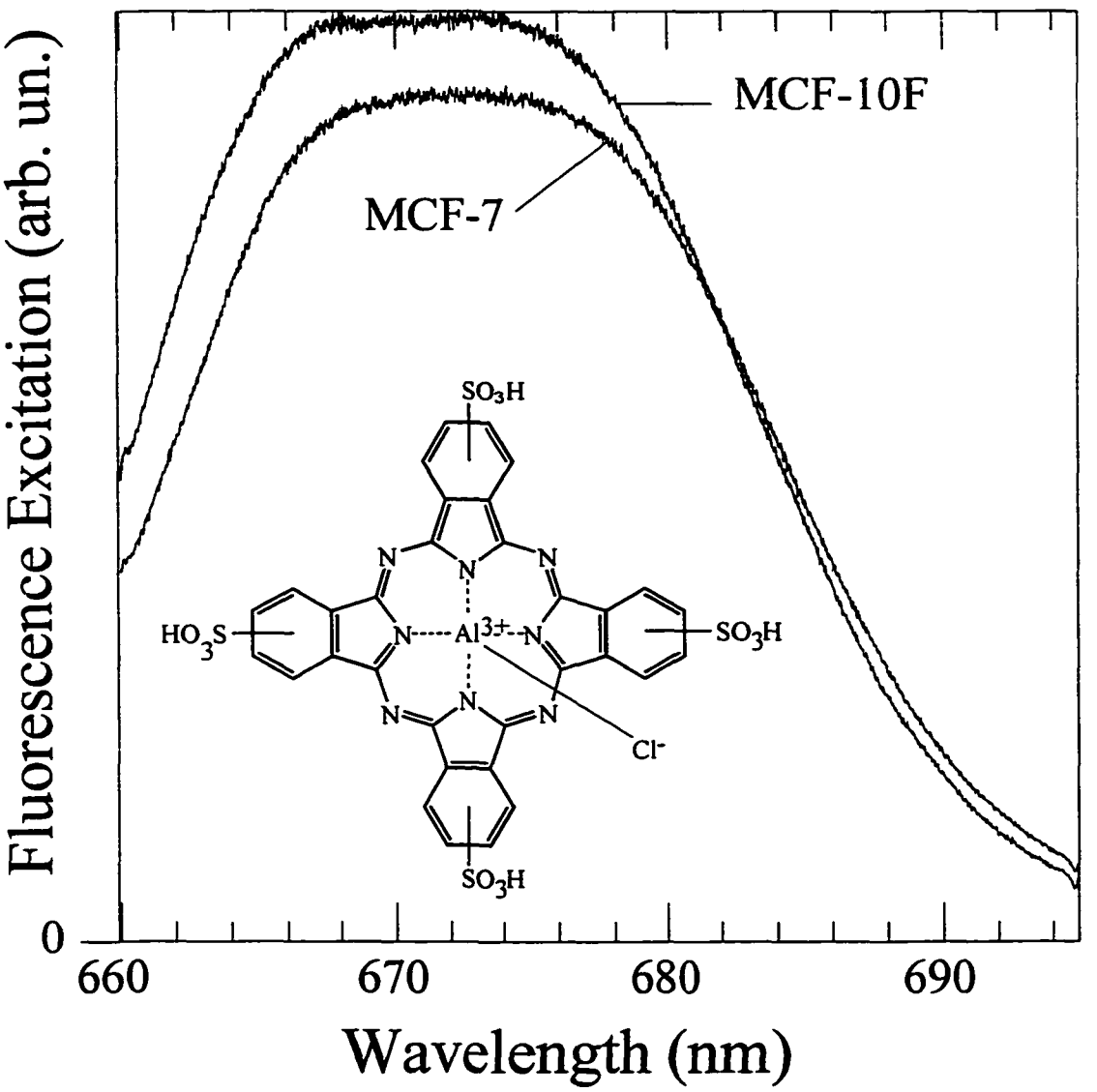

Figure 5-1. Fluorescence excitation spectra of APT in MCF-10F cells (λ_{max} = 675.4 nm) and MCF-7 cells (λ_{max} = 676.2 nm) at 1.8 K.

large red shift in the band maximum (681.3 nm) in 1:1 MCF-10F freezing media/glycerol relative to APT in cells. A similar result was obtained for APT in 1:1 MCF-7 freezing media/glycerol (spectrum not shown) relative to MCF-7 cells stained with APT, thus verifying the presence of APT inside MCF-7 cells. The width of the bands for the two freezing media suggest that APT can be found in a variety of different environments within the freezing media while APT in the cell samples is in a less disordered environment.

The effects of a 10.1 kV/cm Stark field on the ZPH of APT in MCF-10F and MCF-7 cells are shown in Figure 5-2 for both parallel (spectra a and c) and perpendicular (spectra b and d) orientations of the burn laser polarization relative to the Stark field. For both cell lines, only Stark broadening was observed for parallel and perpendicular orientations. Broadening effects were found to be reversible when the electric field was turned off, thus returning the holes to their original widths while hole depths decreased slightly due to spontaneous hole filling (spectra not shown) [8]. No Stark splitting was observed for MCF-10F or MCF-7 cells for either polarization. Broadening of the ZPH for MCF-7 cells (Figure 5-2c and d) is comparable for both laser orientations, whereas the hole broadening for MCF-10F cells (Figure 5-2a and -2b) is greater for the parallel orientation than for the perpendicular.

A more quantitative comparison of the hole broadening for the four cases given in Fig. 5-2 can be made by calculating the change in dipole moment, $\Delta\mu$, for each case as described by Kador et al [9]. This calculation gives the result for $f{\cdot}\Delta\mu$, where f is the local field correction which is unknown for the APT matrix. Results for these calculations are

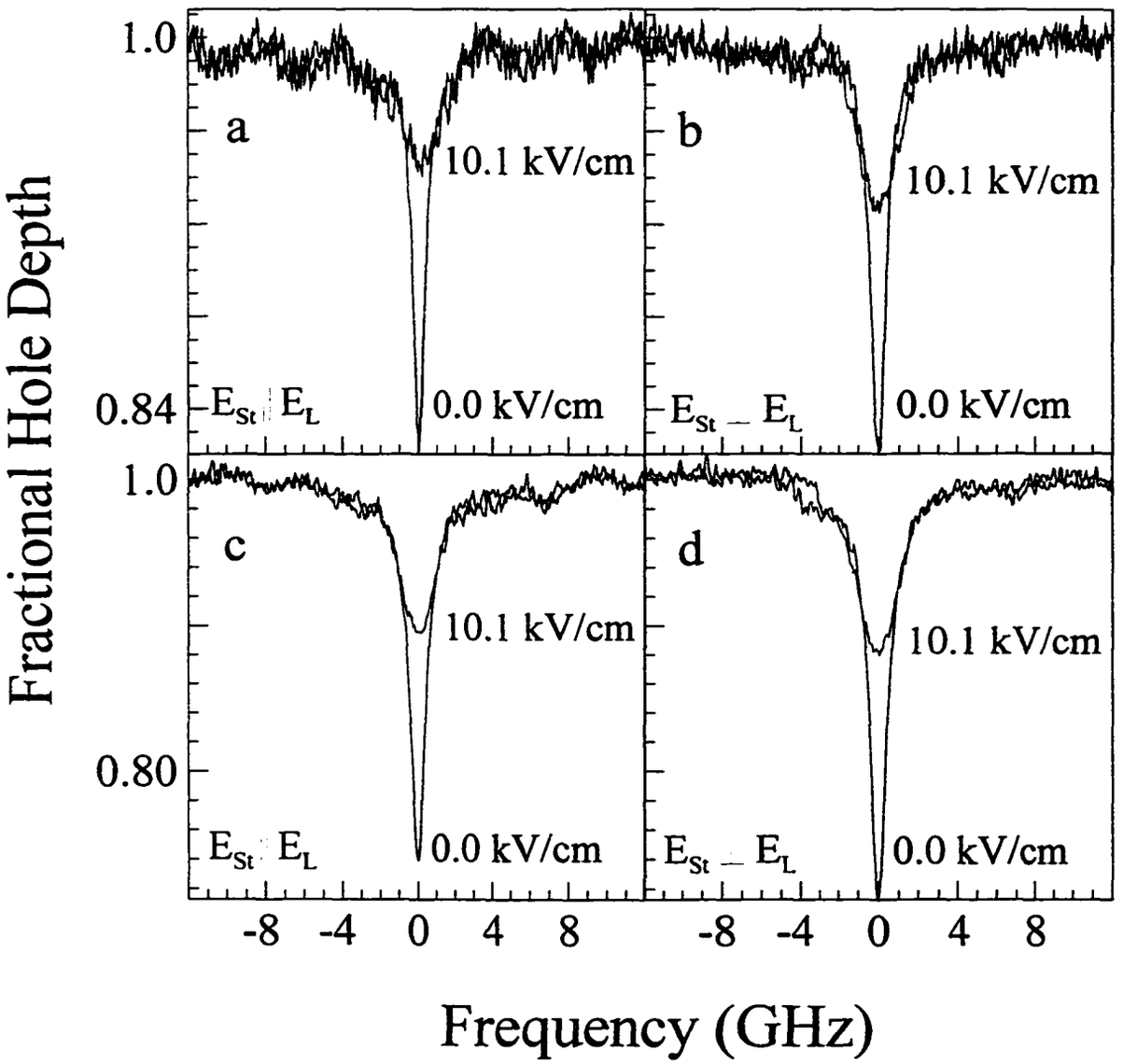

Figure 5-2. ZPH's at zero-field and with a 10.1 kV/cm external field for APT in MCF-10F cells (panels a and b) and in MCF-7 cells (panels c and d). Panels a and c correspond to burn laser polarizations parallel to the Stark field and panels b and d represent a laser polarization perpendicular to the Stark field.

given in Table 1 and were determined by fitting a plot of hole width as a function of electric field strength. An example of this is given in Figure 5-3 for MCF-10F and MCF-7 cells for the parallel orientation. From the data in Table 1, one can see that, indeed, a difference in $\Delta\mu$ exists between parallel and perpendicular polarization for MCF-10F cells. What is also interesting is that $\Delta\mu$-values for the perpendicular orientation for the two cell lines are nearly the same whereas in the parallel case these values are different. Furthermore, the $\Delta\mu$-values are for holes burned at either 677.5 nm or 678.0 nm, but $\Delta\mu$-values for holes burned near 684 nm are nearly identical to those in Table 1 for a given cell line at a given laser orientation.

Table 1: Electric Field-Induced Dipole Moment Changes for APT in MCF-10F and MCF-7 Cells.

Cell Line	$f \cdot \Delta\mu$ (D)*	Laser Polarization	λ_B (nm)
MCF-10F	0.27	$\parallel$	677.5
	0.22	$\perp$	678.0
MCF-7	0.20	$\parallel$	678.0
	0.21	$\perp$	677.5

* Uncertainty is ± 0.01 D.

Therefore, the changes in dipole moment are independent of burn wavelength.

In order to understand these results, we must consider that the change in dipole moment, $\Delta\mu$, is equal to the sum of the molecular dipole moment difference, $\Delta\mu_o$, and a matrix-induced component, $\Delta\mu_{ind}$. For the case where $\Delta\mu_o >> \Delta\mu_{ind}$, one would expect to

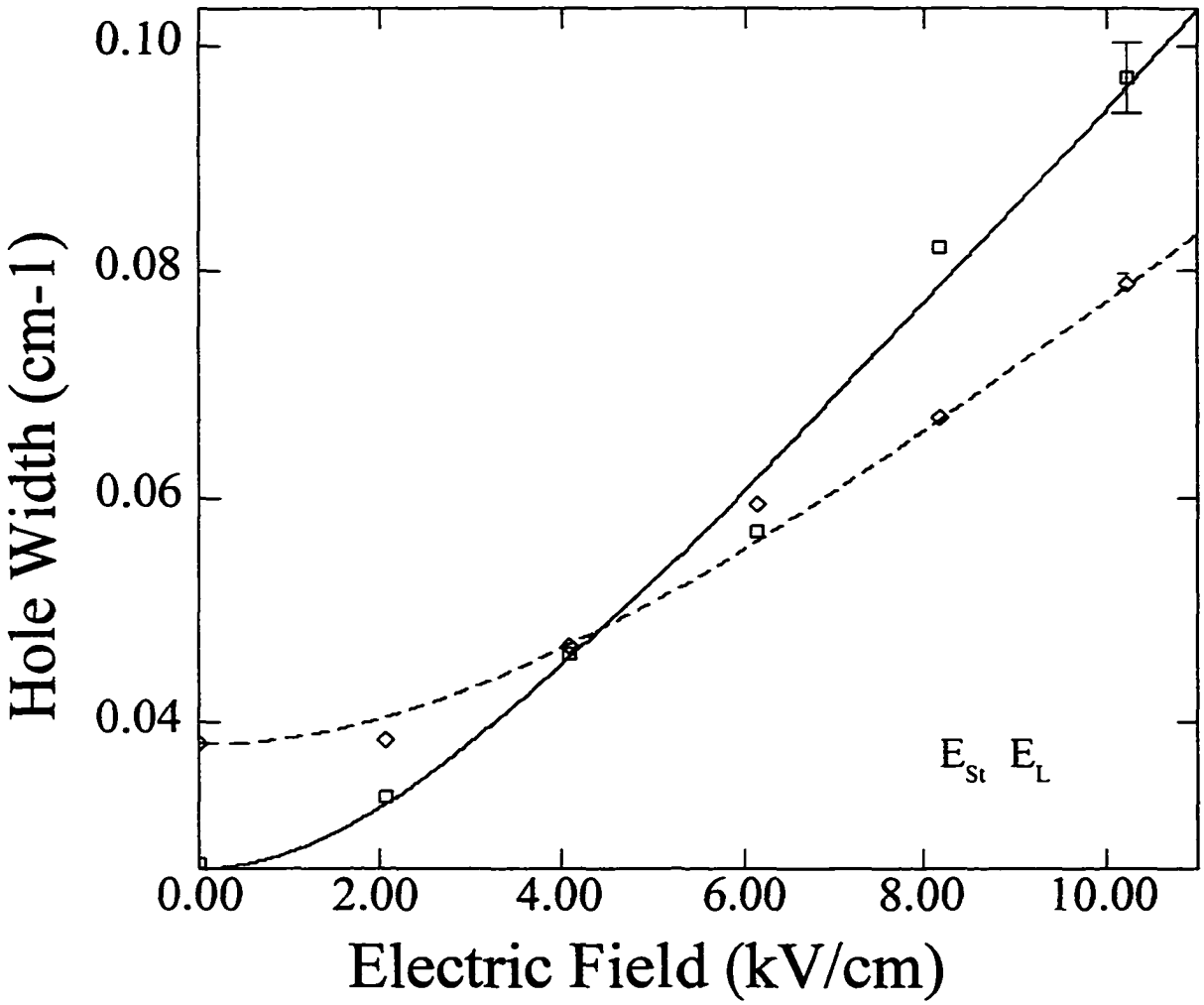

Figure 5-3. Dependence of hole width on Stark field for APT in MCF-10F cells (squares) and MCF-7 cells (diamonds) for a burn laser polarization parallel to the Stark field. Holes were burned at 677.5 nm and 678.0 nm for MCF-10F and MCF-7 cells, respectively, using a burn fluence of 139 $\mu J/cm^2$ for both. Theoretical fits are also given for MCF-10F cells (solid line) and MCF-7 cells (dashed line). Error bars are included at maximum Stark field which resulted in the largest hole width error.

observe Stark splitting for one laser orientation and Stark broadening for the other orientation [10]. However, when Stark broadening occurs at both polarizations, where $\Delta\mu_{||} \cong \Delta\mu_{\perp}$, $\Delta\mu_{ind}$ will dominate, thus indicating $\Delta\mu_{ind}$ is randomly oriented with respect to the transition dipole of APT and the laser polarization. This appears to be the case for APT in MCF-7 cells, but not for MCF-10F cells. MCF-10F data show that holes broaden in an electric field (Fig. 5-2) for both polarizations, but result in $\Delta\mu_{||} \neq \Delta\mu_{\perp}$. For MCF-10F cells, $\Delta\mu_{\perp}$ is similar to the $\Delta\mu$-values for MCF-7 and, thus, we can conclude that $\Delta\mu_{\perp}$ for MCF-10F cells is also caused by a similar randomly distributed $\Delta\mu_{ind}$. However, the fact that $\Delta\mu_{||} > \Delta\mu_{\perp}$ suggests that $\Delta\mu_{ind}$ in normal cells is not completely random. According to Vauthey et al. [11] we can consider $\Delta\mu_{ind}$ to be the sum of a random component, $\Delta\mu_{ind}$ (random), and a non-random component, $\Delta\mu_{ind}$ (non-random). This implies that some degree of ordering of APT molecules exists within the normal cells that does not exist within the cancer cells.

We are currently uncertain what causes this ordering of APT, but, we propose that the ordering of dye molecules is caused by the presence of APT at the cell membrane. Various photodynamic therapy studies have set out to determine the intracellular location of APT, resulting in conflicting data suggesting that APT can be found within lysosomes [12], mitochondria [13], or near the cell membrane [14]. From the results in I, we have established that APT has a mainly aqueous local environment with a modified hydrogen-bonding network similar to that of glassy water. Moreover, since intracellular water is associated with the hydrophilic portion of lipid bilayer membranes [15], e.g. the cell membrane, one can infer that perhaps APT molecules can be found within the aqueous region near the membrane

lipids. A modification in the hydrogen-bonding network would arise from the presence of hydroxyl groups associated with the hydrophilic portion of membrane lipids, which are usually phospholipids or glycolipids [16, 17]. This would also be consistent with our results in I where APT in cells has a fluorescence excitation maximum and mean-phonon frequency intermediate to that of glassy water and glassy ethanol. However, from the above argument alone we cannot say whether or not APT is associated with lysosomes or the cell membrane because both are composed of membrane lipids [16,17]. Müller et al. [14] have reported that photosensitization of APT in urinary bladder carcinoma cells resulted in blistering and rupture of cell membranes. The authors go on to conclude that APT is mainly associated with the cell membrane rather than with lysosomes or mitochondria. Previously, we have argued that the fluorescence excitation spectra of APT in cells is consistent with the dye being localized in an acidic medium such as lysosomes. The Stark measurements, however, would argue for at least some of the APT being located near the plasma membrane. This conclusion is based upon the attenuation that occurs within the cytoplasm when an external electric field is applied to a cell. This may be calculated by assuming that the cell is spherical and composed of a sphere of cytoplasm surrounded by a thin membrane. The resistivity of the membrane is much higher than that of the cytoplasm. The effective field within the cytoplasm sphere is then equal to the ratio of the product of cytoplasm resistance times its radius to the membrane resistance times its thickness [18]. For typical membrane and cytoplasm resistances, the field within the cytoplasm is calculated to be attenuated by a factor of $\sim 10^4$. For such a low effective field, a Stark effect would not be observable. Note that this

does not exclude the possibility of some of the dye being in lysosomes. However, such molecules would not contribute to the Stark effect although they would contribute to the hole burned in zero field. That only dye molecules associated with the membrane contribute to the Stark broadening can also explain why Stark hole-burning can distinguish between normal and cancerous cells while other hole-burning properties do not. It is well established that the cellular morphology, i.e., the plasma membrane and cytoskeleton, of cancer cells are distinctly different from normal cells. Thus dye in the membrane of the two cell types must experience distinctly different environments. The ordering of APT within MCF-10F cells, which we have said to be the result of $\Delta\mu_{ind}$ (non-random), would then be attributed to the influence of the cell membrane potential on APT. We must mention that further work is needed to verify that APT is, in fact, associated with the cell membrane of the two cell lines and that Stark hole burning is able to distinguish between the cell membrane of normal and cancer cells. We are currently investigating the effect of staining time to determine whether differences in Stark effects can be enhanced by increased localization of dye molecules at the cell membrane.

References

1. Milanovich, N.; Reinot, T.; Hayes, J. M.; Small, G. J. *Biophys. J.* **1998**, *74*, 2680.

2. Jankowiak, R.; Small, G. J. *Science* **1987**, *237*, 618.

3. Kim, W.-H.; Reinot, T.; Hayes, J. M.; Small, G. J. *J. Phys. Chem.* **1995**, *19*, 7300.

4. Reinot, T.; Kim, W.-H.; Hayes, J. M.; Small, G. J., *J. Chem. Phys.* **1996**, *3*, 793.

5. Reinot, T.; Kim, W.-H.; Hayes, J. M.; Small, G. J., *J. Opt. Soc. Am. B* **1997**, *3*, 602.

6. Reinot, T.; Hayes, J. M.; Small, G. J., *J. Chem. Phys.* **106**, *2*, 457.

7. Resnicoff, M.; Medrano, E. E.; Podhajcer, O. L.; Bravo, A. I.; Bover, L.; Mordoh, J. *Proc. Natl. Acad. Sci. USA* **1987**, *84*, 7295.

8. Shu, L.; Small, G. J., *J. Opt. Soc. Am. B* **1992**, *5*, 733.

9. Kador, L.; Haarer, D.; Personov, R., *J. Chem. Phys.* **1987**, *10*, 5300.

10. Meixner, A. J.; Renn, A.; Bucher, S. E.; Wild, U. P., *J. Phys. Chem.* **1986**, *26*, 6777.

11. Vauthey, E.; Holliday, K.; Changjiang, W.; Renn, A.; Wild, U. P. *Chem. Phys.* **1993**, *171*, 253.

12. Peng, Q.; Farrants, G. W.; Madslien, K.; Bommer, J. C.; Moan, J.; Danielsen, H. E.; Nesland, J. M., *Int. J. Cancer* **1991**, *49*, 290.

13. Robinson, R. S.; Roberts, A. S.; Campbell, I. D., *Photochem. Photobiol.* **1987**, *45*, 231.

14. Müller, M.; Reich, E.; Steiner, U.; Heicappell, R.; Miller, K. *Eur. Urol.* **1997**, *32*, 339.

15. Keith, A. D.; Arruda, D H.; Ruhlig, L; Snipes, W.; Verbalis, A. In *The Aqueous Cytoplasm*, Keith, A. D., Ed. Marcel Dekker, Inc.: New York, **1979**, 192.

16. Petty, H. R. *Molecular Biology of Membranes: Structure and Function*; Plenum: New York, **1993**, 7.

17. Alberts, B.; Bray, D.; Lewis, J.; Raff, M.; Roberts, K; Watson, J. D. *Molecular Biology of the Cell*; Garland Publishing: New York, Third Ed., 1994, 477.

18. Poo, M.-M., *Ann. Rev. Biophys. Bioeng.*, **1981**, *10*, 245.

CHAPTER 6. CONCLUDING REMARKS

Presented in this dissertation is the successful demonstration that nonphotochemical hole burning can be used to study in vitro cellular systems. From the results presented in Chapters 3 and 4, and Appendix B, the following conclusions are drawn:

- Nonphotochemical hole burning in cells is possible, implying that the host environment for the probe molecule is amorphous and the standard hole burning parameters, γ, λ_o, σ_λ, and S have been determined for MCF-10F cells.
- Fluorescence excitation spectra for APT in media and in cells confirm that APT is found in the cells, suggesting that the intracellular environment of APT is amorphous at liquid helium temperatures.
- A comparison of fluorescence excitation spectra and hole growth kinetics for APT in hyperquenched glassy water, ethanol, and methanol with APT in MCF-10F cells suggest that APT in cells is found in an acidic, water-like environment with a hydrogen-bonding network modified by other intracellular species.
- Effects of hydrostatic helium gas pressure on holes burned in APT-stained MCF-10F and MCF-7 cells in suspension were used to determine the compressibility of the two cell types, which were found to be the same for both cell lines.
- Effects of an external electric (Stark) field on nonphotochemical holes have been used to determine the change in dipole moment for APT in MCF-10F and MCF-7 cells in suspension. Differences are detected between the change in dipole moment for APT in the two cell lines when burn laser polarization is parallel to the Stark field.

- Results for APT in the two cell lines have shown that hole burning is possible for cells adhering to a coverslip and cooled to liquid helium temperatures in the complete absence of cryopreservatives.
- A comparison of hole burning parameters obtained for cells in suspension and cells adhering to coverslips have shown detectable differences for the same cell type for these two sample preparations.

These conclusions demonstrate that hole burning has the potential of providing detailed information about localized intracellular environments and for detecting changes in the physical characteristics (eg., electrical and mechanical properties) of cells. For the latter, the long-term goal will be to develop nonphotochemical hole burning into a diagnostic technique for the early detection of cancer by exploiting the physical differences between normal and cancerous cells and tissues.

Now that a working model has been established for MCF-10F and MCF-7 cells and the "test" molecule, APT, future work will include finding other probe molecules that are both site-selective and that will hole burn. Some commercially available dyes have been screened as potential candidates, but, unfortunately, have been unable to satisfy the necessary criteria for use in hole burning experiments on cells. Therefore, a custom-designed probe molecule that is both site-specific and will hole burn has already been synthesized (see Appendix C). Although preliminary, the results with this "molecular thumbtack" appears promising, but more work must be done to further characterize this molecule. Once a suitable probe molecule is identified and is able to detect cancer-related differences in well-

defined, in vitro systems, work on clinical samples, i.e., tissue sections from biopsies, would begin in order to test the applicability of hole burning to cancer diagnostics. In conclusion, the application of hole burning to cellular systems and tissues has the potential for being a useful tool for basic research in the biological sciences and as a clinical technique.

APPENDIX A. CHARACTERIZATION OF MCF-10F AND MCF-7 CELLS AND SUBCELLULAR DISTRIBUTION OF ALUMINUM PHTHALOCYANINE TETRASULFONATE

Given in Section 3.4 are general descriptions of MCF-10F, normal human breast (luminal ductal) epithelial cells and MCF-7, adenocarcinoma cells. Shown in Figure A-1 are optical microscope images of MCF-10F (Figure A-1a) and MCF-7 cells (Figure A-1b), at 20x magnification, obtained with an Olympus IMT-2 microscope using differential interference contrast to aid in visualizing internal cellular structures. The images in Figure A-1 are of the two cell types while growing in the culture flasks. A general characteristic of normal cells growing in culture is that they grow such that a monolayer of cells is formed on the surface of the culture flask, as seen in Figure A-1a for MCF-10F cells. Furthermore, normal cells typically spread-out on the surface, thereby occupying any space on that surface not already occupied by another cell. The cells will continue to grow in this way until they come in contact with other cells and, thus, prevent further spreading of the cells on the surface of the culture flask. When this occurs, the cells are said to have undergone cell-contact inhibition. In contrast, cancer cells, such as MCF-7 cells, do not grow as organized monolayers and they do not adhere to substrata as strongly as normal cells. Depicted in Figure A-1b are MCF-7 cells whereby a secondary layer of cells (2) is growing on top of a monolayer of MCF-7 cells adhering to the surface of the culture flask (1). Moreover, the lessened ability of MCF-7 cells to adhere to substrata results in the cancer cells spreading out on a surface much less than normal cells.

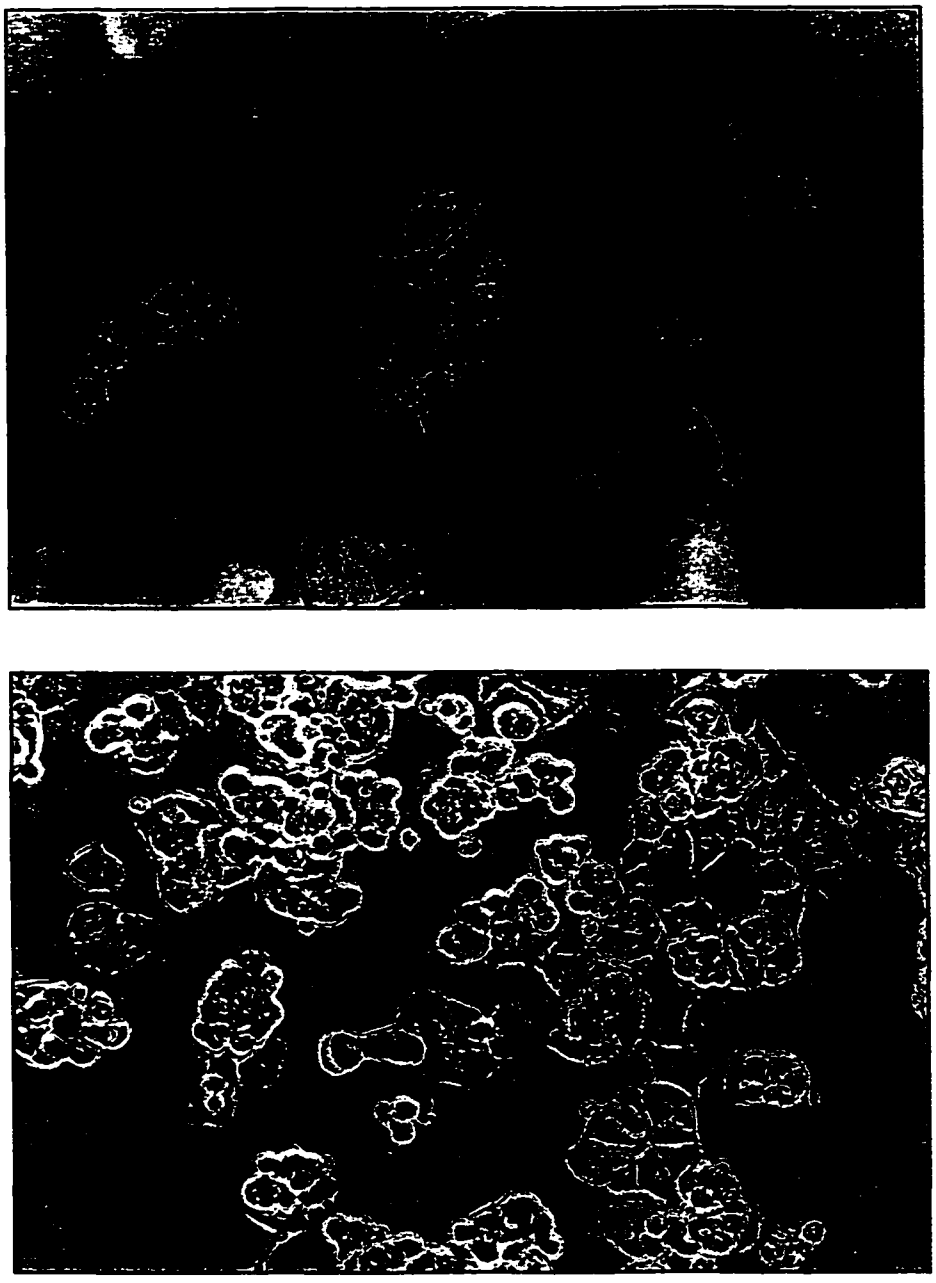

Figure A-1. Optical microscope images of a) MCF-10F and b) MCF-7 cells growing in culture. (1) denotes cells forming a monolayer on the surface of the culture flask and (2) denotes cells growing on top of (1). Note that MCF-10F (normal) cells grow as monolayers while MCF-7 cells grow on top of other MCF-7 cells.

Cell samples used in the work presented in this dissertation were prepared as suspensions. Including in the suspension media was the MCF-10F or MCF-7 culture media which contained the pH indicator, phenol red, previously discussed in Section 3.6.1. Shown in Figure A-2 is a room temperature absorption spectrum for MCF-10F culture medium and the contents of MCF-10F cells stained with APT. This sample was prepared by staining MCF-10F cells with APT for 19 h followed by washing the cells with phosphate-buffered saline (PBS) three times to remove excess dye. The cells were then lysed with Triton X-10 and centrifuged for 5 min. at 1500 rpm. The supernatant was then drawn-off and used to obtain the absorption spectrum in Figure A-2. The absorption ranging from ~ 630 nm to 300 nm is due solely to the components of the culture medium, including phenol red absorption at 560 nm. MCF-7 culture medium gave an absorption spectrum (spectrum not shown) that was nearly identical to the one in Figure A-2. Absorption > 630 nm is that of APT (λ_{max} = 674 nm). It should be noted that the APT present in this sample was the result of dye uptake by the MCF-10F cells. Based on the the optical density of APT in this sample (0.072, $\varepsilon \sim 1.3 \times 10^5$ cm^{-1} M^{-1}), the intracellular concentration of dye was 5.6 nmol/10^7 cells for a 19 h staining time. The intracellular dye concentration was comparable to the concentration of APT uptake (~7 nmol/10^7 cells) found for chinese hamster fibroblasts, line V79-B310H, for a 19 h staining time. [1]

In order to interpret hole burning results with cellular properties, the intracellular distribution of APT must be determined. Given in Figure A-3 are single sections of laser confocal microscope images for a) MCF-10F and b) MCF-7 cells stained with 10^{-4} M APT

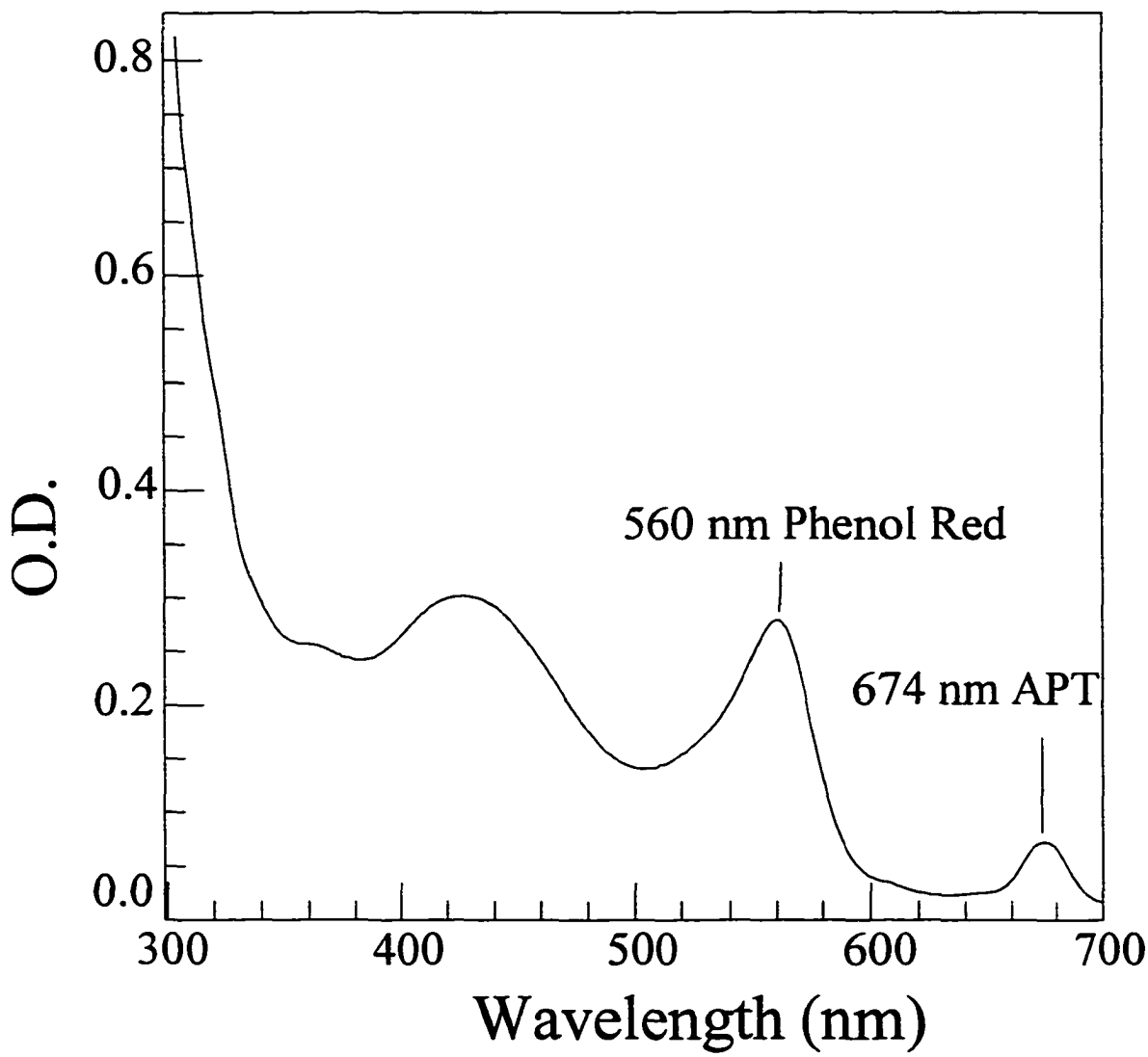

Figure A-2. Room temperature absorption of MCF-10F culture medium and MCF-10F cell content, including APT.

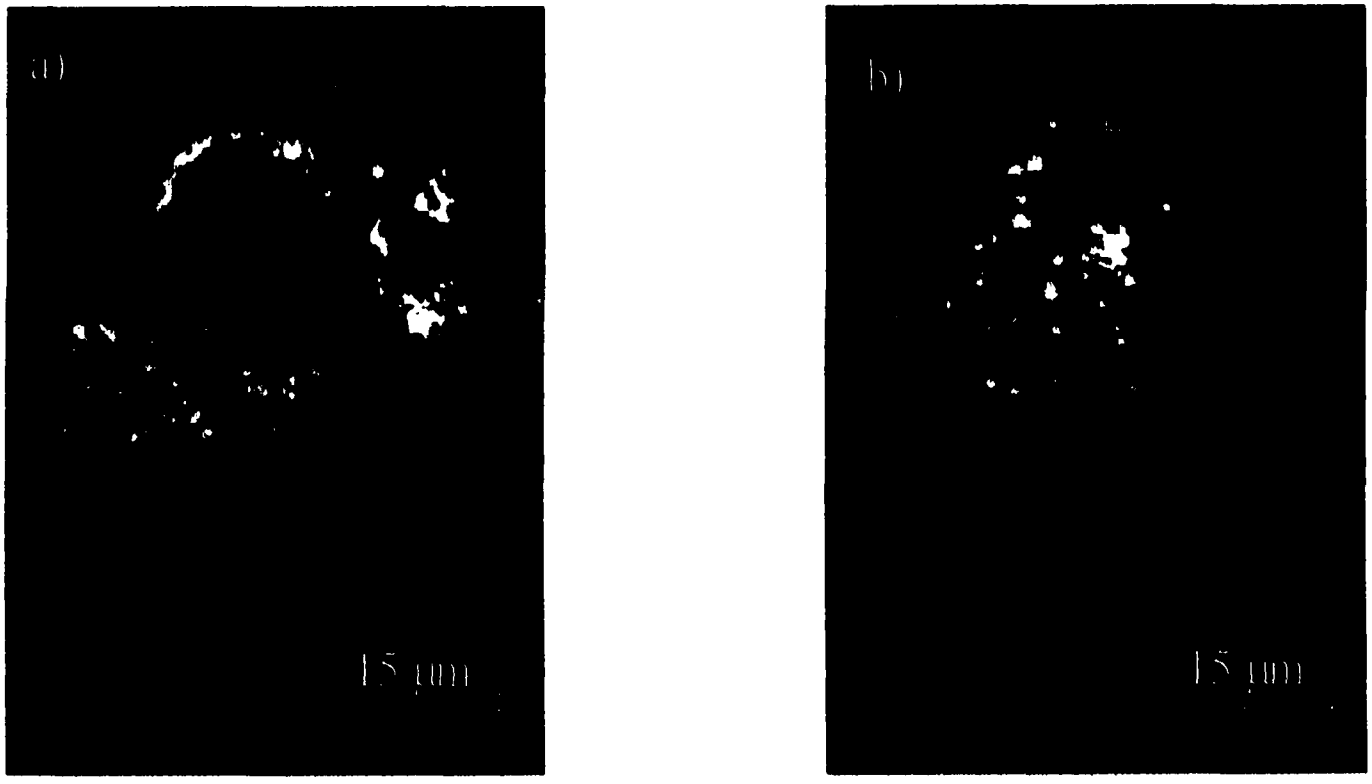

Figure A-3. Confocal microscope images of a) MCF-10F cells and b) MCF-7 cells stained with APT at 100x magnification. Bright spots of fluorescence indicate APT localization within the cell. Less intense, diffuse fluorescence of APT is also present throughout the cytoplasm of both cell types.

for 19 h. The section thickness for Figures A-3a and -b are 0.8 and 0.6 μm, respectively. Samples were prepared according to the procedure by Peng and coworkers [2] and images were taken with a Leica TCS-NT Confocal Microscope System (Leica Microsystems, Inc., Exton, PA). The samples were excited with a HeNe laser and the images in Figure A-3 were taken using a 100x objective lense and immersion oil. A long-pass filter was used to remove fluorescence occurring at wavelengths less than 645 nm. Similar to the results obtained for LOX cells stained with APT [2], the cells in Figures A-3a, and -b exhibited bright spots of fluorescence dispersed throughout the cytoplasm as a result of dye localization in lysosomes. In addition, diffuse fluorescence throughout the cytoplasm was also observed for MCF-10F and MCF-7 cells, including the nucleus. The diffuse fluorescence in MCF-10F and MCF-7 cells is the result of redistribution of dye from lysosomes to the cytoplasm (and, to a minor extent, the nucleus) following laser irradiation, also observed for LOX cells. [2]

In conclusion, the two model cell lines used in this dissertation, MCF-10F and MCF-7 cells, exhibit the characteristic growing patterns of normal and cancerous cells, respectively. The absorption spectrum for APT and the MCF-10F suspension medium serves as an example of the presence of additional absorbing species found in the MCF-10F and MCF-7 suspension media. Finally, laser confocal images of MCF-10F and MCF-7 cells stained with APT showed both localized fluorescence, thought to be APT contained in lysosomes, and diffuse fluorescence throughout the cytoplasm.

References

1. Ben-Hur, E.; Siwecki, J. A.; Newman, H. C.; Crane, S. W.; Rosenthal, I. *Cancer Lett.* **1987**, *38*, 215.

2. Peng, Q.; Farrants, G. W.; Madslien, K.; Bommer, J. C.; Moan, J.; Danielsen, H. E.; Nesland, J. M. *Int. J. Cancer*. **1991**, *49*, 290

APPENDIX B. CELL SUSPENSION VS. COVERSLIP

B.1 Introduction

The first examples of hole burning experiments on cellular systems (See Chapters 4 and 5) were carried out on cultured cells in suspension. Cell suspensions were prepared because of concerns over the possible formation of intracellular ice crystals which would, in turn, affect the morphology of cells. Furthermore, Kim et al. [1] have shown that APT will not hole burn when the matrix is ice. As a result, the cell samples were prepared as suspensions, containing cryopreservatives, based on results by Farrant et al. [2] demonstrating that V79 Chinese hamster cells in the presence of a cryopreservative and cooled by a two-step process avoided intracellular ice formation.

In light of these experiments, one point of contention with the samples being prepared as suspensions is whether the probe molecules are located inside the cell, or in the suspension medium. In Chapter 4, a comparison between the fluorescence excitation spectra of 10^{-5} M APT in the MCF-10F suspension medium resulted in a much broader band with a red-shifted peak maximum relative to that of APT in MCF-10F cells. This relation is also observed for APT in the MCF-7 suspension medium versus APT in MCF-7 cells. These results suggest that the environment of APT in the cell samples is different from that in suspension media. However, despite the favorable results obtained from fluorescence excitation, the general effects of having cells in suspension remains uncertain. Therefore, cells adherent to a glass coverslip were prepared in the complete absence of suspension media, afterwhich hole burning measurements were performed on the samples. The disadvantage to using cell

samples on a coverslip to do hole burning is that, unlike cell suspensions, the samples can only be used once and must then be discarded. Nonetheless, cells adhering to a substratum provide a more organized system in that the morphology of cells such as epithelial cells (eg., MCF-10F and MCF-7 cells) is affected by a cell's ability to organize and form tight junctions with adjacent cells [3-5]. Cells grown on coverslip are also more similar to tissue samples prepared on glass slides in that an organized sample arrangement on a surface will allow for selective probing of various sample regions with the probe beam. Presented here are preliminary hole burning measurements for cell samples prepared on a coverslip.

B.2 Experimental Section

Sample Preparation The experimental protocol for cells prepared in suspension and hole burning measurements taken thereafter are described in Chapter 4. For samples prepared on coverslip, an autoclaved, glass coverslip (18 mm x 18 mm) was placed in each well of a six-well culture plate. Cells and the appropriate culture medium were then added to each of the wells of the culture plate and allowed to incubate overnight at 37 °C, in a 5% CO_2 atmosphere. Cells were stained on the following day with APT having a final concentration of 10^{-4} M and allowed to incubate for 18-19 h at 37 °C, in a 5% CO_2 atmosphere. After incubation, cells were washed three times with fresh media (3 mL/wash) followed by three washs with phosphate-buffered saline (PBS) at 3 mL PBS per wash in order to remove excess APT. Samples were then kept in PBS until ready for hole burning experiments.

Hole Burning Experiments The laser system used in the present hole burning experiments has previously been described in Chapter 4. Samples on coverslip were removed from the

PBS solution and excess solution was allowed to drain by touching a corner of the coverslip to a paper towel. The coverslip was then mounted on a removable sampleholder located at the end of the cryostat's sample rod. The sampleholder consisted of a copper plate with a 10 mm hole in the center. As a whole, the sample rod and holder was oriented horizontally and the coverslip was then positioned on top of the hole on the copper plate. An o-ring spacer made of teflon was placed on the coverslip, followed by another copper plate with a 10 mm hole (which provided laser beam access to the sample). This second copper plate was screwed into the main plate to keep the sample in place and the spacer was used to prevent movement of the coverslip between the two plates. After mounting, the sample was immediately plunged into the cryostat, which was precooled to 4.5 K.

B.3 Results and Discussion

Figure B-1 compares the fluorescence excitation spectra of APT-stained MCF-10F and MCF-7 cell samples on coverslip. In this Figure, the fluorescence excitation spectra of APT in MCF-10F and MCF-7 cells have nearly identical bands. However, neither of these two bands have the characteristic flat top or two partially resolved peaks observed in previous NPHB studies with APT as the probe molecule (see Figures 4-2 and 5-1). The two APT bands are, nonetheless, composed of two separate bands attributed to Q_x and Q_y splitting of the phthalocyanine ring [6]. By fitting the fluorescence excitation profiles with two Gaussian functions, the lower energy band was determined to have a peak maximum of 674.4 nm and 673.5 nm for APT in MCF-10F and MCF-7 cells on a coverslip, respectively. This contrasts with the values reported for Gaussian fits for APT in MCF-10F (675.4 nm) and MCF-7 cells

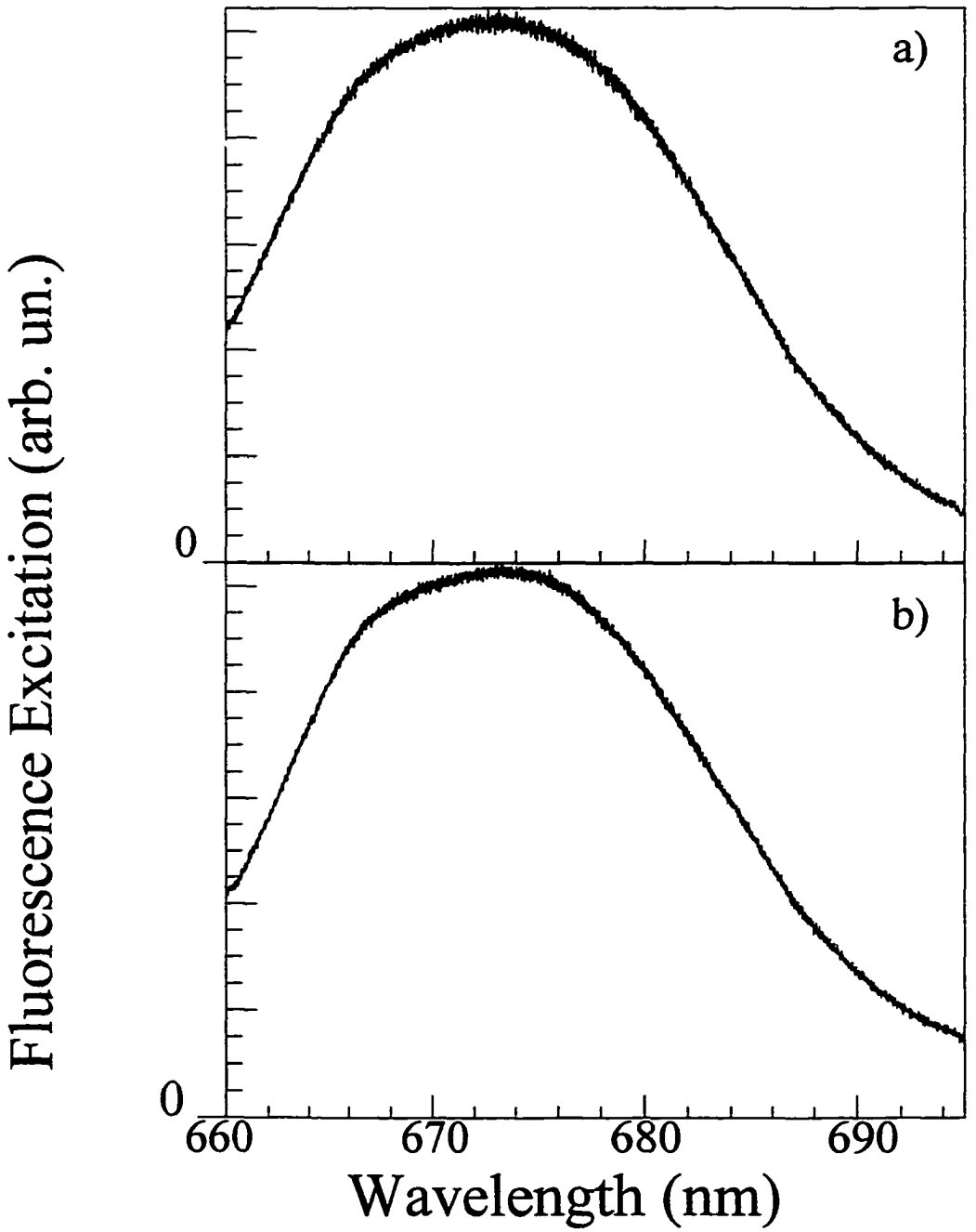

Figure B-1. Fluorescence excitation spectra of APT-stained a) MCF-10F and b) MCF-7 cells prepared on a coverslip. The spectra in a) and b) overlap appreciably and, thus, were separated into two panels for clarity.

(676.2 nm) in suspension [7, 8]. Differences between the spectra of APT in cells grown in suspension versus coverslip are already observed, even before the samples are hole burned. One possibility for this difference is the presence of penetrating cryopreservatives such as DMSO and glycerol,

which are both components of the suspension media and, thus, interact with the intracellular APT molecules. Cell samples on a coverslip are devoid of cryopreservatives and, therefore, the nearly identical fluorescence excitation profiles for these two cell types come about from almost indistinguishable intracellular APT environments. Moreover, the presence of glycerol in an APT/water sample is known to red-shift the fluorescence excitation maximum (unpublished results) relative to an APT/water sample. This observation is consistent with the relative peak maxima for cells on a coverslip and in suspension. This logic is further supported by considering the relative peak maxima for MCF-10F cells and MCF-7 cells in suspension. For instance, if the plasma membranes of cancer cells are considered less selectively permeable than normal cells, then one can infer that more of the penetrating cryopreservatives, *viz.*, DMSO and glycerol, will penetrate the cell membrane of MCF-7 cells than MCF-10F cells. This, in turn, would result in a fluorescence excitation maximum for MCF-7 cells to be red-shifted from MCF-10F cells, which is precisely what is observed.

In Figure B-2, action spectra for APT in the two cell types is shown for cells grown on coverslip. As shown by the holes burned across the fluorescence excitation bands for the cells on coverslip, narrow ZPH's can be burned into the low energy band of the absorption profile, but not the high energy band. These results suggest that the APT intracellular

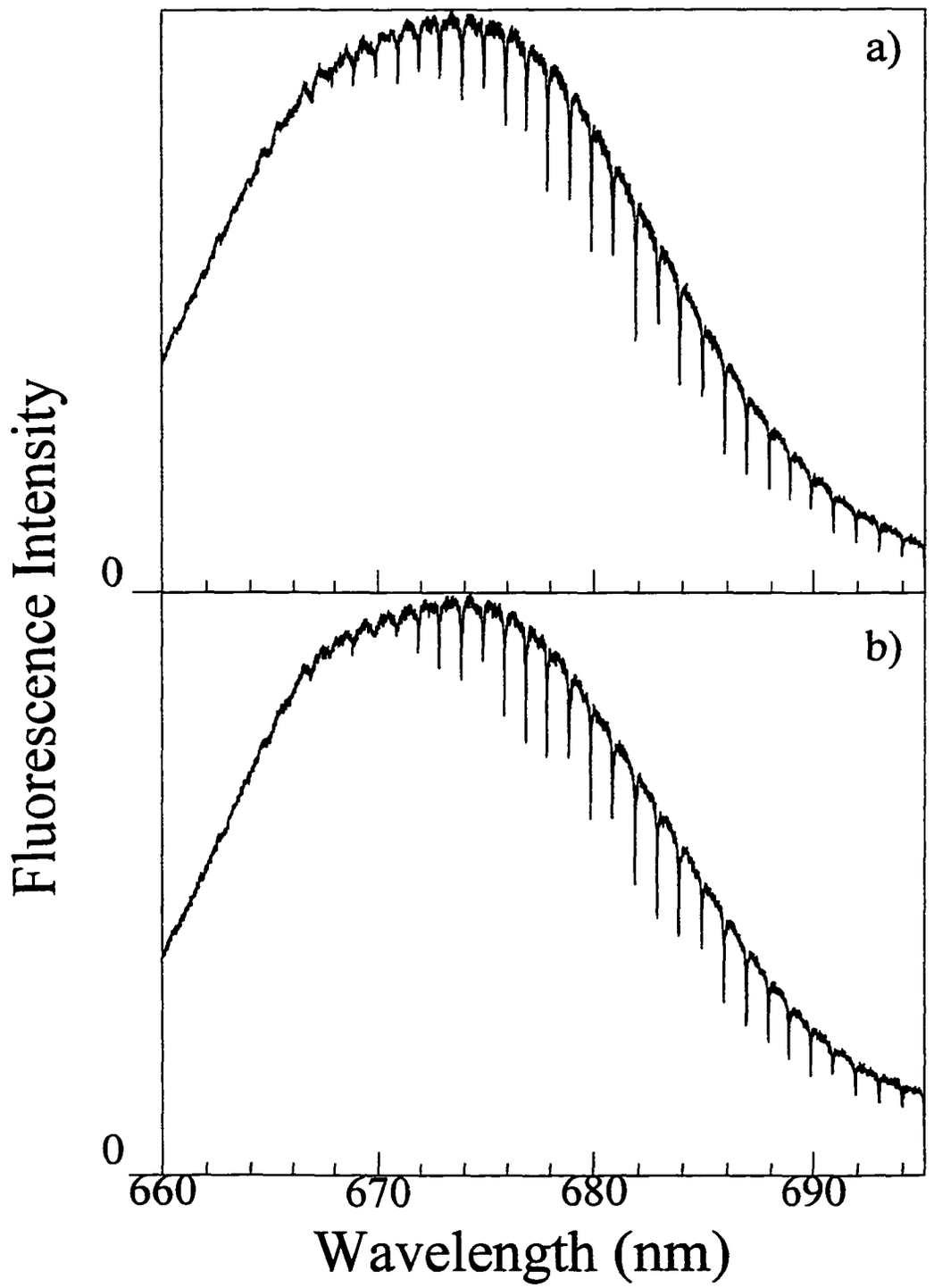

Figure B-2. Action spectra of APT-stained a) MCF-10F and b) MCF-7 cells prepared on a coverslip. As in the previous figure, the spectra in a) and b) overlap appreciably and, thus, were separated into two panels for clarity.

environment for cells on coverslip is, in fact, amorphous and hole burning of APT for the samples on coverslip is similar to that for cells in suspension.

Hole width and hole growth kinetics measurements were made for cells on coverslip under the same conditions as those obtained for cells in suspension [7, Chapter 4] and are summarized in Table B-1. Holes having a fractional hole depth of ~10% resulted in hole widths (FWHM) for cells on coverslips being twice that of cells in suspension. Furthermore, the values for λ_0 were the same for both coverslip and suspension while σ_λ and the Huang-Rhys factor, S, were somewhat greater for cells on coverslips. Note that based on inconsistent kinetics results for MCF-7 cells in suspension due to the heterogeneity of this cell line [9] the results obtained for MCF-7 cells on coverslips be unreliable. Kinetics results for MCF-10F cells in suspension, on the other hand, have been consistent and, thus, these results can be considered reliable.

Based on the results summarized in Table B-1, the degree of disorder of the APT environment for cells on coverslip is interpreted as being greater than the disorder for cells in suspension. This increased disorder can be described in terms of cell morphology as follows. A cell, when in suspension, is best able to withstand mechanical stress by assuming a spherical shape and, thus, preserving the structural integrity of the cell with this ordered, symmetric shape. In contrast, adherence of a cell to a substratum disrupts the spherical order found in a cell in suspension, ie., attachment to a surface causes a portion of the cell membrane to flatten in the same way the membrane of a spherical balloon flattens when pressed on a flat surface. A cell's shape is further distorted by forming attachments to

adjacent cells at various loci on the cell membrane which, using the balloon analogy, would be similar to pinching the balloon membrane in various places while the balloon is already pressed against a flat surface. In terms of the mechanical strength of a tissue, these cell-cell and cell-substrate interactions result in stronger tissue at the expense of an individual cell's strength. Therefore, cells on a coverslip can be viewed as less symmetric and more

Table B-1. List of hole burning results.

Sample	Hole Width (GHz)*	λ_0	σ_λ	S
MCF-10F-coverslip	2.8 (0.09)	9.1	1.18	0.49
MCF-10F-suspension [7]	1.5 (0.09)	9.1	0.96	0.36
MCF-7-coverslip	2.9 (0.1)	9.1	1.22	0.57
MCF-7-suspension [7]	1.5 (0.09)	-	-	-

* Values in parentheses refer to fractional hole depth of hole used to determine hole width.

disordered structurally than cells in suspension because of a cell's attachment to the coverslip surface and adjacent cells.

B.4 Conclusion

A comparison of the fluorescence excitation spectra for APT in MCF-10F and MCF-7 cell samples prepared on a coverslip to those in suspension has shown differences in position of the peak maxima. The positions of the peak maxima are susceptible to the presence of glycerol, which is able to penetrate the plasma membrane and is thought to cause the red-

shifted peaks for cells in suspension. Action spectra for APT in cells on coverslips indict that the intracellular environment of APT is, in fact, amorphous. Furthermore, the ability to burn narrow and deep ZPH's into the low energy band of APT is consistent with other NPHB systems using APT as the probe molecule, including cells prepared in suspension [7]. Finally, hole width and hole growth kinetics measurements were able to distinguish between cells in suspension and on coverslip. This difference can be attributed to the structural disorder brought about by morphological distortion of a cell upon formation of cell-cell and cell-substrate interactions.

References

1. Kim, W.-H.; Reinot, T.; Hayes, J. M.; Small, G. J. *J. Phys. Chem.* **1995**, *99*, 7300.
2. Farrant, J.; Walter, C. A.; Lee, H.; Morris, G. J.; Clarke, K. J. *J. Microscopy*, **1977**, *111*, 17.
3. Simons, K.; Fuller, S. D. *Ann. Rev. Cell Biol.* **1985**, *1*, 243.
4. Rodriguez-Boulan, E.; Nelson, W. J. *Science* **1989**, *245*, 718.
5. Fish, E. M.; Molitoris, B. A.; *New Eng. J. Med.* **1994**, *330*, 1580.
6. Reinot, T.; Hayes, J. M.; Small, G. J.; Zerner, M. C. *Chem. Phys. Lett.* **1999**, *299*, 410.
7. Milanovich, N.; Reinot, T.; Hayes, J. M.; Small, G. J. *Biophys. J.* **1998**, *74*, 2680.
8. Milanovich, N.; Rätsep, M.; Reinot, T.; Hayes, J. M.; Small, G. J. *J. Phys. Chem. B*, **1998**, *102*, 4265.
9. Resnicoff, M.; Medrano, E. E.; Podhajcer, O. L.; Bravo, A. I.; Bover, L.; Mordoh, J. *Proc. Natl. Acad. Sci. USA*. **1987**, *84*, 7295.

APPENDIX C. MOLECULAR THUMBTACKS

Based on the interpretation of results from Stark hole burning between MCF-10F and MCF-7 cells, a new membrane dye was sought to enhance the differences observed with APT. However, the unavailability of suitable commercial dyes for application of NPHB to cellular systems has prompted the design of a novel biological dye referred to as a molecular thumbtack (MTT), whose structure is given in Figure C-1. The two important features of this molecule are the pthalocyanine ring and the twelve-carbon fatty acyl chain, which provides a chromophore known to hole burn and hydrocarbon chain that is a common structural feature of lipid membranes. To distinguish this MTT from future derivatives, this molecule will henceforth be referred to as $SiPcC_{12}\phi$ (MW 818.12).

Shown in Figure C-2 is the room temperature UV-VIS spectrum for ~ 2 mM $SiPcC_{12}\phi$ in DMSO ($\varepsilon \sim 2 \times 10^3$ cm^{-1} M^{-1}) using a quartz cuvette (1 cm path length). Spectra were acquired with a Perkin-Elmer UV-VIS spectrometer using a 1.0 nm resolution. It should be noted that DMSO was arbitrarily chosen as the solvent and sonication was required to dissolve the dye. A preferred solvent for $SiPcC_{12}\phi$ is currently unknown. This spectrum resembles the room temperature absorption spectrum of APT in water (spectrum not shown). Interestingly, the absorption of $SiPcC_{12}\phi$ shows a partial splitting of the origin band (λ_{max} = 682 nm and 688 nm for the high and low energy bands, respectively). This splitting is observed for APT in various matrices, but only at cryogenic temperatures [1]. The splitting of the origin band of APT has been attributed to Q_x/Q_y splitting arising from the coordination of water molecules with aluminum [1]. Therefore, splitting of the origin band for $SiPcC_{12}\phi$

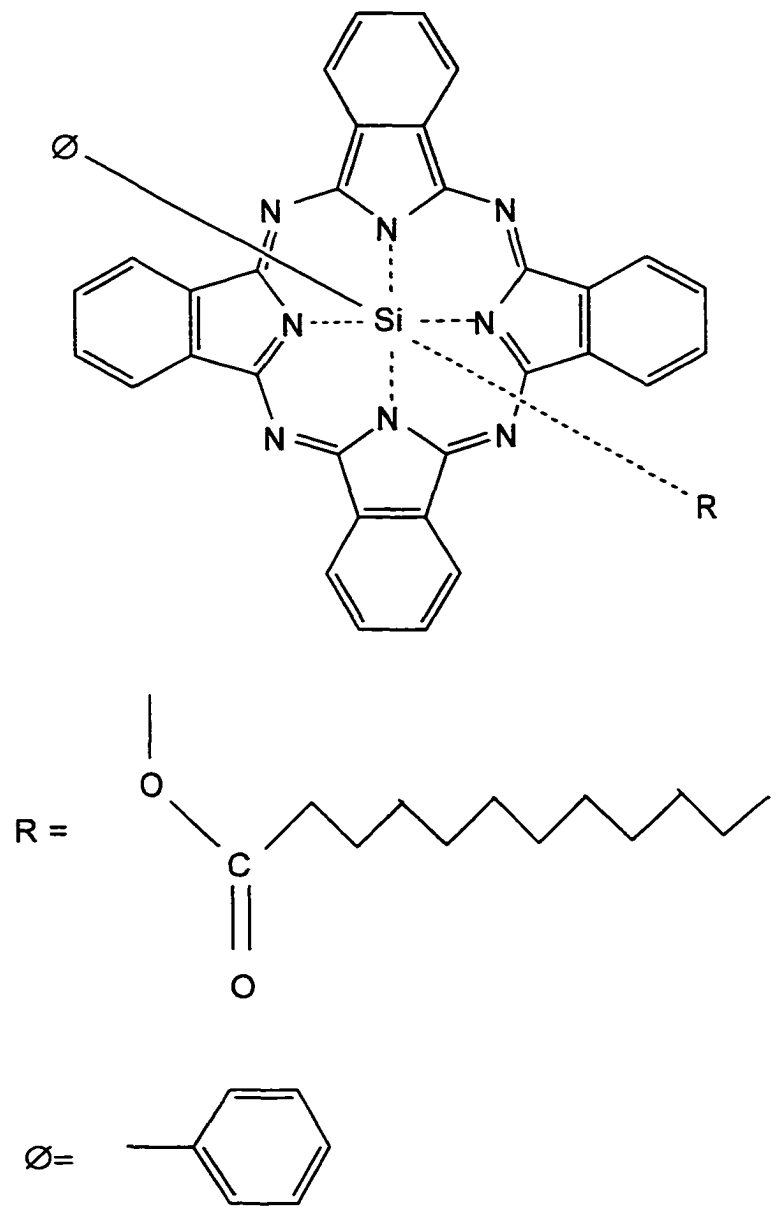

Figure C-1. Structure of the molecular thumbtack $SiPcC_{12}\phi$.

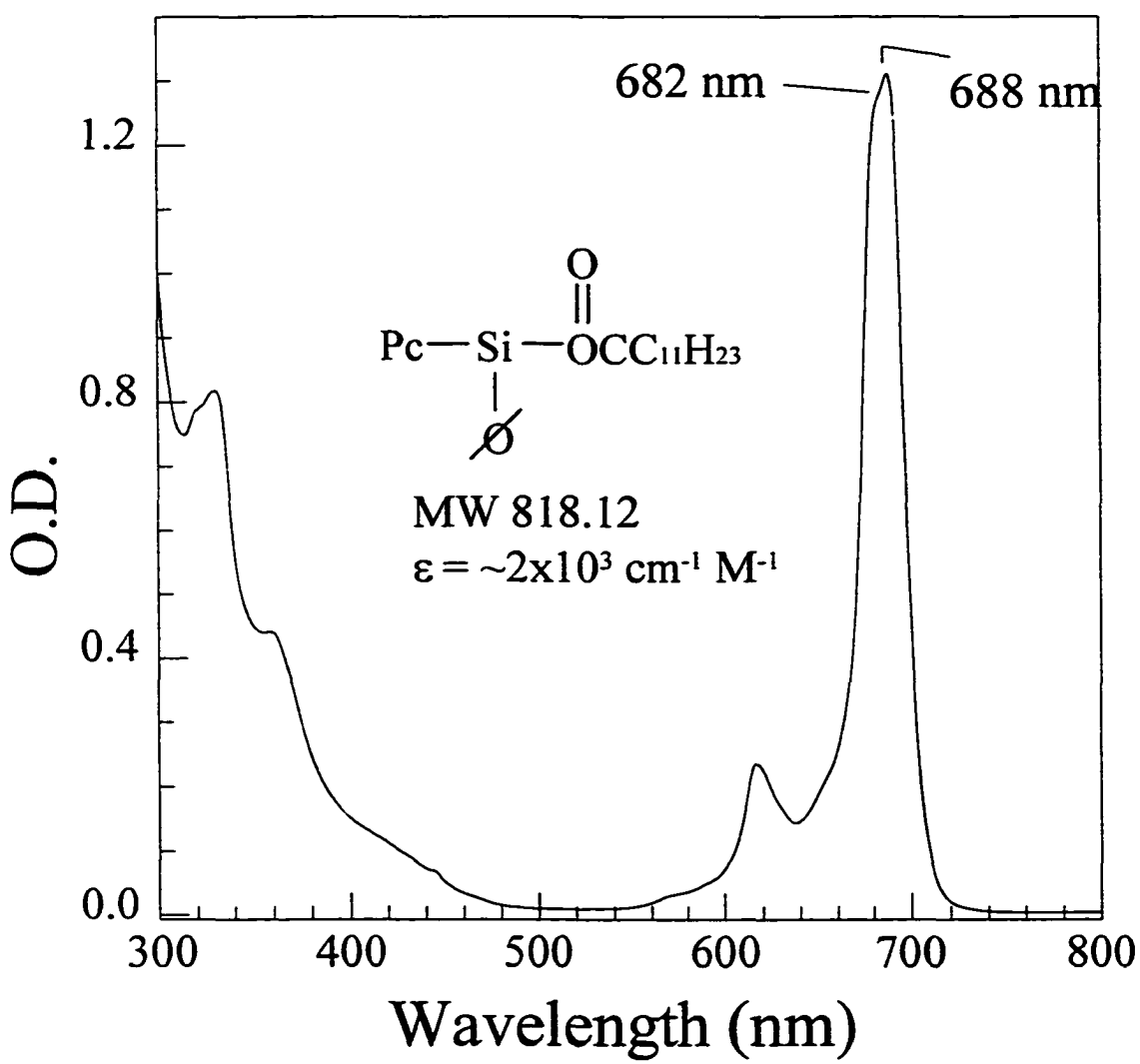

Figure C - 2. Room temperature absorption spectrum of 2 mM $SiPcC_{12}\phi$ in DMSO.

as a result of covalent bonding of both a phenyl group and a fatty acyl chain on opposing sides of the plane of the phthalocyanine should not be surprising.

Figure C-3a shows the pre-burn fluorescence excitation spectrum (1.0 cm^{-1}) for ~0.5 mM $SiPcC_{12}\phi$ in 1:3 (v/v) DMSO/glycerol taken at 1.8 K. At this temperature, the splitting between the Q_x/Q_y bands (λ_{max} = 682.0 nm and 694.1 nm for the high and low energy bands, respectively, with a splitting of 256 cm^{-1}) is better resolved than at room temperature, or for APT at low temperatures. The post-burn fluorescence excitation spectrum for $SiPcC_{12}\phi$ shows that when holes are burned at 1.0 nm intervals (0.2 mW/cm^2 laser power, at 20 s burn time per hole) from lower to higher energy across the absorption profile, only the lower energy band can be burned, which is the exact same behavior observed for APT [1, 2]. Burning a hole at λ_B = 695.5 nm (0.24 $\mu W/cm^2$, 60 s) yielded a hole with FWHM of 0.340 GHz and a fractional hole depth of 0.063 (inset, Figure C-3b), thus, demonstrating that hole widths in the range of those for APT are possible for $SiPcC_{12}\phi$.

In order to determine the biodistribution for $SiPcC_{12}\phi$, confocal microscope images were taken for MCF-10F and MCF-7 cells stained with ~ 7.3 x 10^{-4} M $SiPcC_{12}\phi$ and are presented in Figure C-4a and b, respectively. The confocal microscope system used to acquire these images was described in Appendix A. In addition, samples were prepared according to the protocol given in Appendix A for MCF-10F and MCF-7 cells stained with APT, except that staining time was only 15 min. As shown in these images, $SiPcC_{12}\phi$ fluorescence delineates the cell membrane, but no fluorescence is observed in the cell interior. For the MCF-10F cells (Figure C-4a), $SiPcC_{12}\phi$ appears primarily as localized

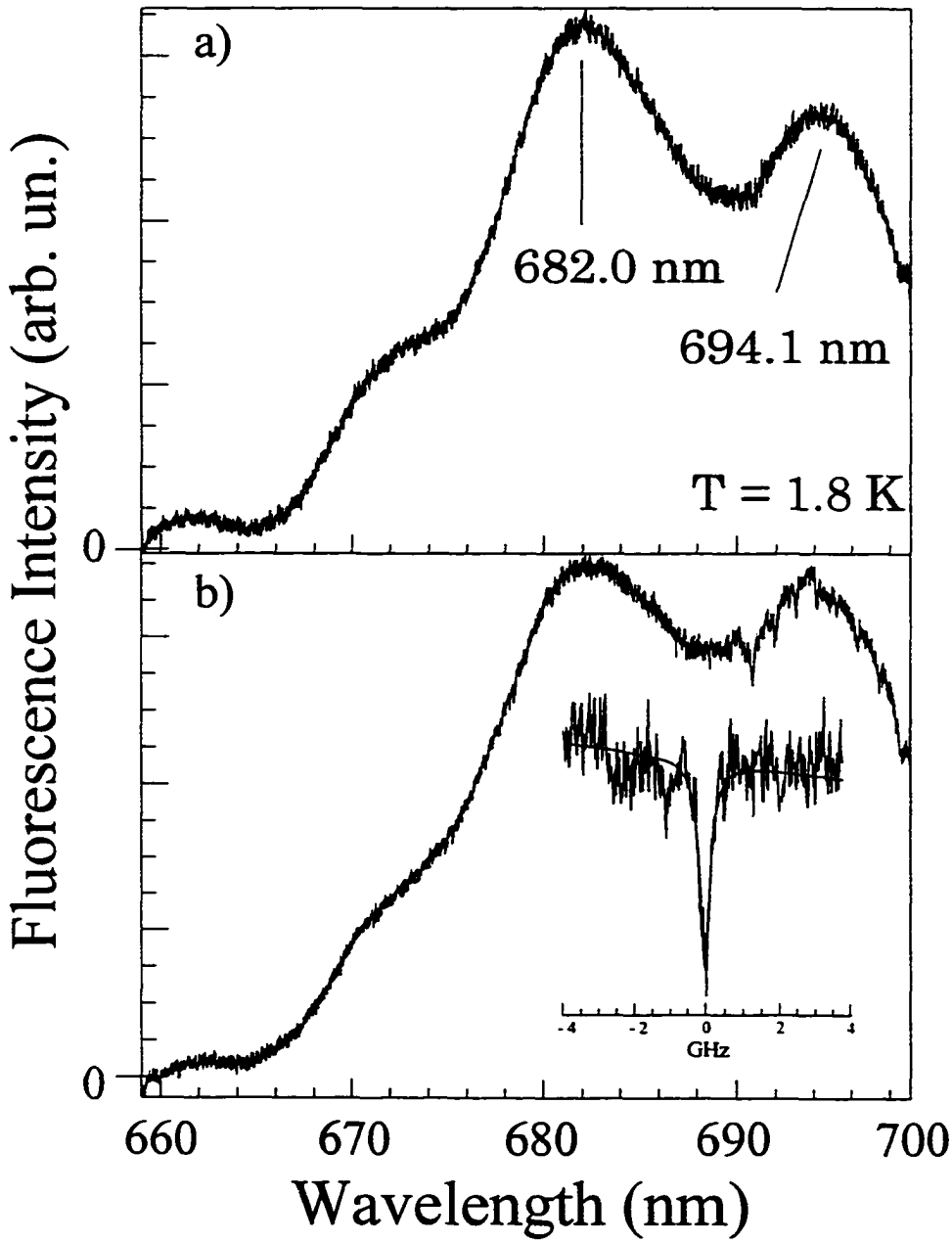

Figure C-3. Preburn fluorescence excitation spectrum a) and postburned spectrum b) of 0.5 mM $SiPcC_{12}\phi$ in 1:3 DMSO/glycerol. The inset of b) shows a hole spectrum and Lorentzian lineshape fit for $SiPcC_{12}\phi$. The fitting gave a hole with fractional depth of 0.06 and FWHM 0.340 GHz. This hole was burned at λ_B = 695.5 nm (0.24 $\mu W/cm^2$, 60 s).

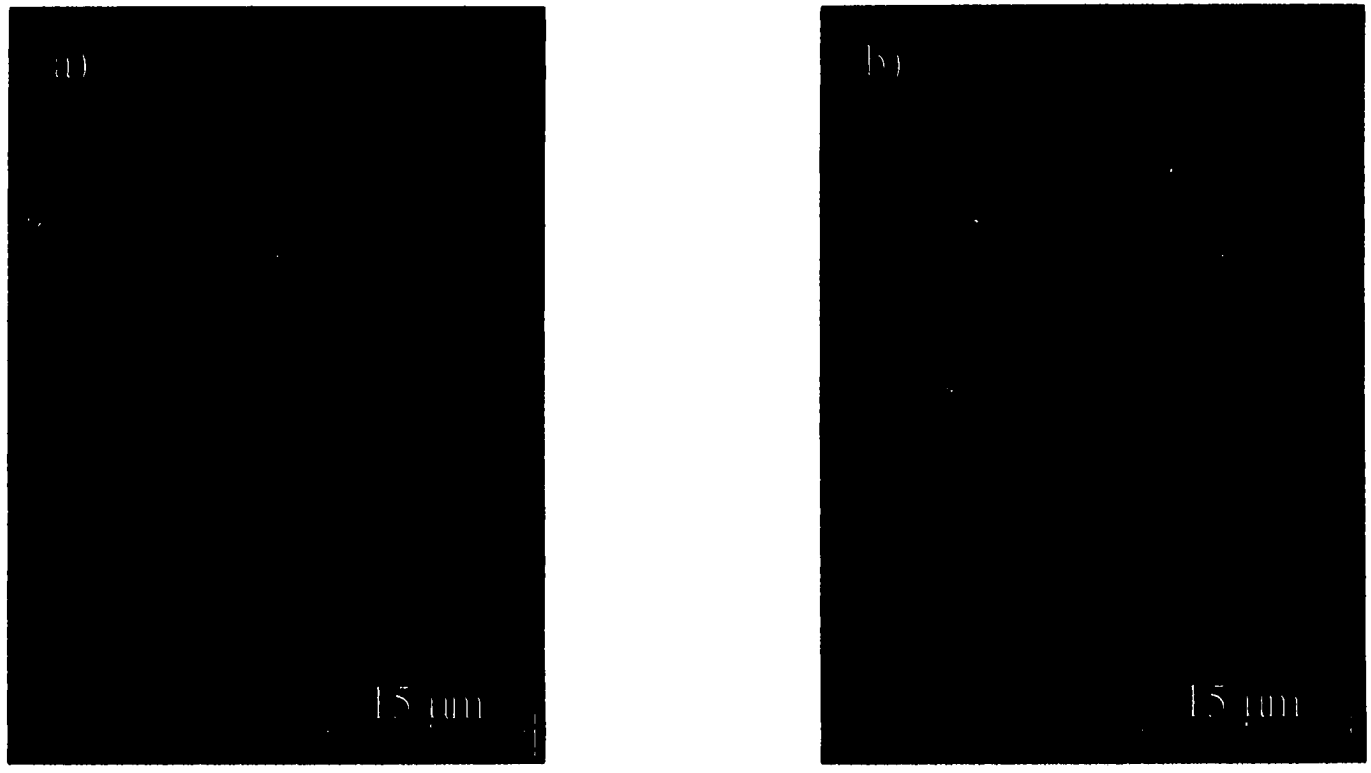

Figure C-4. Confocal microscope images of a) MCF-10F cells and b) MCF-7 cells stained with $SiPcC_{12}\phi$ at 100x magnification. $SiPcC_{12}\phi$ is shown to be specific for the plasma membrane with primarily localized fluorescence on the MCF-10F cell membrane. The fluorescence from the MCF-7 appears more diffuse than the MCF-7 cells.

fluorescence about the perimeter of the plasma membrane with some membrane regions having diffuse fluorescence. The fluorescence for MCF-7 cells stained with $SiPcC_{12}\phi$ (Figure C-4b) is also found at the plasma membrane, but is primarily diffuse. It is currently uncertain whether the differences in fluorescence for the two cell types is due to the membrane properties of the cells, or photodegradation of the dye. This result suggests that $SiPcC_{12}\phi$ is suitable for staining the cell membrane. In conclusion, the design of $SiPcC_{12}\phi$, as demonstrated by the spectroscopic results and the microscope images, indicate that $SiPcC_{12}\phi$ has both hole burning and cellular site-selective characteristics desired for application to cellular systems. The next step will be to perform hole burning experiments on MCF-10F and MCF-7 cells stained with $SiPcC_{12}\phi$ to determine the true utility of this dye.

References

1. Reinot, T.; Hayes, J. M.; Small, G. J., *J. Chem. Phys.* **1997**, *106*, 457.

2. Milanovich, N.; Reinot, T.; Hayes, J. M.; Small, G. J. *Biophys. J.* **1998**, *74*, 2680.

GLOSSARY OF BIOLOGICAL TERMS

Ankyrin Protein present on intracellular side of cell membrane in red blood cells. Interacts with spectrin and Band III protein.

Basal Lamina A thin collagenous layer forming part of the basement membrane and underlying epithelial tissue. Separates the epithelial layer from underlying tissue.

Basement Membrane Separates the epithelial layer from underlying tissue. Composed of basal lamina, mucopolysaccharides and a fine fibrous meshwork.

Carcinoma Malignant tumor of epithelial cells, eg., adenocarcinoma (cancer associated with glands) and squamous cell carcinoma (type of skin cancer).

Centriole Short array of microtubules arranged cylindrically and present in pairs in the center of centrosomes in animal cells.

Centrosome Animal cell organelle located near the nucleus and containing a pair of centrioles. Functions as a spindle pole during mitosis.

Cilia Hair-like extensions found on the surfaces of some eukaryotic cells, eg., epithelial cells lining the small intestine. Composed of a core bundle of microtubules that produce a beating motion producing a flow of nutrients over the cell membrane surface.

Cytotoxic Lethal to cells.

Desmosome Point on a cell membrane at which a cell-cell junction is formed.

Diploid Having a complete pair of homologous chromosomes thereby having two copies of each gene present in the chromosomes.

Endocytosis The process of the uptake of materials by a eukaryotic cell from the extracellular environment ("cell eating"). Materials are taken up such that invagination of the plasma membrane around the material results in the formation of vesicles containing the extracellular material (cf. pinocytosis and exocytosis).

Eukaryotic Refers to unicellular and multicellular organisms having distinct nuclear and cytoplasmic regions (cf. prokaryotic).

Excocytosis The process by which eukaryotic cells secrete molecules from the cell by fusion with the plasma membrane of a membrane-bound vesicle containing these molecules ("cell excreting").

Fibrocyst Cystic lesion found in connective tissue.

Fibrocystic Having characteristics of a fibrocyst.

Homeostasis Equilibrium maintained between the interior and exterior environments of a cell.

***In Situ* Carcinoma** Cells that grow abnormally, but are not invasive.

Ion Channel Transmembrane protein forming a water-filled pore and allowing passive transport of select ions across a chemical gradient. Channels activated by a stimulus are referred to as gated channels.

Keratin Cystine-rich member of a family of proteins forming a type of intermediate filament, usually in epithelial cells. Also found in hair, nails and other cuticular structures.

Leukemia Cancer of bone marrow or lymphatic system.

Lumen The internal space of a tubular or sac-like organ or cell organelle.

Lymphoma Cancer of nodes or glands of the lymphatic system.

Malignant Invasive tumors and tumor cells having the ability to metastasize.

Metastasis The speading of cancer from the primary tumor (tumor of origin) to a secondary location in the body.

Microvilli Thin, fingerlike projections of a cell membrane surface containing a core of actin filaments. These projections increase the surface area of a cell membrane and form brush borders of certain cells, eg., epithelial cells performing absorptive functions.

Mitotic Spindle Array of micrtubules found at opposite poles of a eukaryotic cell undergoing mitosis whose function is to separate duplicated chromosomes.

Morphology An organism's form and structure.

Myeloma Cancer of plasma cells in bone marrow.

Neoplastic Cells, or tissue formed as a result of uncontrolled growth, possibly malignant.

Pinocytosis Uptake of liquids by a cell by endocytosis ("cell drinking").

Pleural Effusion Fluids having escaped from blood vessels or the lymphatic system into the chest cavity.

Primary Site Site of original tumor growth.

Pump Transmembrane protein involved in the active transport of ions and molecules across the cell membrane.

Receptor Proteins that evoke cellular responses as a result of binding of external stimuli (ligands), eg., neurotransmitters.

Sarcoma Malignant tumor of connective tissue, eg., bones, tendons, cartilage and muscle.

Senescence The process of aging that leads to cell death.

Sialomucins Class of glycoproteins with acidic sugar groups that are found in secretions, eg., from mucous, and saliva.

Syngeneic Genetically identical.

Ultrastructure Cellular fine structure observed with an electron microscope.

IMAGE EVALUATION
TEST TARGET (QA-3)

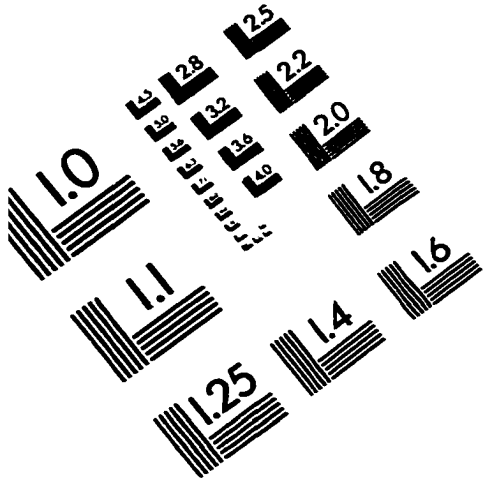

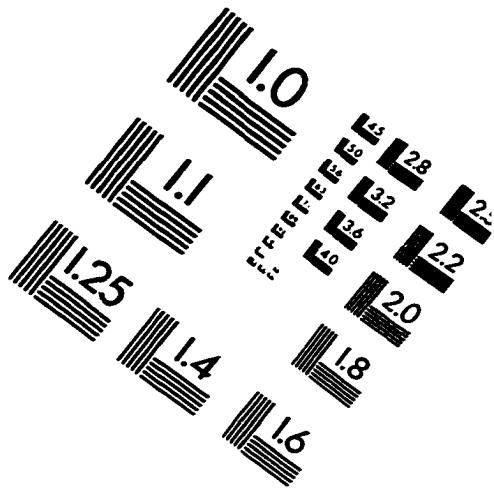

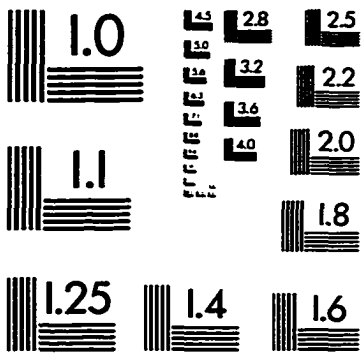

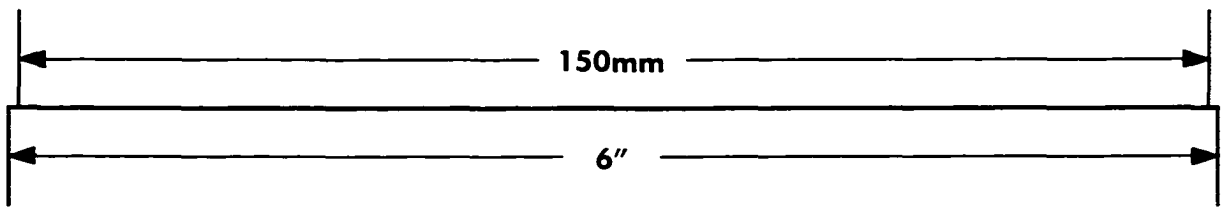

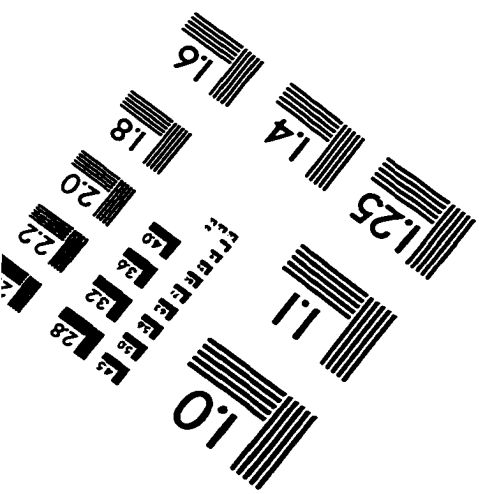

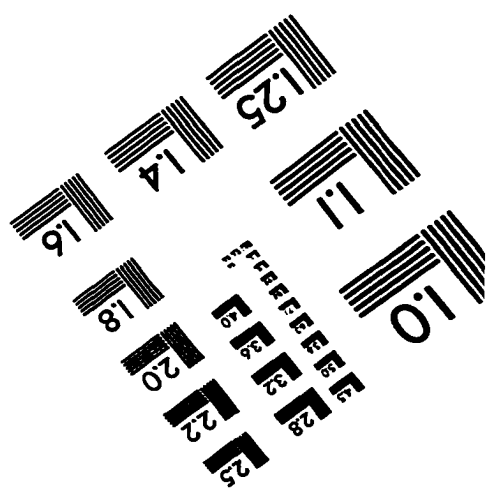

APPLIED IMAGE, Inc
1653 East Main Street
Rochester, NY 14609 USA
Phone: 716/482-0300
Fax: 716/288-5989